ISSN number 0971 - 9709

IGU
Promoting Earth System Sciences

The Journal of Indian Geophysical Union

AN OPEN ACCESS BIMONTHLY JOURNAL OF IGU

VOLUME 29, ISSUE 4, JULY 2025

EDITORIAL OFFICE

Indian Geophysical Union, NGRI Campus, Uppal Road, Hyderabad- 500 007

Telephone: 91-4027012739, 27012332; Telefax:+91-04-27171564

Email: jigu1963@gmail.com, website: http://iguonline.in/journal/

The Journal with six issues in a year publishes articles covering

Solid Earth Geosciences; Marine Geosciences; and Atmospheric, Space and Planetary Sciences.

The Journal is Financially supported by MoES, Govt. of India.

Annual Subscription

Individual Rs -1000/- per issue and Institutional Rs- 5000/- for six issues

Payments should be sent by DD drawn in favour of "The Treasurer, Indian Geophysical Union", payable at Hyderabad,

Money Transfer/NEFT/RTGS (Inter-Bank Transfer), Treasurer, Indian Geophysical Union, State Bank of India, Habsiguda Branch,

Habsiguda, Uppal Road, Hyderabad- 500 007

A/C: 52191021424, IFSC Code: SBIN0020087, MICR Code: 500002318, SWIFT Code: SBININBBHO9.

For correspondence, please contact, Hon. Secretary, Indian Geophysical Union, NGRI Campus, Uppal Road,

Hyderabad - 500 007, India; Email: igu123@gmail.com; Ph: 040 27012332

ISSN: 0257-7968 (Clarivate Analytics)
ISSN: 0971-9709 (NISCAIR)
Approved as bimonthly ESCI journal by Clarivate Analytics
Cited in Indian Citation Index (ICI), New Delhi
Evaluated by NISCAIR, New Delhi
UGC Approved Journal

CONTENTS

Research Articles

Student Section

Report

J. Ind. Geophys. Union, 29(4) (2025), 218-235
https://doi.org/10.71122/JIGU.29(4)2025.0022

Imaging intra-volcanic Mesozoic sediments and shallow crustal configuration from traveltime inversion of long-offset seismic data in Saurashtra basin, India

Renuka Kolluru and Laxmidhar Behera*
CSIR-National Geophysical Research Institute, Hyderabad - 500007, India
** Corresponding Author: laxmidhar.ngri@csir.res.in*

ABSTRACT

Saurashtra on-shore basin is considered a major Mesozoic province of India having wide-spread cover of Deccan Traps (basalts), which acts as major impediment for imaging deeper sub-surface geological structures for the exploration of hydrocarbons. The Mesozoic sediments hidden and entrapped within the basalts, as well as other subsurface geological structures, which can be distinctly imaged using the inversion of long-offset seismic traveltime data. Hence, the robust ray-trace inversion technique is employed for the same traveltime data along the 180 km long NW-SE trending Jodia-Ansador seismic profile of Saurashtra basin. This helped to image the sub-surface geological structures and shallow-crustal P-wave velocity model (V_P) of this region. The V_P model delineated along the seismic profile has five-layers derived from the 2-D ray-trace inversion of both refraction and reflection traveltime data. The low-velocity-layer (LVL) Mesozoic sediments (4.2 km/s) of 0.5-1.0 km thickness is imaged, which is hidden below the high-velocity-layer (HVL) Deccan Traps (4.8-5.2 km/s). Below the low-velocity Mesozoic layer, another HVL (5.4-5.5 km/s) is present, which is considered as Mesozoic volcanics of Jurassic age having thickness variations of 0.5-1.6 km that pinches out towards Ansador. The granitic-gneissic basement (5.8-6.0 km/s) is very undulating having thickness variation of 2.5-3.5 km, forming horst and graben structures along the profile. Below the basement, a relatively high-velocity (6.5 km/s) layer has been delineated, which may be attributed to mid-crustal rocks. It is constrained to a maximum 10 km depth using long-offset seismic reflection data. There is significant up-warping of basement and the mid-crustal layer, which indicate complex geological and tectonic setup because of the Late Cretaceous Deccan volcanism and out-pouring of wide-spread tholeiitic lavas on the surface, masking the hydrocarbon-bearing Mesozoic sediments of the basin.

Keywords: Deccan Traps, Mesozoic sediments, Long-offset seismic data, Basement, Mid-crust, Traveltime inversion

INTRODUCTION

The Deccan Traps of the Late Cretaceous age (~65 Ma), act as a mask for the hydrocarbon-bearing Mesozoic sediments, which cover significant parts of the on-shore Saurashtra basin in western India (Figure 1). Evidence of the Mesozoic sediments, hidden by Deccan basalts in on-shore Saurashtra basin, was confirmed from the Lodhika and Dhandhuka drilled wells (Figure 2) as well as the exposed Mesozoic Dhrangadhra sandstones towards north-eastern part of the basin (Singh et al., 1997). To obtain spatial extension of the intra-volcanic low-velocity Mesozoic sediment layer (LVL), CSIR-NGRI executed different long-offset seismic profiles along with a small experimental profile passing through the Lodhika well during 1994-1996, which was sponsored by the OIDB and ONGC (NGRI, 1998). The LVL hidden below the high-velocity volcanic layer (HVL) can be detected by modeling of long-offset seismic data using traveltime-skip (SKIP) phenomena (Greenhalgh, 1977; Whiteley and Greenhalgh, 1979; Tewari et al., 1995; Behera et al., 2002; Sain et al., 2002; Behera and Sen, 2014), which is mainly constrained by the velocity contrasts of HVL and LVL as well as the thickness of LVL. The 2-D ray-trace modeling and inversion technique (Zelt and Smith, 1992; Zelt, 1999) is employed for the seismic traveltime data along the 180 km long Jodia-Ansador profile (Figure 1) having significant SKIPs to image LVL hidden below the HVL layer, and to obtain other sub-surface geological units, granitic-gneissic basement configuration and the underlying shallow-crustal structure. The derived shallow-crustal 2-D P-wave velocity model (V_P) is constrained to a maximum of 10 km depth in the studied region of the Saurashtra basin, located in the western part of India (NGRI, 1998).

There are significant differences about the velocity and thicknesses of the Mesozoic sediments and basalts obtained in this region from the modeling and inversion of traveltime data (refraction and reflections) for the small experimental profile as well (Figure 1) that passes through the Lodhika well (Figure 2), which is constrained by the well lithology (Dixit et al., 2000; Sain et al., 2002). However earlier, Murty et al. (2016) has obtained two different velocity models for the same Jodia-Ansador seismic profile from ray-trace inversion of first-arrival traveltime data, picked from the original monitor/paper records (analog data) by honoring velocities and thicknesses of the Mesozoic sediments obtained by Dixit et al. (2000) and Sain et al. (2002). Nevertheless, the thickness and velocities of the Mesozoic sediments as well as basalts obtained along the same seismic profile cannot have two different values (Murty et al., 2016), which conflicts with each other leading to model non-uniqueness. To ameliorate all these issues and provide a geologically plausible high-resolution shallow-crustal V_P model along the Jodia-Ansador profile, long-offset digital seismic data acquired along the profile is used for analysis, by picking, modeling and ray-trace inversion. The derived V_P model is further validated by computing ray-density/hitcounts (Hits), model parameterizations of different velocity and boundary nodes along with the measure of traveltime RMS residuals and normalized chi-square (χ^2) misfit of the observed data (Zelt and Smith, 1992; Sain et al., 2002; Behera et al., 2004). The main objectives of present study are, (i) to image intra-volcanic LVL Mesozoic sediments, which is underlain by HVL Deccan Traps, (ii) delineate sub-surface velocity heterogeneity, horst and graben features, basement configuration and shallow-crustal structure, (iii) constrain and

validate the V_P model derived along the profile using nearby well lithology of the basin.

GEOLOGY AND TECTONIC SETTING

The Saurashtra basin belongs to an Atlantic type rifted passive margin basin, which is placed in the category of peri-cratonic rift basins of India (Biswas et al., 1993). The basin has many highlands of exposed basalts and rocky hillocks surrounded by the Gulf of Cambay in southeast, the Arabian sea in west, mainland of Gujarat in east and Gulf of Kutch in the north (Figure 1). The sequential rifting of East Africa, Madagascar and Seychelles has developed this basin (Biswas et al., 1993; Plummer, 1994). This is bounded by a major fault, which was earlier recognized as Kathiawar horst and later as Saurashtra horst. The other faults namely Cambay rift in east, Surat depression in south, NE-SW faulted margin of Kutch rift in north, and offshore shelf-facies in west, bound this basin. The NE-SW Delhi-Aravalli trend is an important orogenic trend, continues across into the Saurashtra platform. Hence, the structural and tectonic settings of the Saurashtra basin is thought to be largely controlled by this Precambrian trend. Regional fault trends and alignments of dyke swarms occurring in the southern and south-eastern parts, show preferred NE-SW orientations, possibly due to manifestation of the Precambrian basement lineaments (Biswas and Deshpande, 1983). Several plutonic centers occur in this area, the most important is the Girnar massif near Junagadh. A broad domal feature is located in the NE part of Saurashtra basin (Figure 1) has outcrops of Mesozoic sediments (Dhrangadhra and Wadhwan formations). The general stratigraphy of Saurashtra basin consists of Precambrian granitic-gneissic basement overlain by Mesozoic rocks, followed by the Late Cretaceous Deccan Traps with sporadic distribution of thin cover of Neogene and Quaternary sediments on the top surface (Table 1). The Deccan Traps (basalt) mainly cover the basin with exposed Lower Cretaceous sediments in NE (Figure 1). The eastern fringe of basin is a low-land interspersed with marshy lakes. The coastal plains mainly fringe the trappean highland comprising the Cenozoic cover of Tertiary and Quaternary rocks. There are several tholeiitic intrusions of acidic, alkaline, and mafic/ultramafic plugs present in this basin, major ones being the Girnar, Osham, Barda, Alech in the western part and Vallabhipur, Palitana and Rajula in the south-eastern part (Merh, 1995) of the on-shore Saurashtra basin of India (Figure 1).

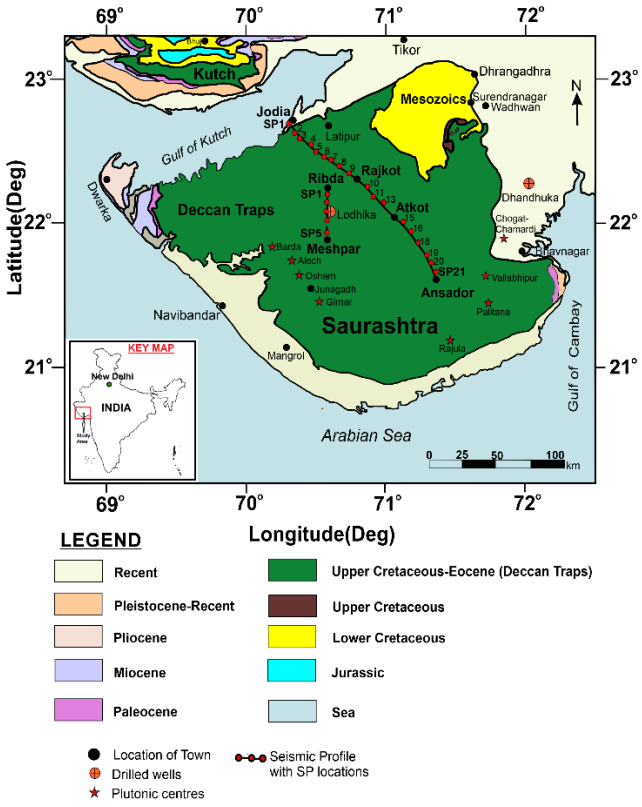

Figure 1. The geology map of Saurashtra basin (marked as inset within the key map) along with the NW-SE trending Jodia-Ansador and N-S trending Ribda-Meshpar seismic profiles. The different rock types exposed on the surface are indicated by color legends corresponding to their ages. The shot points (SPs) are indicated as red dots with labels along the profile, which is shown as bold black line. The drilled well locations of Lodhika and Dhandhuka are also marked. The Lodhika well is located on the Ribda-Meshpar seismic profile.

Table 1. Generalized stratigraphy of the Saurashtra basin (Modified after Merh, 1995)

Rock/Sediment type	Age
Costal sediments, alluvium, marine sediments like Miliolite	Quaternary
Marine to fluvio marine rocks	Upper Tertiary (Neogene)
---------- Unconformity ----------	--------- Unconformity ----------
Laterites	Paleocene
Deccan Traps	Upper Cretaceous to Lower Eocene
---------- Unconformity ----------	--------- Unconformity ----------
Surendranagar and Wadhwan formations	Upper Jurassic to Lower Cretaceous
---------- Unconformity ----------	----------Unconformity ----------
Crystalline Basement (Granite and Gneiss)	Pre-Cambrian (Proterozoic)

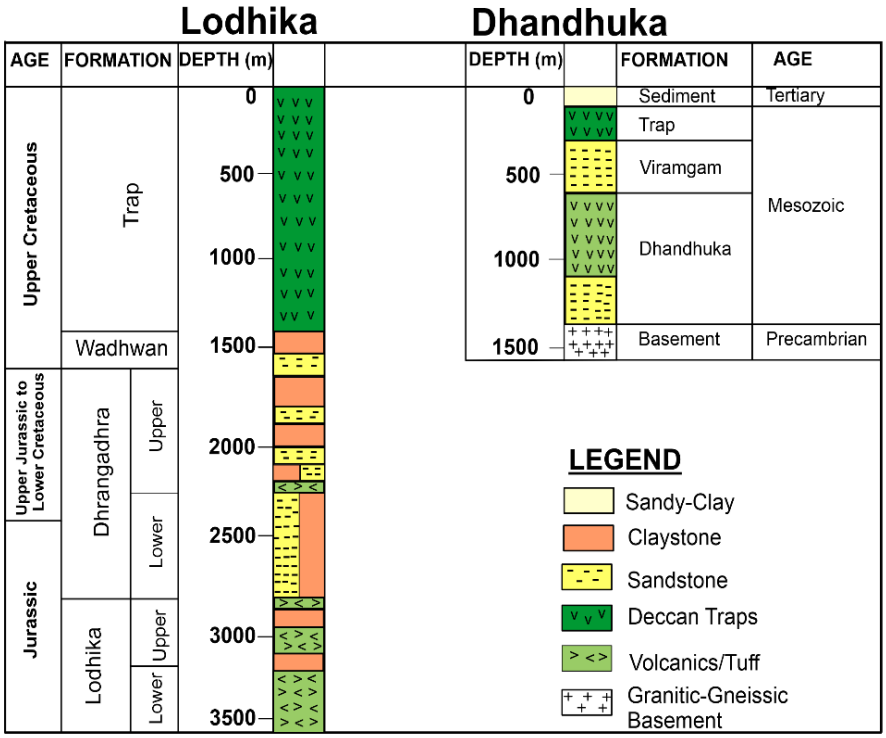

Figure 2. Lithostratigraphy of Lodhika and Dhandhuka wells drilled in the Saurashtra basin (Modified after Singh et al., 1997).

In fact, the Saurashtra basin is a horst block, surrounded by the major faults on its four sides. The North Kathiawar Fault (NKF) is located towards north and the Son-Narmada Fault (SNF) extends in south (Biswas, 1982). The WNW-ESE trending West Coast fault (WCF) system and the West Cambay Basin Margin Fault (WCBMF) mainly confine the western boundary by delimiting the eastern boundary. Three major Pre-Cambrian trends i.e., the Dharwar trend (NNW-SSE) in southern part, the Aravalli trend (NE-SW) in north-eastern part and the Satpura trend (ENE-WSW) in central part, mainly coincide in the Saurashtra region (Biswas and Deshpande, 1983). Hence, the Saurashtra horst acts as a foundered block among the three intersecting rifts, which lie along the major Precambrian trends. It is nearly a square-shaped block tilted towards the southwest. The straight western margin of the basin acts as a faulted-margin, which follows the Dharwar trend. This block is uplifted because the western margin fault cut across the Saurashtra arch (Biswas, 1987). The present structure of Saurashtra basin is a manifestation of numerous phases of tectonic alterations, including the rifting and separation of the Indian and African plates, segmentation of its western continental margin as it drifted northward, followed by the Deccan volcanism due to the Reunion plume (White and McKenzie, 1989).

DATA

Seismic data acquisition and pre-processing

The long-offset seismic refraction and reflection data was acquired by the Controlled Source Seismic (CSS) Group of

CSIR-NGRI during 1994-96 along NW-SE trending Jodia-Ansador profile in the Saurashtra basin (Figure 1). The data was recorded from 21 shot points (SPs) using two 60 channel DFS-V seismic data acquisition systems in master-slave mode with ~10 km shot point (SP) interval and geophone group interval of ~100 m having 6 geophones in a group (channels) with natural frequency of 4.5 Hz. The sampling interval (SI) of the seismic data recording was kept for 4 ms with system dynamic range (DR) of 84 dB and wide-band frequencies ranging from 3 Hz to 64 Hz. A notch-filter of 50 Hz was kept in operation during data recording, to minimize the effect of power-line noise. The data was recorded by blasting each SP loaded with explosives of different charge sizes in pattern of holes drilled to maximum 25 m depth with 50 kg explosives put inside each hole. The charge size of each SP varies from 50 kg to 450 kg, depending upon the maximum source-receiver offset and number of spreads having each spread length of 11.8 km (NGRI, 1998). Each spread consisted of 120 geophone groups. For shot points SP1 to SP9, the data was recorded up to maximum-offset of 50 km (approximately 4 spreads) and for SP10 to SP21, the data was recorded with varying offsets (Figure 1).

We have used the raw seismic data acquired along the profile (Figure 1) for pre-processing by merging the different spread data into individual SP gathers (supergathers). The pre-processing steps (Yilmaz, 2001) applied to obtain individual SP gathers are, format conversion, sorting, merging, geometry application using topographical survey data, editing and muting of noisy/dead traces, spherical-divergence/geometrical-spreading correction, application of field-statics for weathering and elevation correction, spiking-deconvolution and band-pass filtering (Table 2). The seismic data quality is very good having high signal-to-noise ratio (SNR) in which the P-wave phases having direct, refracted and reflected arrivals are prominent in the example SP gathers (Figure 3) along the profile, which are picked for modeling and inversion. The trace-normalized seismic data are displayed in reduced-time with reduction-velocity of 7.0 km/s (Figure 3).

Data analysis and picking

The identification and picking of different phases in the observed seismic data (Figure 3) are the most important and crucial step for modeling and inversion. Two prominent first-arrival or refraction phases (P_1, P_4) and four reflection phases (P^1, P^2, P^3, P^4) are identified in the observed seismic data as shown in example shot gathers (Figure 3). As we can observe in the data, the first-arrival phases are fairly clear at small-offsets, but as the offset becomes large, there is greater uncertainty in the identification of these phases with a possibility of cycle-skip. We have picked both the first-arrival and reflection traveltimes manually by assigning the picking uncertainty of ± 25 ms for first-arrivals and ± 50 ms for reflection phases of all the 21 SP gathers recorded along the profile. The picking uncertainties are generally assigned to the traveltime data to avoid over- or under-fitting during the inversion. After careful inspection of the data quality, the uncertainties are assigned to the data picked taking into account SNR and frequency content using a constant value for each phase (Zelt and Smith, 1992; Zelt, 1999; Behera et al., 2004). Since the seismic profile traverses mainly through the Deccan Trap covered regions of the Saurashtra basin (Figure 1), there is significant loss of seismic energy due to attenuation and absorption through the highly heterogenous and rugose Deccan basalts. Hence, the continuity and coherency of the first-arrival phases are disrupted at long-offsets. Also, we have observed traveltime skips (SKIP) in the seismic data at long-offsets due to lowering of signal amplitudes, which indicate the presence of low-velocity-layer (LVL) hidden below the high-velocity-layer (HVL) basalts/traps (Figure 3). The reflection phases are strong and prominent at both near and long-offsets due to significant impedance contrast as well as amplitude build-up due to total internal reflections in the post-critical range (Greenhalgh, 1977; Whiteley and Greenhalgh, 1979; Behera et al., 2002, 2004, Behera and Sarkar, 2011; Behera and Sen, 2014; Behera et al., 2021).

Table 2. Pre-processing flow of 2-D seismic data

Data loading of tapes stored from DFS-V Recording System
Demultiplexing of data (conversion of SEG-B to SEG-Y format)
Sorting of traces for each individual FFID
Merging of individual FFID's to prepare individual SP gathers
Application of field geometry for individual SP gathers
Muting and editing of noisy/dead traces
Spherical divergence/Geometrical spreading correction with T^2V^1 exponential gain function
Application of field statics for weathering and elevation corrections (i.e., shot and receiver statics, datum statics)
Spiking deconvolution (OL = 0.60s, PL = 0.08s, PPW = 0.1%)
Band-pass filtering (3-8-24-60 Hz)

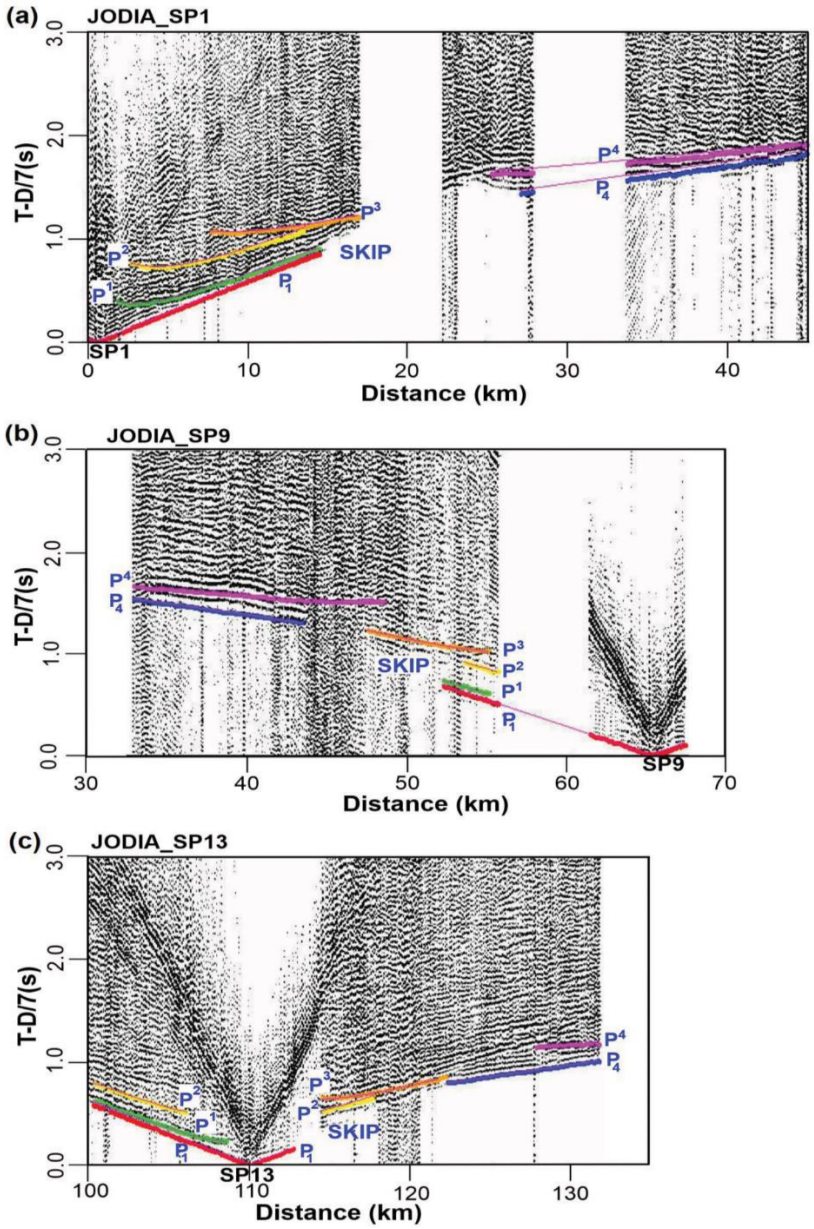

Figure 3. Example record sections of different shot point (SP) gathers shown for data quality and the phases picked are indicated by colored dots representing first-arrivals (P_1, P_4) and reflections (P^1, P^2, P^3, P^4), respectively for **(a)** SP1, **(b)** SP9, and **(c)** SP13 along the seismic profile. The traveltime-skip (SKIP) is clearly observed in the example SP gathers, indicating presence of LVL hidden below the HVL. The SP gathers (data) are displayed in reduced-time with reduction velocity of 7.0 km/s.

METHODOLOGY

To derive P-wave velocity model (V_P) for the Jodia-Ansador seismic profile (Figure 1), we have employed the 2-D ray-trace inversion approach of Zelt and Smith (1992) by using first-arrival and long-offset reflection traveltime data picked for all the SPs along the profile. Since, there are traveltime-skips observed in the first-arrival data for most of the SPs, proper care has been taken for ray-trace inversion by constraining the model with nearby well lithology and previous modeling results in this region (Dixit et al., 2000; Sain et al., 2002; Murty et al., 2016; Behera et al., 2021). The effectiveness of ray-tracing algorithm and its use in the traveltime inversion are strongly characterized by the model parameterization (Zelt and Smith, 1992). The model is parameterized by variable size blocks having arbitrary number and spacing of boundary nodes for each layer connected by linear interpolation in which the number and position of nodes for each boundary may differ.

The traveltimes and their partial-derivatives with respect to the chosen velocity and boundary nodes are calculated during ray-tracing along with the corresponding traveltime fit of the observed data and the forward response obtained for the starting velocity model. The model parameters are then

updated iteratively using the correction vector obtained from the damped-least-square (DLS) inversion of traveltime residuals. This iterative inversion process is continued until a satisfactory fit of the observed traveltime data and computed response of the model is achieved with corresponding normalized chi-square (χ^2) misfit of 1.0. The ray-trace inversion is performed simultaneously for both velocity and interface boundary nodes of the model derived using first-arrival as well as reflection traveltime data (Zelt and Smith, 1992).

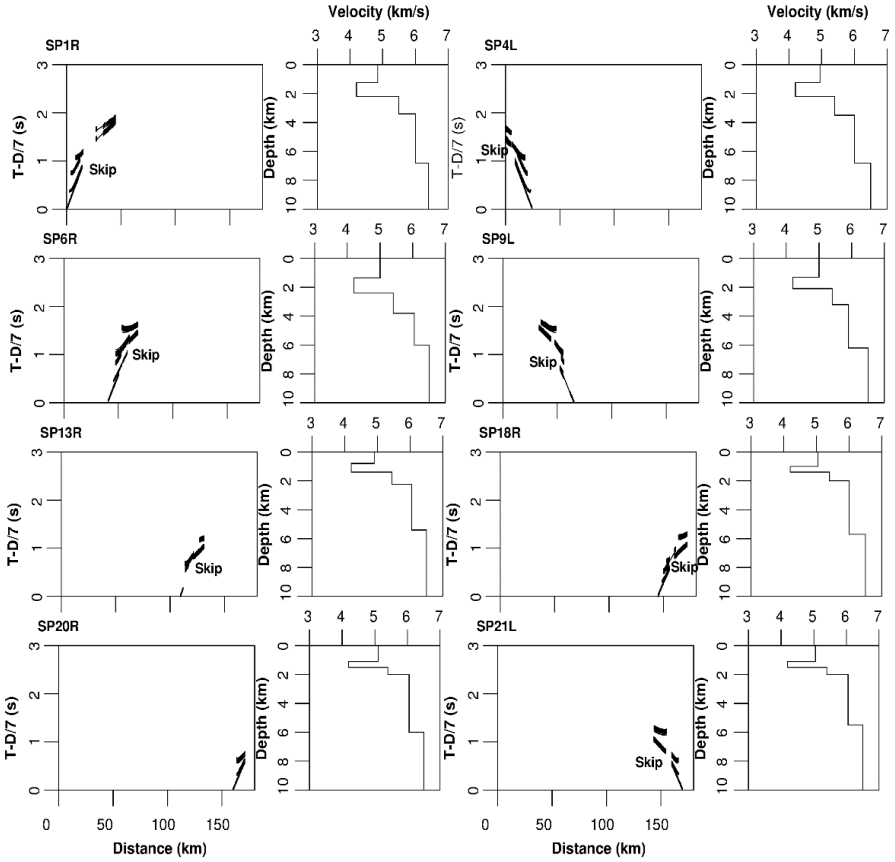

Figure 4. 1-D velocity-depth functions (right panel) obtained after the damped-least-square inversion of the observed P-wave first-arrival and reflection traveltime data (vertical bars) shown for selected SPs from SP1 to SP21 with the corresponding traveltime fit (solid lines) plotted in reduced-time of 7.0 km/s reduction velocity (left panel) for each SP. The traveltime-skips are prominent in the observed data indicating presence of LVL all along the profile.

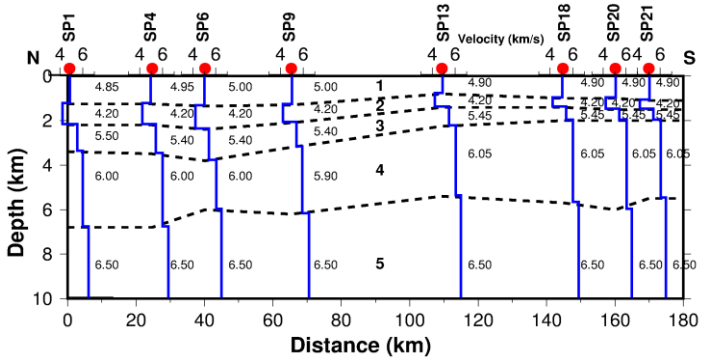

Figure 5. Pseudo 2-D velocity model derived by smoothly joining (dashed lines) the 1-D velocity-depth functions (solid blue lines) obtained for different SPs along the profile (Figure 4). The velocity-scale for each 1-D velocity-depth function is shown on the top with corresponding values from 3-7 km/s having small indents marked at every 1 km/s. The individual SPs are indicated as red dots with label. The layer numbers are indicated (1, 2, 3, 4, and 5) with the corresponding average velocity values (5.00 km/s, 4.20 km/s, 5.40 km/s, 6.00 km/s, and 6.50 km/s) obtained for each layer from the 1-D inversion of traveltime data along the profile.

MODELING AND INVERSION

1-D and pseudo 2-D modeling

We have computed the 1-D velocity-depth functions for each SP along the profile (Figure 4). The 1-D velocity-depth functions indicate that first-arrivals have apparent velocities of 4.8-5.0 km/s representing the Deccan Traps/basalts and 5.9-6.0 km/s corresponding to the granitic-gneissic basement, respectively. The computed responses obtained from the 1-D velocity models are compared with the corresponding observed data for optimum fit along the profile (Figure 4**).** We observed that, the 1-D velocity models derived using P-wave first-arrival and reflection data show 4.9 km/s, 5.4 km/s, 6.0 km/s and 6.5 km/s, respectively as the average apparent velocities for corresponding traveltime segments of all SPs along the profile at different offsets (Figure 4). The traveltime-skips as observed from different SPs, indicate the presence of LVL below the HVL. The magnitude of traveltime-skip or delay (Figures 3 and 4) constrain the thickness and extension of the LVL along the profile. We could able to constrain the apparent P-wave velocity (4.2 km/s) and thickness of the LVL (which is gradually thinning towards Ansador (SW) of the profile) from the extent of the skip/delay in traveltime, which is of the order 0.2 to 0.6 s (Figures 3 and 4) as observed from different SPs (SP1 to SP21) along the Jodia-Ansador seismic profile (Figure 1). The apparent P-wave velocity of the LVL is constrained from cumbersome 1-D inversions, using the DLS layer-stripping inversion approach (Zelt and Smith, 1992; Sain and Kaila, 1994; Behera et al., 2004; Behera and Kumar, 2022). The thickness of the LVL increases from SP1 to SP9, and decreases from SP10 to SP21 as constrained from the corresponding 1-D velocity modeling along the seismic profile (Figure 4). We have derived the pseudo 2-D velocity model (Figure 5) along the profile by smoothly joining the corresponding 1-D velocity-depth functions obtained at each SP (Figure 4), which constitute as a good starting model for the 2-D ray-trace inversion to derive the shallow-crustal velocity model of the Saurashtra basin without any bias for the traveltime inversion.

2-D Ray-trace inversion

To derive the shallow-crustal V_P model of Jodia-Ansador seismic profile in Saurashtra basin (Figure 1), we have employed the 2-D ray-trace modeling and inversion (Zelt and Smith, 1992) of first-arrival and reflection traveltime data, picked from all the SPs (Figure 6). The ray-trace inversion takes into account suitable model parameterization of each velocity and boundary node. Hence, both velocity and layer structure of the model are derived simultaneously from ray-trace inversion of traveltime data using layer-stripping approach, which helps to determine deeper layers successively (Zelt, 1999). The inversion is an iterative process in which the computed responses obtained from each layer are superimposed on the corresponding observed data. The different phases have been classified and indicated by respective colored dots on the observed data and shown as vertical bars with their corresponding picking uncertainties on the traveltime plots (first-arrival refraction and reflections) for all the SPs, respectively (Figure 6). The iterative inversion is continued until an optimum fit is achieved between the observed traveltime data and the corresponding computed responses through the different layers of the model (Zelt and Smith, 1992; Behera et al., 2002, 2004; Behera and Sen, 2014; Behera and Kumar, 2022; Kumar and Behera, 2024). The model is constrained by the RMS traveltime residual along with the χ^2 misfit computed for all the SPs along the profile. The normalized χ^2 misfit can be expressed as (Menke, 1984; Zelt and Smith, 1992):

$$\chi^2 = \frac{1}{N}\sum_{i=1}^{N}\left(\frac{d_m^i - d_{obs}^i}{\sigma_d^i}\right)^2 \quad (1)$$

where d_m^i is the modeled data, d_{obs}^i is the observed data, σ_d^i is the standard deviation, and N determines the total number of traveltime data used in the ray-trace inversion. If the value of $\chi^2 \sim 1.0$, then the model is having good fit and can be acceptable. If χ^2 value is greater than 1.3, the model corresponds to under-fit, and if the value is less than 0.7, then it indicates over-fit.

The ray-trace inversion is able to handle large number of SPs in spite of the complexity of the source-receiver spread configuration or quality of the data. It is essential to perform ray-tracing through the model with the help of efficient numerical solutions of 2-D ray-trace equations coupled with ray take-off angles (Červený et al., 1977; Zelt and Ellis, 1988). Besides this, we have employed the smooth-layer boundary simulation followed by partial-derivative computation of traveltime data with respect to the corresponding model parameters (e.g., velocity and boundary at each node) to reduce instability associated with the blocky model parameterization and the ray-trace inversion (Spence, 1984; Huang et al., 1986; Firbas, 1987; Lutter et al., 1990; Zelt and Smith, 1992; Behera et al., 2004, 2021; Behera, 2011a, b; Behera and Sen, 2014; Talukdar and Behera, 2018; Behera and Kumar, 2022; Kumar and Behera, 2024). The partial-derivatives computed correspond to any arrivals (e.g., refraction, reflection, head-wave, multiple etc.) of the observed traveltime data. To avoid two-point ray-tracing of the algorithm, it is essential to interpolate the traveltimes and their partial-derivatives across ray end-points of the corresponding receiver locations. Finally, the damped-least-squares inversion is employed with chosen damping-factor for simultaneous modification along with

model-parameter update of both velocity and boundary nodes, respectively (Zelt and Smith, 1992, Zelt and Ellis, 1998; Zelt, 1999; Behera et al., 2004; Behera, 2011a, b; Behera and Sen, 2014; Talukdar and Behera, 2018; Behera and Kumar, 2022). During the ray-trace inversion through the model, both traveltime-residual vector and partial-derivative matrix are calculated for a specific iteration. After initial ray-tracing, we have computed the parameter modification vector and applied to the current velocity model. This is followed by ray-tracing through the updated model, which is continued until optimum fit of the observed and computed data are achieved with pre-defined stopping-criteria (Spence et al., 1985; Zelt and Smith, 1992; Behera and Kumar, 2022).

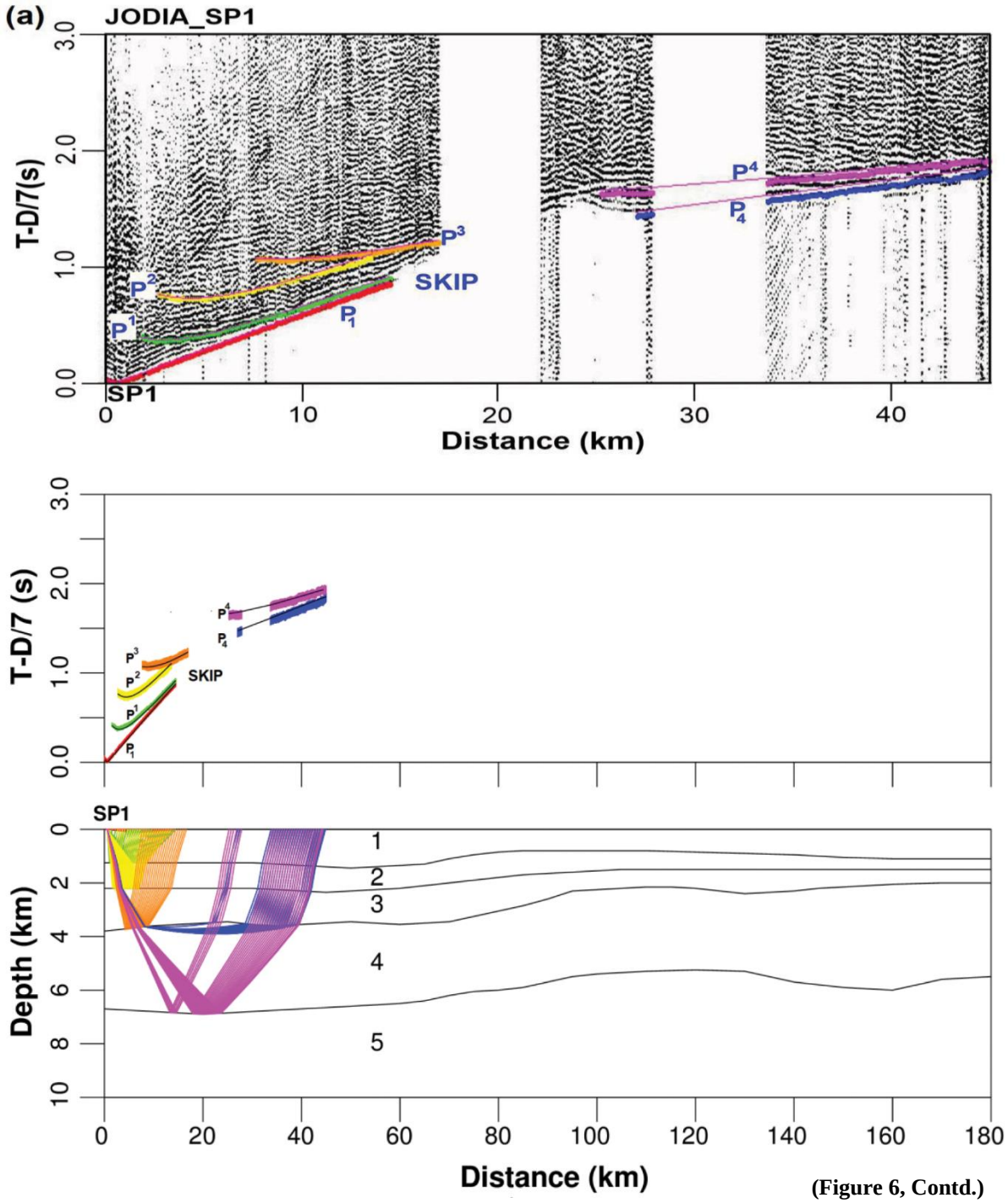

(Figure 6, Contd.)

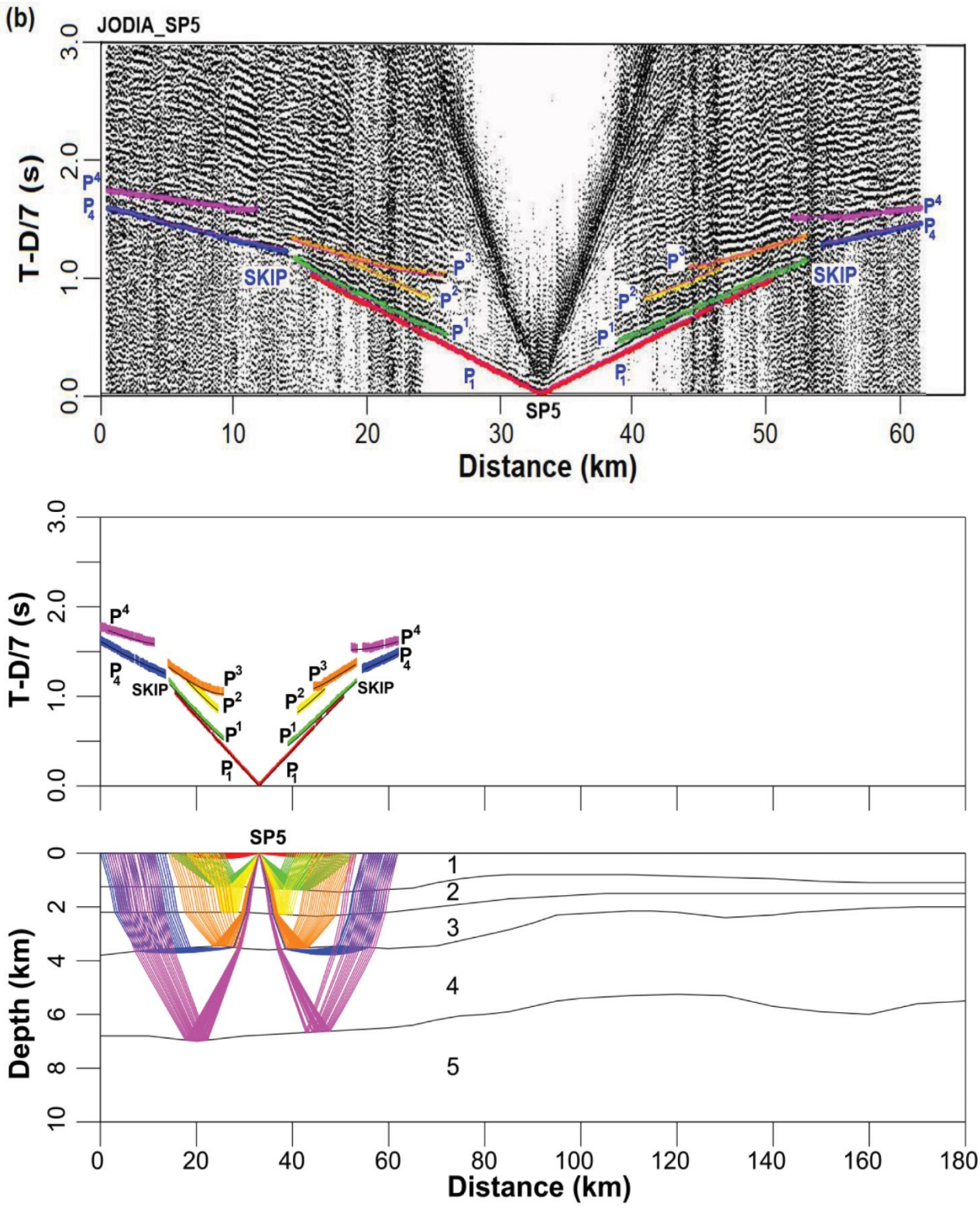

(Figure 6, Contd.)

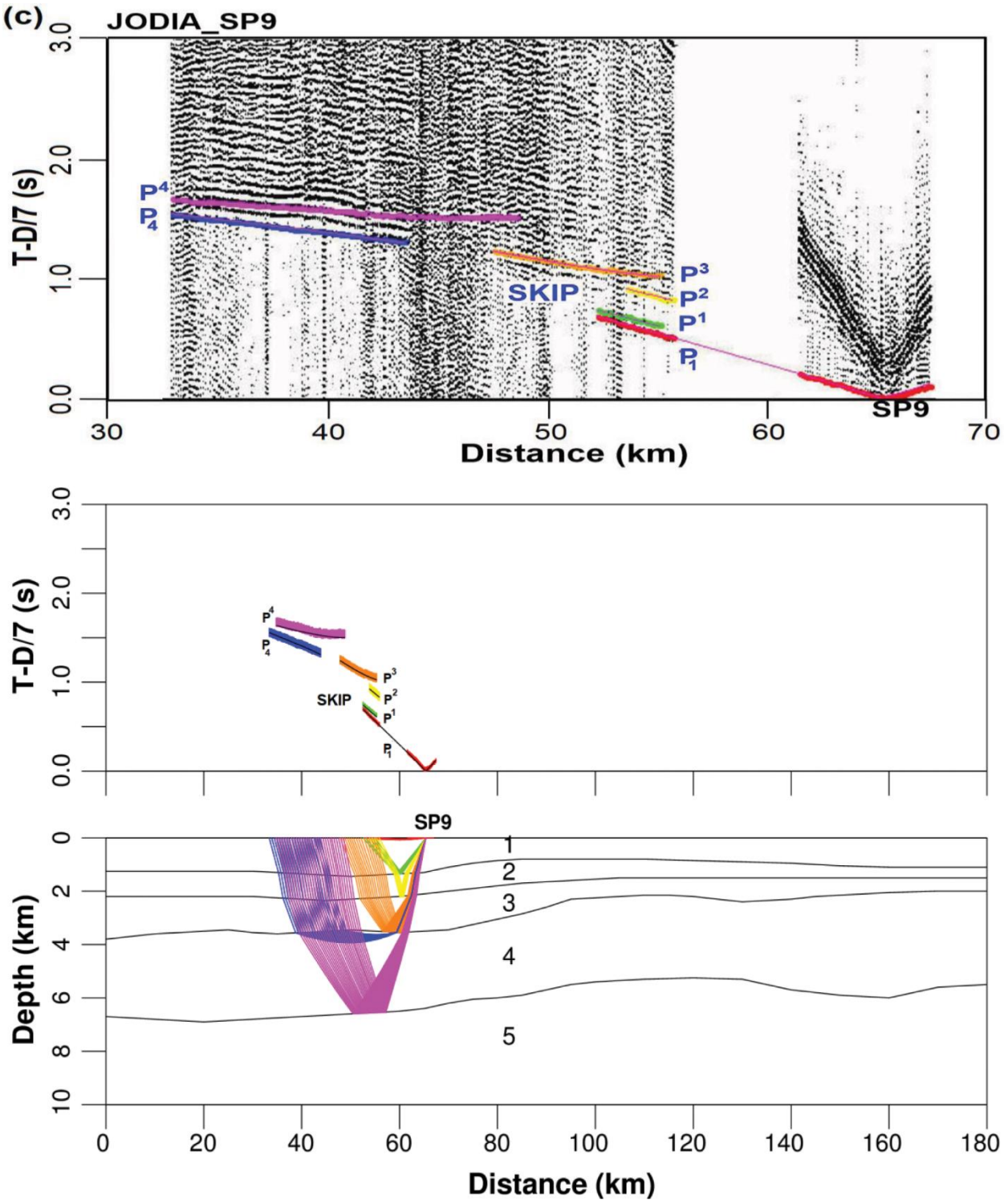

(Figure 6, Contd.)

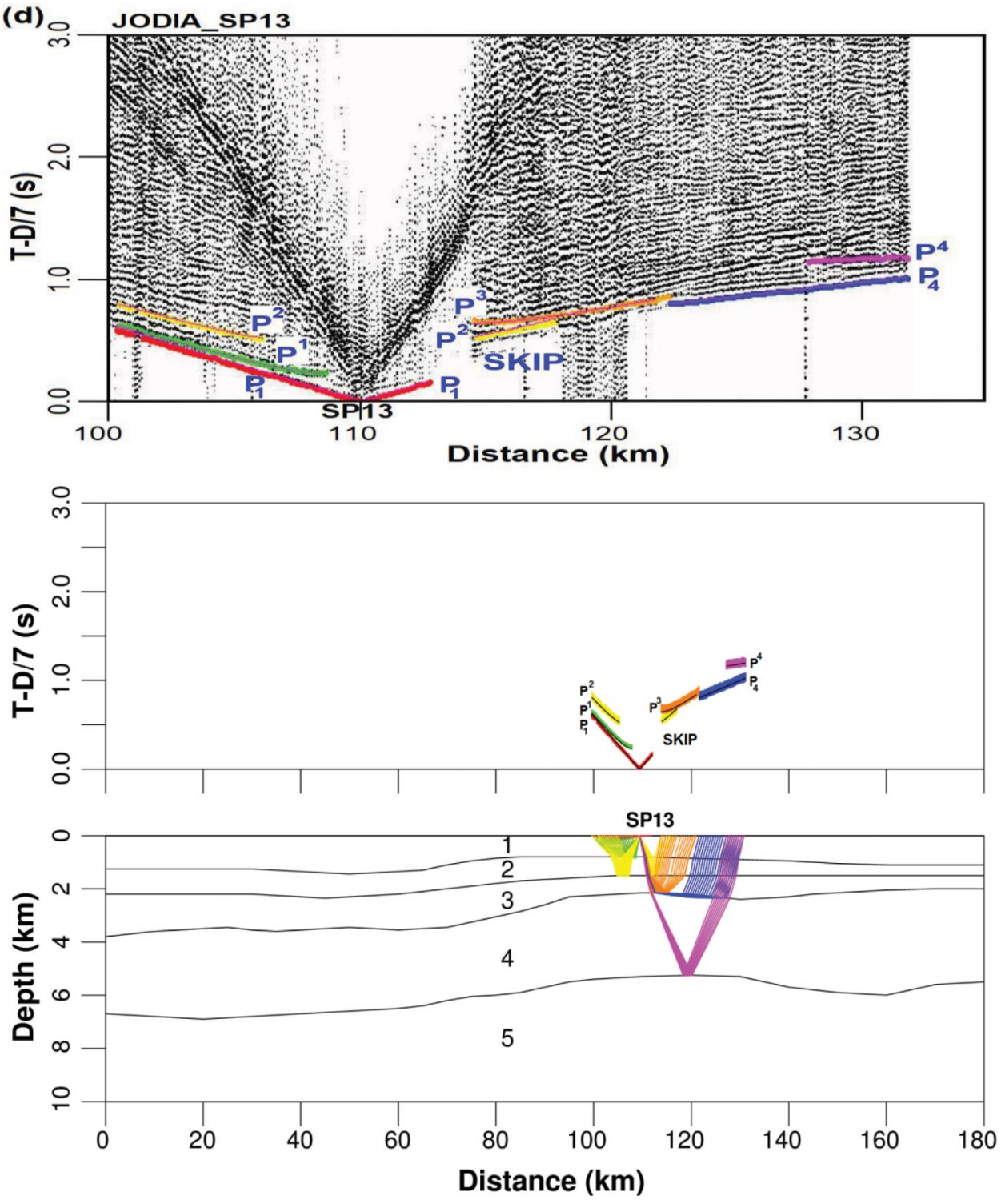

(Figure 6, Contd.)

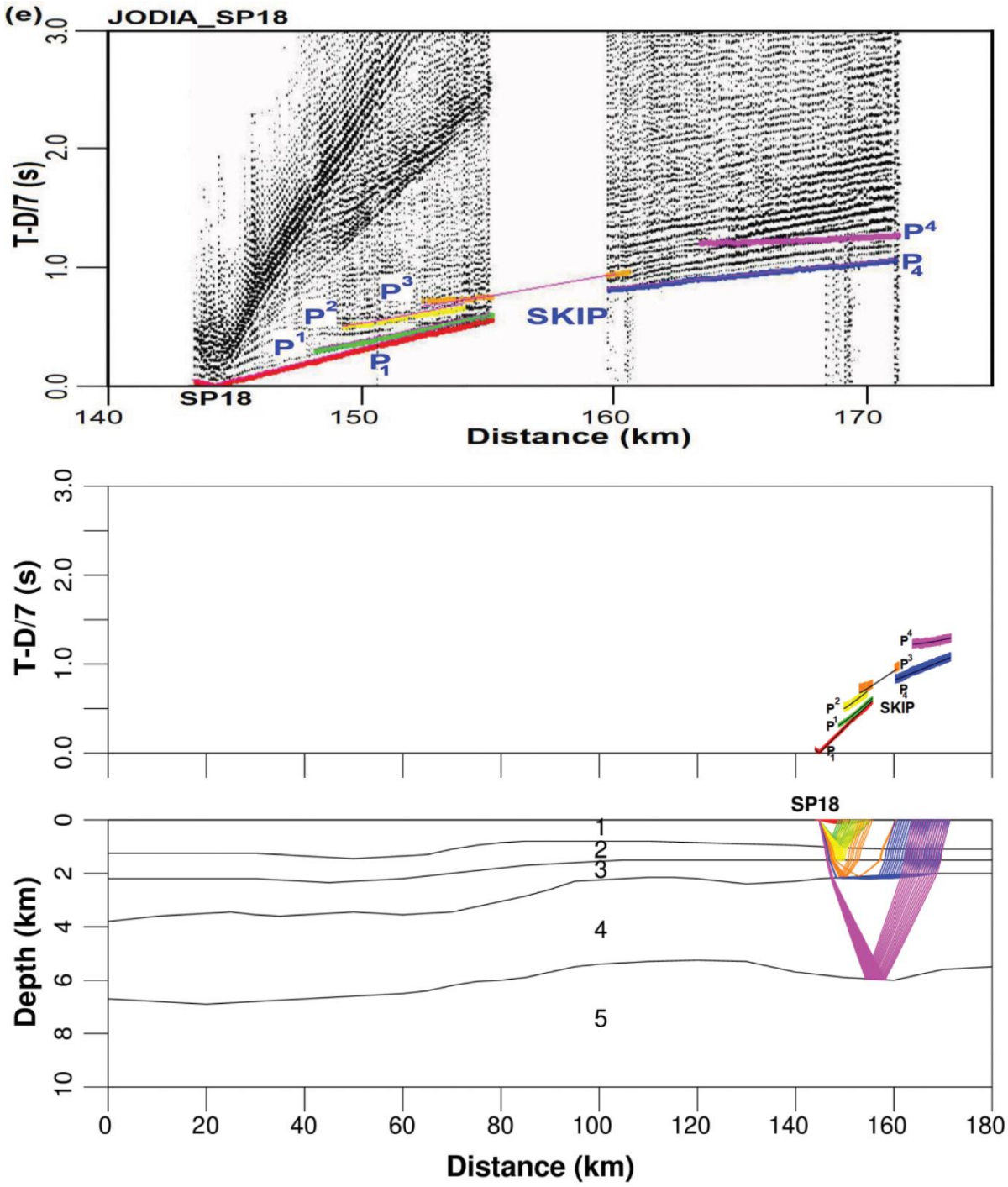

Figure 6. The ray-trace inversion of P-wave seismic data (refraction and reflection traveltimes) showing rays traced through each layer of the final velocity model derived. The corresponding observed data and ray-trace inversion along the profile with different phases picked (colored dots) in the observed data (top panel) shown for representative SP gathers **(a)** SP1, **(b)** SP5, **(c)** SP9, **(d)** SP13, and **(e)** SP18 along the profile. The first-arrival refraction (P_1, P_4) and reflection (P^1, P^2, P^3, P^4) traveltime data picked are shown as colored bars indicating the picking uncertainties assigned for different phases of all the SPs in the respective traveltime plots (middle panel). The corresponding computed responses shown as solid black line superimposed on the observed data to indicate the nature of the traveltime fit (middle panel) obtained by the ray-trace inversion through each layer (marked by the same layer numbers 1, 2, 3, 4, and 5 as shown in Figure 5) of the derived velocity model (bottom panel). The traveltime data are plotted in reduced-time with 7.0 km/s reduction velocity. The traveltime-skip observed in the first-arrival data for all the SPs are marked as SKIP, which indicates presence of LVL along the profile (layer number 2) shown in bottom panel. To avoid any distortion of ray propagation and free diving of rays through the model, the maximum depth of the model is extended to 10 km.

The corresponding final 2-D ray-trace inversion of P-wave traveltime data (first-arrival refraction and reflection traveltimes) for all twenty-one SPs is shown (Figure 7) along the 180 km long Jodia-Ansador seismic profile (Figure 1). The standard iterative forward-modeling strategy followed by the layer-stripping inversion approach (Zelt and Smith, 1992; Zelt, 1999) has been incorporated for the 2-D ray-trace inversion using very good input starting pseudo 2-D velocity model (Figure 5) obtained independently from the 1-D inversion of corresponding P-wave first-arrival and reflection traveltime data (Figure 4).

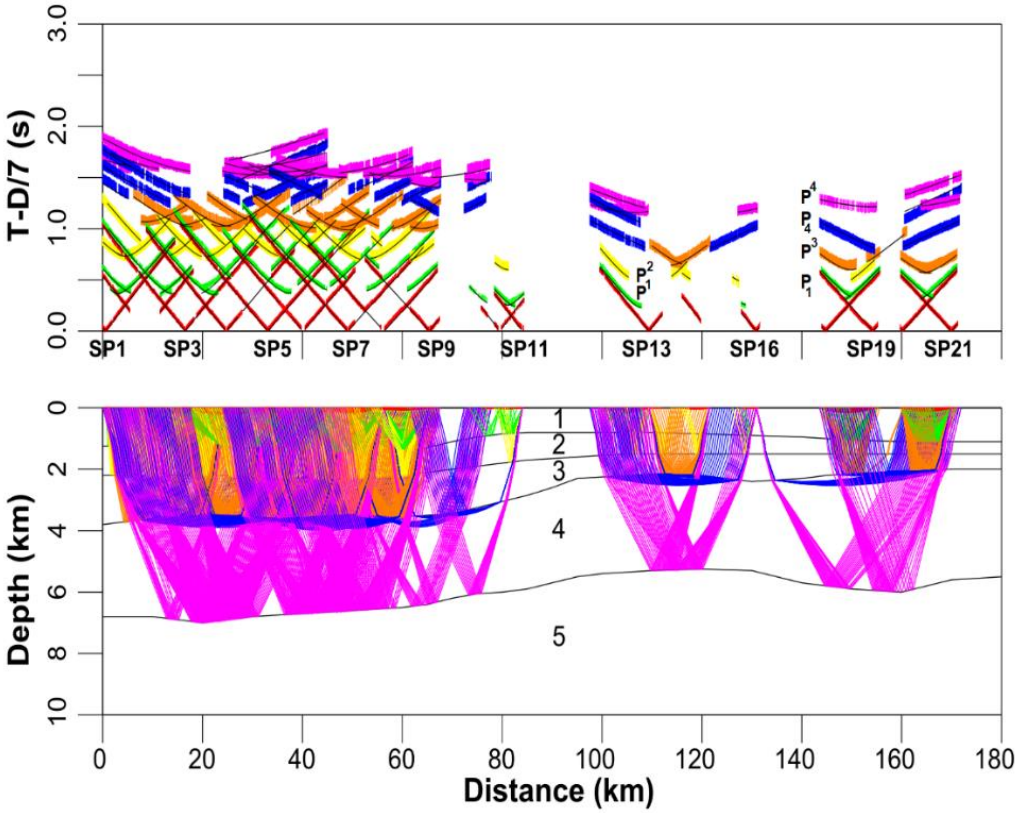

Figure 7. The ray-trace inversion of P-wave seismic data (refraction and reflection traveltimes) showing rays traced through each layer of the final velocity model derived from all the SPs (SP1 to SP21) along the seismic profile. The picked first-arrival refraction (P_1, P_4) and reflection (P^1, P^2, P^3, P^4) traveltime data are shown as colored bars for all the SPs, and the corresponding computed responses indicated as solid black lines superimposed on the observed data to indicate the nature of the traveltime fit (top panel) obtained by the 2-D ray-trace inversion through each layer (marked by the same layer numbers 1, 2, 3, 4, and 5 as mentioned in Figure 5) of the final velocity model derived (bottom panel). The traveltime data (top panel) is plotted in the reduced-time with 7.0 km/s reduction velocity.

Table 3. Ray-trace inversion results along Jodia-Ansador seismic profile

	Phase Identification	No. of Picks	Average Picking Uncertainty (ms)	RMS Traveltime Residual (s)	Normalized χ^2	No. of rays traced through the model
All P	P_1, P^1, P^2, P^3, P_4, P^4	12,474	41.66	0.041	1.087	12,059
P_1	1	2784	25	0.023	0.994	2776
P^1	2	2300	25	0.026	1.042	2290
P^2	4	1293	50	0.055	0.987	1282
P^3	6	2353	50	0.043	1.143	2185
P_4	3	2054	50	0.047	1.096	1868
P^4	5	1690	50	0.053	1.264	1658

The minimum-parameter V_P model obtained from 2-D ray-trace inversion of first-arrival and reflection traveltime data show corresponding fit of the observed data close to their picking uncertainties (Figure 6). The normalized χ^2 misfit parameter is used for the assessment of data fit, whose values should generally be close to 1.0. This indicates, the inversion will stop once the misfit criteria are satisfied. This is possible, when the observed data for all the SPs show required fit corresponding to their assigned picking uncertainties (Zelt and Smith, 1992; Zelt, 1999). The total number of P-wave data picks used for modeling and inversion are 12,474 (Table 3) for all the twenty-one SPs along the profile. We have classified the P-wave traveltime data picked for first-arrival phases as (P_1, P_4), and corresponding reflection phases as (P^1, P^2, P^3, P^4), which are used for the ray-trace inversion (Table 3). These phases picked are marked with colored dots for all the SPs (SP1 to SP21) along the profile (Figures 3 and 6) as a measure of data quality. The theoretically computed responses obtained from the final V_P model is superimposed on the corresponding observed traveltime data (shown as vertical bars indicating the picking uncertainties) for each SP to demonstrate the nature of data fit along the Jodia-Ansador seismic profile of the Saurashtra basin (Figure 7).

MODEL ASSESSMENT

For the validation of ray-trace inversion, the important factors responsible for establishing the reliability of the V_P model derived along the profile as a measure of the model assessment are, (i) RMS traveltime residual and normalized χ^2 misfit of all the data used in the inversion, (ii) nature of correlation between the observed and computed responses along with the corresponding traveltime misfit, (iii) ray-density/Hits as a measure of number of rays pass through the final velocity model derived (Zelt, 1999). The quantitative parameter estimates of the ray-trace inversion using P-wave traveltime data (Figures 6 and 7) are shown in Table 3 for the seismic profile of Saurashtra basin **(**Figure 1).

Chi-square misfit

To understand the nature of structural changes or model roughness as the inversion proceeds by taking into consideration the corresponding starting P-wave velocity model (Figure 5), the normalized chi-square (χ^2) misfit plays very important role. The χ^2 has converged to 1.087 with RMS residuals of 0.041 s for the final ray-trace inversion (Table 3), which falls from very large value of 18.6 for χ^2 and RMS traveltime residual value of 0.142 s after eighteen non-linear inversion iterations using the correspondng trade-off parameter or damping factor (λ) of 1.0 (Zelt and Smith, 1992).

Ray-density (Hits)

To quantify how the rays are sampled for every cell of the derived V_P model along the Jodia-Ansador seismic profile of Saurashtra basin (Figures 7), we have computed the ray-density or Hits of the model derived (Zelt, 1999). For the computation of ray-density, the cell size of the model is optimally selected in such a way that reasonable number of rays should pass through the cells. However, increase of cell size results in increased number of rays propagate through the cells and hence more Hits. However, the corresponding resolution degrades indicating adverse effect on the model resolution (Behera et al., 2004). Hence, we have judiciously selected 0.5 km × 0.5 km cell size of velocity model (e.g., twice the horizontal and vertical node-spacing) for the ray-density/Hits calculation along the seismic profile so that moderate number of rays should pass through each cell (Figure 8). The Hits plot show the nature of ray-coverage from all the SPs having color scale with corresponding values of Hits (≥ 20) indicated by different colors (Figure 8). Thus, the shallow-crustal V_P model (Figure 9) derived from the ray-trace inversion (Figure 7) is constrained very well based on the nature and continuity of rays passing through them as shown in the ray-density/Hits plot along the profile (Figure 8). Hence, the ray-density/Hits plot provide a very good insight of the quantitative assessment of the rays passing through the final V_P model and considered as one of the important tools for indirect assessment of the model derived (Zelt, 1999).

SHALLOW-CRUSTAL VELOCITY MODEL

The shallow-crustal V_P model down to 10 km depth is obtained (Figure 9) for the 180 km long Jodia-Ansador seismic profile in the Saurashtra basin using 2-D ray-trace inversion (Zelt and Smith, 1992) of first-arrival refraction and reflection traveltime data (Figure 8). The total traveltime data picks of 12,474 are used for the inversion having RMS traveltime-residual of 0.041 s and normalized χ^2 misfit of 1.087 (Table 3), respectively. The geologically plausible V_P model (Figure 9) consists of five layers constrained independently from the corresponding 1-D (Figure 4) and pseudo 2-D velocity models (Figure 5). The first-layer has velocity variations of 4.9-5.1 km/s, which is mainly related to the Deccan Traps (basalts) and are exposed all along the profile (Figure 1). The trap thickness varies from 0.7-1.4 km along the whole profile with 1.2-1.4 km thick cover lying between SP1-SP9 from Jodia towards Rajkot. From Rajkot to Atkot (between SP9-SP15), the trap thickness becomes thin (0.7-0.9 km) and then gradually thickens (0.9-1.1 km) from Atkot towards Ansador (between SP15-SP21). The second layer present below the HVL Deccan Trap is a LVL constrained from the traveltime-skip phenomena using the inversion of first-arrival traveltime data (Greenhalgh, 1977; Whiteley and Greenhalgh, 1979; Sain and Kaila, 1994; Behera et al., 2002, 2004) along with corresponding reflection traveltime for all the SPs using rigorous DLS 1-D inversion (Figure 4) followed by pseudo 2-D modeling (Figure 5) and 2-D ray-trace inversion (Figures 6 and 7) along the profile. The 4.2 km/s velocity obtained for the LVL strongly correlate with

the nearby studies of this region having constrain from the Lodhika well (Dixit et al., 2000; Sain et al., 2002) and Murty et al. (2016), which is confirmed as the Mesozoic sediments hidden below the HVL Deccan Traps. The thickness variation of LVL Mesozoic sediments is constrained as 0.5-1.3 km, which is thinning towards Ansador along the profile (Figure 9). Below the LVL Mesozoic sediments, we have delineated another HVL in which velocity varies from 5.40-5.55 km/s. This HVL may be inferred as Mesozoic volcanics/Tuff as confirmed from the nearby Lodhika and Dhandhuka well lithology (Figure 2). The Mesozoic volcanics has thickness variations of 0.5-1.8 km with maximum thickness attained within 0-90 km profile distance and then gradually becomes thin towards Ansador (0.5-1.0 km) along the profile (Figure 9). This layer has been modeled based on the later-arrival reflection phases (P^3), which are observed prominently in the record sections (Figure 6) with the corresponding ray-trace inversion of different SPs along the profile (Figure 7). The velocity of the layer below the Mesozoic volcanics varies from 5.9-6.1 km/s (Figure 9), which can be considered as the granitic-gneissic basement constrained from the refraction (P_4) phase (Figures 6 and 7). The basement is very shallow (2.0-2.2 km) towards SE of the profile correlating the nearby Dhandhuka well (Figure 2) and deepens to 4.0 km depth towards NW forming horst and graben structure. The thickness of the granitic-gneissic basement varies from 3.0-4.0 km constrained from the ray-trace inversion of reflection phase (P^4) observed from all the SPs along the profile (Figures 6 and 7). The velocity of 6.5 km/s is fixed for the layer lying below this basement, which can be inferred as the rocks of mid-crust or intermediate-crust situated at a shallow depth of 6.0 km due to significant upwarping of the crustal column (Pandey, 2020) as a result of the Reunion mantle plume interaction and impact of the 65 Ma Deccan volcanism.

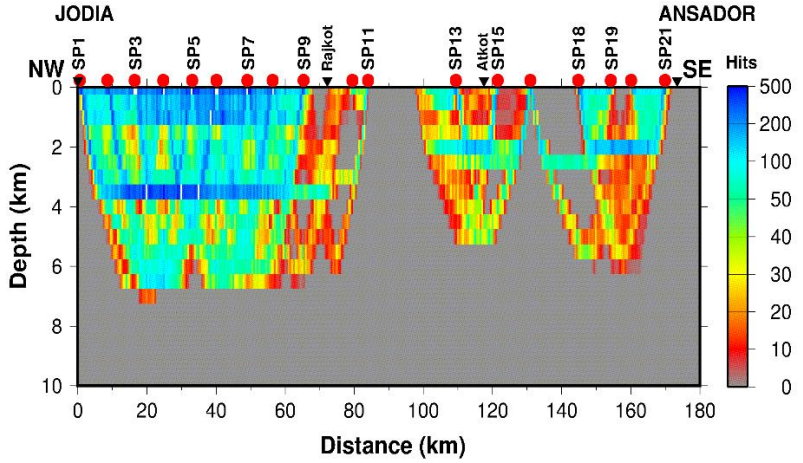

Figure 8. Ray-density or Hits plot of the P-wave velocity model (V_P) with respective color scale representing number of rays passing through the chosen cell size (hit counts). The regions not sampled by rays are shaded in gray color, and SPs are shown as red dots with label along the seismic profile.

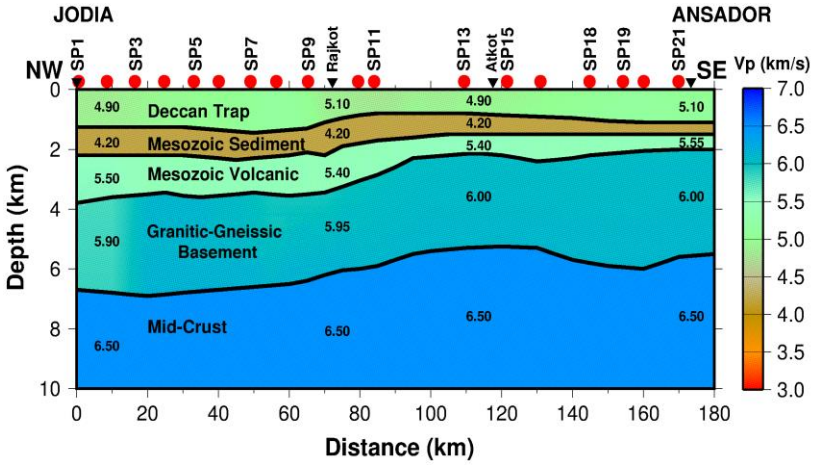

Figure 9. The final V_P model obtained along the NW-SE trending Jodia-Ansador seismic profile in the Saurashtra basin of India using the 2-D ray-trace inversion of P-wave first-arrival seismic refraction and reflection traveltime data (Figure 7). The SP locations along the profile are marked as red dots on the top of the model with corresponding label, and the velocity variation is shown in color scale along with corresponding average velocity values (5.90 km/s) indicated for each layer.

RESULTS AND DISCUSSION

The shallow-crustal V_P model obtained for the NW-SE trending Jodia-Ansador seismic profile in the Saurashtra basin, which is highly heterogeneous having horst and graben structures, is constrained to a depth of 10 km. The intra-volcanic Mesozoic sediments (Figure 9) are masked by ubiquitous spread of thick Deccan Traps all along the profile (Figure 1), which are exposed in an area of 5000 sq. km. towards NE of the Saurashtra basin (Figure 1). They are mainly Lower-Cretaceous older Dhrangadhra sandstones and younger Wadhwan formations confirmed from the lithology of both the nearby Lodhika and Dhandhuka wells (NGRI, 1998; Dixit et al., 2000; Sain et al., 2002). The Dhrangadhra formations mainly comprises of felspathic sandstones, fine-grained argillaceous sandstones, quartzites, sandy shale and clay with occasional thin coal bands. These formations are considered as suitable for reservoir rocks, being porous and permeable. On the other hand, the Wadhwan formations overlie the Dhrangadhra formations conformably (Srivastava, 1963, 1968), but according to Chiplonkar and Badve (1975), the formations lie unconformably. The formation is well exposed towards NE part of executed seismic profile (Figure 1), which was mapped by Fedden (1884) for the first time and named them after the town of Wadhwan around which they are well exposed. This formation is further divided into Surendranagar sandstones and Malachimata/Chamraj formations. Singh et al. (1997) has mentioned in their studies that Mesozoic sediments, in general, exhibit poor organic richness and having poor source rock potential. However, the upper Dhrangadhra sediments display moderate organic richness along with fair gas-prone source rock potential at selected intervals. The oil-window zone has been demarcated between 1650 m to 3230 m in top most upper Dhrangadhra and Lodhika formations (Figure 2), respectively (NGRI, 1998). In the other borewell at Dhandhuka (Figure 2), below 80 m column of Tertiaries, a 505 m thick column of trap was encountered followed by Cretaceous formations (205 m), volcanics of 490 m, Jurassic formations of 80 m and then basement (granites and gneisses) at a depth of 1300 m, which is closely correlated with our results obtained along the profile towards Ansador (Figure 9). The parametric Lodhika well drilled near Rajkot (Figure 2) has revealed in detail the geological setup for the subsurface Mesozoic sediments along with their depositional environment. The oldest formation in the subsurface sequence of Lodhika comprises tuff and amygdaloidal basalt and has been designated as Lodhika formation. The overlying Dhrangadhra formation includes two members, the lower one characterized by rudaceous sediments and claystone, while the upper member is represented by alterations of sandstone and claystone. The Lodhika formation and lower member of Dhrangadhra formation is confined to only subsurface and are not exposed anywhere in the Saurashtra basin. The Dhrangadhra formation grades up into Wadhwan formation, which is dominated by claystone and mature quartz arenite. Deccan Trap flows of 1350 m thickness cap the Wadhwan formation. The depositional formations have been interpreted that the Lodhika formation came into existence under an eruptive igneous regime concomitant with the initiation of rifting, which was followed by the development of horst and graben structures (Figure 9). The subsequent deposition of lower Dhrangadhra member took place under lacustrine and alluvial fan regime, whereas upper Dhrangadhra member was deposited under distal alluvial fan, braided stream, channel sand and marshy environments along with the advancement of rift. The lithological succession of Wadhwan formation represents meandering channel over the suitable continental crust. The Deccan Trap eruption over the Wadhwan formation led to an end of the sedimentation in this area (Figure 1). The Mesozoic sediments have been imaged all along the profile having 4.2 km/s velocity with thickness variations of 0.5-1.3 km that sandwiched between exposed Deccan Traps and underlying the older Mesozoic volcanic flow, which also strongly correlate with the results obtained by Sain et al. (2002) in this region from another small 45 km long seismic profile passing through the Lodhika well. The derived V_P model clearly demonstrate the presence of LVL Mesozoic sediments hidden below the Deccan Traps has potential for hydrocarbon accumulation, which is also confirmed from the nearby drilled wells of Lodhika and Dhandhuka (Figure 2).

The Deccan Traps in the Saurashtra basin is characterized by large number of dykes, volcanic and plutonic centres, the major ones being Girnar, Osham, Alech, Barda and Chogat Chamardi (Merh, 1995). These hills comprising the Deccan basalt eruptions and intrusions seem to be arranged in a broad arcuate outcrop, concave northward (Figure 1). The continuity and extent of thick (0.7-1.4 km) HVL Deccan Traps lie both laterally and vertically along with ubiquitous presence in the Saurashtra basin indicating large-scale volcanic activity with outpouring of tholeiitic flood basalts or lavas during the Deccan volcanism (~65 Ma), when Indian plate was located above the Reunion plume and subsequent rifting of Seychelles from Indian plate. The Mesozoic volcanics (older basalts) underlying the Mesozoic sediments play very important role for making a channel for the deposit of the intra-volcanic sediments without any dispersal and acts as a major reservoir rock potential for the hydrocarbon exploration in this region. The crystalline granitic-gneissic basement (5.9-6.1 km/s) is highly undulating having horst and graben structures that indicate large-scale tectonic activity with significant upwarping and presence of mid-crustal rocks (6.5 km/s) at very

shallow depth of 6.0 km. The intense tectonic activity has resulted in the presence of deep-basinal faults controlled by the horst and graben structures and significant upwarping within 80-140 km segment of the profile towards Atkot and depressions towards Jodia and Ansador (Figure 9).

CONCLUSIONS

Based on the 2-D ray-trace modeling and inversion of seismic refraction and reflection traveltime data along the 180 km long NW-SE trending Jodia-Ansador seismic profile in the Saurashtra basin of India, the following conclusions are drawn.

(i) The top layer is mainly covered with highly heterogeneous and rugose Deccan Traps, which extends to maximum depth of 1.4 km with velocity variations of 4.9-5.1 km/s along the profile, that obscure and mask all the subsurface geological features.

(ii) The LVL intra-volcanic Mesozoic sediments (4.2 km/s) delineated from the traveltime-skip phenomena, are hidden below the HVL Deccan Traps and sandwiched above the another high-velocity (5.4-5.55 km/s) Mesozoic basaltic layer, may play an important role in the accumulation of hydrocarbons. This LVL has been constrained from the nearby Lodhika and Dhandhuka wells drilled by ONGC as parametric wells for the hydrocarbon exploration in the Saurashtra basin. The Mesozoic sediments are exposed in the NE part of the basin as Dhrangadhra and Wadhwan sandstone formations.

(iii) The crystalline basement is mainly granitic and gneissic in composition with velocity variations of 5.9-6.0 km/s, which is highly undulating forming horst and graben structures, attains maximum depth of 4 km near Jodia. It is constrained by deep-basinal faults with significant upwarping near Atkot and gradually shallowing to 2 km depth towards Ansador along the profile.

(iv) The high-velocity (6.5 km/s) mid-crustal rocks are imaged at very shallow depth of only about 6.0 km with significant upwarping correlating the basement geometry and may be due to complex tectonic activity and impact of Deccan volcanism in this region.

(v) The V_P model derived to a maximum depth of 10 km has been constrained from model parameterizations, RMS traveltime residuals, normalized χ^2 misfit, ray-density or Hits as well as nearby well lithology of the study region.

ACKNOWLEDGEMENTS

We sincerely thank Dr. Prakash Kumar, Director, CSIR-NGRI for according permission to publish this paper. Prof. Colin A. Zelt of Rice University, USA is gratefully acknowledged for using his RAYINVR codes. We sincerely thank Prof. P. R. Mohanty, an Anonymous Reviewer and Dr. O. P. Pandey, Chief Editor of The Journal of Geophysical Union (JIGU) for their comments and suggestions to improve the quality of the paper. We acknowledge and thank the CSS team members of CSIR-NGRI for seismic data acquisition in the Saurashtra basin of India. This work pertains to the scientific research contribution of CSIR-NGRI under MLP-7012-28 (PK) with Ref. No. NGRI/Lib/2025/Pub-62.

Author Credit Statement

Renuka Kolluru: Data curation, data analysis, methodology, writing original-draft. Laxmidhar Behera: Conceptualization, data curation, methodology, writing original-draft, data analysis, editing and revision, funding acquisition, resources and supervision

Data Availability

The seismic data used in this study can be made available by requesting to the Director, CSIR-NGRI (E-mail: director.ngri@csir.res.in) as per CSIR-NGRI data policy.

Compliance with Ethical Standards

The authors declare that they have no conflict of interest and adhere to the copyright norms.

References

Behera, L., 2011a. Seismic imaging of Mahanadi delta and its tectonic significance. Lap Lambert Academic Publishing GmbH and Co. KG, Germany.

Behera, L., 2011b. Crustal tomographic imaging and geodynamic implications toward south of Southern Granulite Terrain (SGT), India. Earth Planet. Sci. Letts., 309(1-2), 166-178.

Behera, L. and Sarkar, D., 2011. Tomographic imaging of large volcanic province due to intense magmatism in the Mahanadi delta of eastern India. Phys. Earth Planet. Int., 189, 142-150.

Behera, L. and Sen, M. K., 2014. Tomographic imaging of sub-basalt Mesozoic sediments and shallow basement geometry for hydrocarbon potential below the Deccan Volcanic Province (DVP) of India. Geophys. J. Int., 199, 296-314.

Behera, L. and Kumar, D., 2022. Deep crustal structure and compositions for tectonic and geodynamic implications of the Dharwar Craton (Southern India) inferred from 3-C wide-angle seismic data. J. Asian Earth Sci., 227(105092), 1-37.

Behera, L., Sain, K., Reddy, P. R., Rao, I. B. P. and Sarma, V. Y. N., 2002. Delineation of shallow structure and Gondwana graben in the Mahanadi delta, India, using forward modeling of first-arrival seismic data. J. Geodyn., 34, 127-139.

Behera, L., Sain, K. and Reddy, P. R., 2004. Evidence of underplating from seismic and gravity studies in the Mahanadi delta of eastern India and its tectonic significance. J. Geophys. Res., 109(B12311), 1-25.

Behera, L., Kolluru, R. and Singh, B., 2021. Imaging Mesozoic sediments in Deccan Volcanic Province of India: Inferences from seismic and gravity studies. J. Geol. Soc. India, 97, 1260-1273.

Biswas, S. K., 1982. Rift basins in the western margin of India and their hydrocarbon prospects. Bull. AAPG, 66(10),1497-1513.

Biswas, S. K., 1987. Regional tectonic framework, structure and evolution of the western marginal basins of India. Tectonophysics, 135, 307-327.

Biswas, S. K. and Deshpande, S. V., 1983. Geology and hydrocarbon prospects of Kutch, Saurashtra and Narmada basins, In: L.L. Bhandari, B.S. Venkatachalam, R. Kumar, S.N. Swamy, P. Garga and D.C. Srivastava (Eds.), Petroliferous basins of India. Petrol. Asia J., 6(4), 111-126.

Biswas, S. K., Bhasin, A. L. and Ram, J., 1993. Classification of Indian sedimentary basins in the framework of plate tectonics. Proc. Second Sem. Petrol. Basins. India, 1, 1-46.

Červený, V., Molotkov, I. A. and Pšenčík, I., 1977. Ray Methods in Seismology, Prague, University of Karlova.

Chiplonkar, G. W. and Badve, R. M., 1975. Stratigraphy of the area around Wadhwan, Saurashtra, Gujarat State. Rec. Res. Geol., Hindustan Publ., Delhi, 1**,** 229-239.

Dixit, M. M., Satyavani, N., Sarkar, D., Khare, P. and Reddy, P. R., 2000. Velocity inversion in the Lodhika area, Saurashtra peninsula, western India. First Break, 18, 499-504.

Fedden, F., 1884. Geology of Kathiawar peninsula in Gujarat. Mem. Geol. Soc. India, 21(2), 78-125.

Firbas, P., 1987. Tomography from seismic profiles. In: Nolet, G. and Dordrecht, R. (Eds.). Seismic Tomography, p. 189-202.

Greenhalgh, S. A., 1977. Comments on 'The hidden layer problem in seismic refraction work'. Geophys. Pros., 25, 179-181.

Huang, H., Spencer, C. and Green, A., 1986. A method for the inversion of refraction and reflection travel times for laterally varying velocity structures. Bull. Seism. Soc. Am., 76, 837-846.

Kumar, D. and Behera, L., 2024. Upper-crustal structure, compositions and tectonic settings obtained from Perur-Chikmagalur 3-C seismic profile of Archean Dharwar Province, southern India. Acta Geophysica, 72, 2521-2553.

Lutter, W. J., Nowack, R. L. and Braile, L. W., 1990. Seismic imaging of upper crustal structure using travel times from the PASSCAL Ouachita experiment. J. Geophys. Res., 95, 4621-4631.

Menke, W., 1984. Geophysical Data Analysis: Discrete Inverse Theory; Academic press, Orlando.

Merh, S. S., 1995. Geology of Gujarat; Geol. Soc. Ind., Bangalore, India.

Murty, A. S. N., Sain, K., Sridhar, V., Prasad, A. S. S. S. R. S. and Raju, S., 2016. Delineation of Trap and sub-trappean Mesozoic sediments in Saurashtra peninsula, India. Curr. Sci., 110(9), 1844-1851.

NGRI, 1998. Integrated geophysical studies for hydrocarbon exploration in Saurashtra, India. NGRI Technical Report No. NGRI-1998-Exp-237.

Pandey, O. P., 2020. Geodynamic evolution of the Indian shield: Geophysical aspects; Springer Nature, Switzerland.

Plummer, Ph. S., 1994. Mesozoic source rocks and hydrocarbon potential of the Seychelles offshore. J. Petrol. Geol., 17(2), 157-176.

Sain, K. and Kaila, K. L., 1994. Inversion of wide-angle seismic reflection times with damped least-squares. Geophysics, 59, 1735-1744.

Sain, K., Zelt, C. A. and Reddy, P. R., 2002. Imaging of sub-trappean Mesozoics using travel time inversion of wide-angle seismic data in the Saurashtra peninsula of India. Geophys. J. Int., 150, 820-826.

Singh, D., Alat, C. A., Singh, R. N. and Gupta, V. P., 1997. Source rock characteristics and hydrocarbon generating potential of Mesozoic sediments in Lodhika area, Saurashtra basin, Gujarat, India. Proceed. Second Int. Petrotech Conf. Exhib., Petrotech-97, New Delhi, 205-220.

Spence, G. D., 1984. Seismic structure across the active subduction zone of western Canada. PhD Thesis, University of British Columbia.

Spence G. D., Clowes, R. M. and Ellis, R. M., 1985. Seismic structure across the active subduction zone of western Canada. J. Geophys. Res., 90, 6754-6772.

Talukdar, K. and Behera, L., 2018. Sub-basalt imaging of hydrocarbon-bearing Mesozoic sediments using ray-trace inversion of first-arrival seismic data and elastic finite-difference full-wave modeling along Sinor-Valod profile of Deccan Syneclise, India. Pure Appl. Geophys., 175, 2931-2954.

Tewari, H. C., Dixit, M. M. and Murty, P. R. K., 1995. Use of traveltime skips in refraction analysis to delineate velocity inversion. Geophys. Pros., 43, 793-804.

Srivastava, P. K., 1963. Geology of Saurashtra. ONGC Report (unpublished).

Srivastava, P. K., 1968. A note on the Quaternary geology of Saurashtra peninsula. Quart. Geol. Min. Met. Soc. India, 40(2), 55-64.

White, R. and M^{c}Kenzie, D., 1989. Magmatism at rift zones: the generation of volcanic continental margins and flood basalts. J. Geophys. Res., 94, 7685-7729.

Whiteley, R. J. and Greenhalgh, S. A., 1979. Velocity inversion and the shallow seismic refraction method. Geoexploration, 17**,** 125-141.

Yilmaz, Ö., 2001. Seismic Data Analysis. Soc. Explor. Geophys.; Tulsa, OK, USA.

Zelt, C. A., 1999. Modeling strategies and model assessment for wide-angle seismic traveltime data. Geophys. J. Int., 139, 183-204.

Zelt, C. A. and Ellis, R. M., 1988. Practical and efficient ray tracing in two-dimensional media for rapid traveltime and amplitude forward modeling. Can. J. Exp. Geophy., 24, 16-31.

Zelt, C. A. and Smith, R. B., 1992. Seismic travel time inversion for 2-D crustal velocity structure, Geophys. J. Int., 108, 16–34.

Received on: 15-05-2025; Revised on: 25-06-2025 ; Accepted on: 26-06-2025

J. Ind. Geophys. Union, 29(4) (2025), 236-247
https://doi.org/10.71122/JIGU.29(4)2025.0023

Mapping and demarcating gold mineralization in Jashpur and Raigarh districts (Chhattisgarh) from Analytic Hierarchy Process and geophysical approach

Vishal Bajirao Nayakwdi[1] and Dewashish Kumar[1,2]*
[1]CSIR-National Geophysical Research Institute, Hyderabad -500007, India
[2]AcSIR – Academy of Scientific and Innovative Research, Ghaziabad, India
*corresponding author: dewashishkumar@ngri.res.in; dkumar.ngri@gmail.com

ABSTRACT

Mineral exploration is a vital activity for the sustainable and economic development of any region. This study focuses on the Jashpur and Raigarh districts of Chhattisgarh state in India. We integrate geology, electrical tomography, resistivity, induced polarization (IP) and Geographic Information Systems (GIS) to identify high potential zones of hydrothermal gold deposits. We followed a data driven approach that utilizes multiple data sets pertaining to geological, geochemical and geophysical studies. These data sets in the Analytic Hierarchy Process (AHP) were utilized to provide weights to various evidence layers through expert judgment and literature review. The weighted layers were combined to generate mineral prospective maps, which identified areas with significant economic potential. This study demonstrates the effectiveness of integrating state-of-the-art electrical tomography method and GIS in mineral exploration by providing a robust framework for identifying economically viable gold and other sulphide mineral deposits. Mineral Prospect Map (MPM) indicates that 130.40 sq. km area comes under the class of high mineralized zone. The results contribute to the sustainable development of the Jashpur and Raigarh districts, offering valuable insights for mineral resource management and exploration strategies.

Keywords: Chhotanagpur Gneissic Complex, Electrical resistivity tomography, Time domain IP, Mineralization, Chhattisgarh, India

INTRODUCTION

Finding new mineral deposits and utilising prospective zones within the region of interest for economic and sustainable growth, is a major motive in mineral exploration (Haldar, 2018). There is hidden information on geo-evidential features, which are considered indicators for exploring appropriate minerals and deposit types. Complexity arises due to the wide variety of geological processes, large spatial areas involved and the need to interpret data both from the surface and subsurface findings (Mansouri et al., 2017). Mineral potential mapping in recent years has been categorised as either data driven or knowledge driven (Pradhan et al., 2022; Zuo et al., 2023). A knowledge driven approach was used for this study. Multiple data sets or maps are required to be collected, analysed and integrated for mineral prospective mapping (MPM) in the region of interest to identify mineral-rich zones.

Present study aims to determine high potential zones of hydrothermal gold deposits in the Jashpur and Raigarh districts of Chhattisgarh in India, where many previous studies have also been done. For example, Geological Survey of India (GSI), Geomysore Services and MECL, explored gold as a G3 reconnaissance survey. Dora (2014) also studied ten different sites from Bastar craton for PGE mineralisation. Similarly, Kumar et al. (2017) studied and reported positive IP results and GSI also reported gold mineralisation around the study area (Kalsotra and Narang, 1983). An Analytic Hierarchy Process (AHP) method was applied to determine the weights of five different evidential layers, obtained from geological and geochemical studies as well as literature review, to demarcate high and economically explorable gold deposits. Prospectivity maps were created by merging the weighted evidential layers using the AHP technique (Du et al., 2016). As such, present study integrates high resolution electrical resistivity, IP tomography geophysics and GIS data to demarcate the mineral potential zones. State-of-the-art electrical resistivity tomography (ERT) and induced polarisation (IP) geophysical methods were used to study in detailed the subsurface geological structure(s) and mineralised zones within the rock mass of a geological setting in the study area. Subsequently, ERT and IP results were used to validate the mineral prospective map (MPM) as obtained in the present study.

STUDY AREA, GEOLOGY AND DRAINAGE SYSTEM

The study area falls in Jashpur and Raigarh districts of Chhattisgarh state, India (**Figure 1**). This study region is enriched with different types of mineral deposits and also known for its complex geological formations. It has a long history of mineral exploration activities. The geographic coordinates of the study area are 22°17' to 23°15' N and 83°30' to 84°24' E . It falls in toposheets 64N/10, 64N/11, 64N/14 and 64N/15. The study area comprises different geological features like, fractures, faults, lineaments and dykes (Figure 2). It exposes Precambrian rocks, represented predominantly by biotite granites and gneisses with xenoliths of older metamorphic and basic rocks, which are traversed by quartz veins (Kalsotra and Narang, 1983; Kumar et al., 2017) (Figure 3). It is also comprised of Lower Gondwana and Chhotanagpur gneissic complex rocks (Figure 3), exposed along an E-W belt and have numerous stringers and veins of quartz traversing mostly in NW-SE, NE-SW and E-W directions. Pegmatites, meta basic dykes, aplite veins, basic dykes and quartz veins are also found in the study area (Choudhary, 1969; Mishra et al., 2008).

The study area comprises undulating topography with numerous knolls, hillocks and linear ridges rising over a general level of 365 m above mean sea level. Ib and Maini

rivers are the most important water channels in Jashpur district, which drains from north to south in the study region. Both river have their source in the Khuria highlands in the north. The Maini river is flowing south-easterly in the western part and north-eastern in the eastern part with numerous meanders and thus forms the chief drainage system of the area. It is a 6th order stream along with a number of 4th and 3rd order streams joining it from north and south direction.

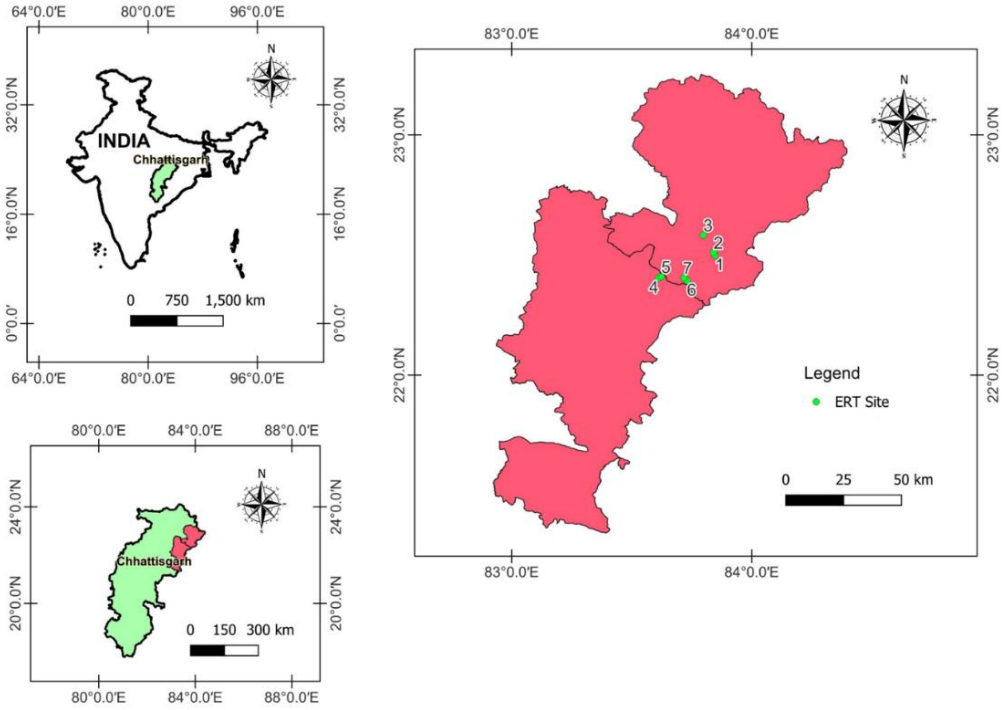

Figure 1. Location of study area showing electrical tomography sites in Jashpur and Raigarh districts of Chhattisgarh state.

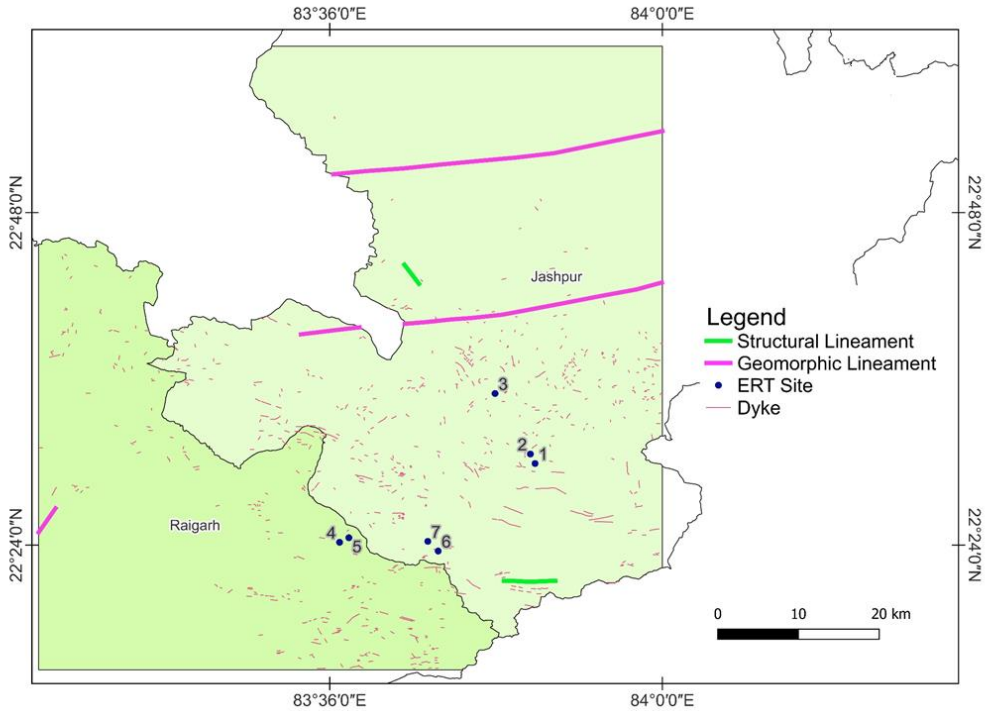

Figure 2. Structural map of the study area showing location of dykes, structural and geomorphic lineaments.

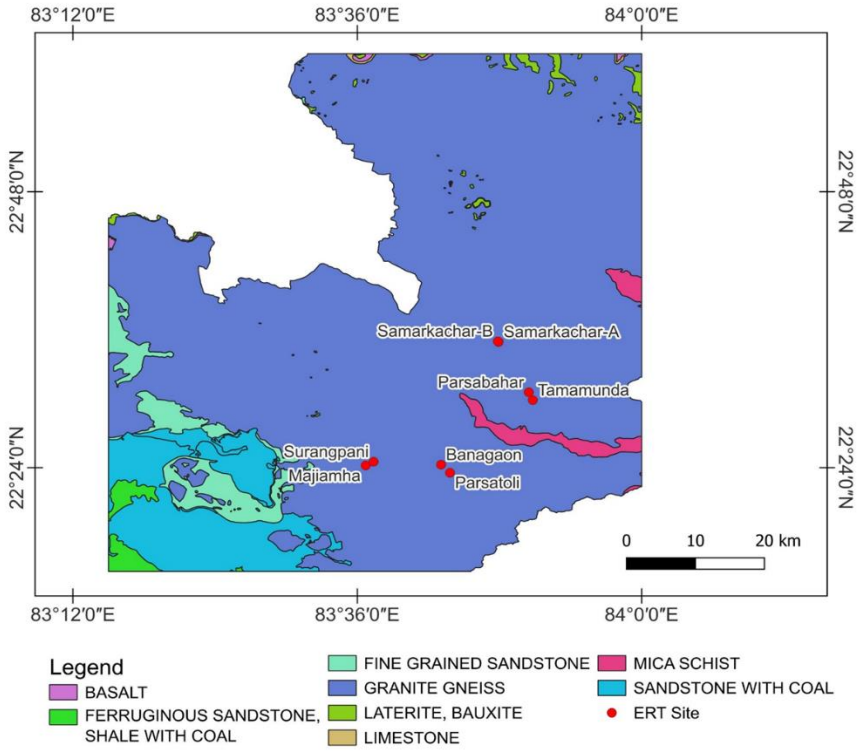

Figure 3. Detailed geological map of the study area along with the location of ERT sites.

METHODOLOGY

Electrical tomography

Electrical resistivity and induced polarization (IP) surveys were performed using a gradient array to acquire subsurface resistivity and chargeability in order to know the variations of the rock mass in terms of resistivity and chargeability property in the present geological setting. Electrical Tomography data were collected at 7 different sites (Figure 1) using the state-of-the-art 4-channel ABEM Terrameter LS equipment® (ABEM, 2012). Good quality dataset are collected for mapping mineralization. IP survey resulted in chargeability, that acts as a prominent indicator for mineral deposition, which aids along with the resistivity in the detection and evaluation of sulphide minerals associated with gold deposits (Kumar et al., 2017, 2022).

GIS approach

In the present work, we used different thematic maps namely lithology, structural discontinuity, distribution of pathfinder elements in stream sediments, dykes and their lithology for detailed analysis of mineralization. The stream network (Figure 4a) was extracted from the DEM file in ArcGIS for further analysis. This stream network was used for network analysis and traced upstream to find source rock regions to demarcate high mineral prospect areas. The GIS algorithm is used to calculate the drainage network. For the drainage network analysis, Shuttle Radar Topographic Mission (SRTM) Digital Elevation Model (DEM) was used. The flow direction was estimated using a slope, while stream network analysis can be estimated from a drainage network together with flow direction.

Stream sediment sampling data contains all types of elements present in the sample (Figure 4b), which gives the regional geochemistry of the study area. This data has been used to understand the geochemical background. Further, stream sediment sampling data is used for preparing anomaly maps of pathfinder elements. The stream sample points were interpolated to prepare the anomaly map using the Inverse Distance Weighted (IDW) interpolation method in ArcGIS (Cheng et al., 1994; Cheng, 1999) (Figures 5 and 6). This method uses precious elements, which are used as pathfinders for gold mineral deposits which are Te, As, Sb, Ag, Bi, Cu, Mo and Zn (Bullock et al., 2017; Barnes, 2018; Ge et al., 2023). IDW interpolation of Au, Te, As and Sb as a pathfinder for gold deposit is shown in Figure 5. The thematic map resulted from the intersection area between dyke buffers and river buffers with a 1000 m buffer to both the features, is shown in Figures 5 - 7.

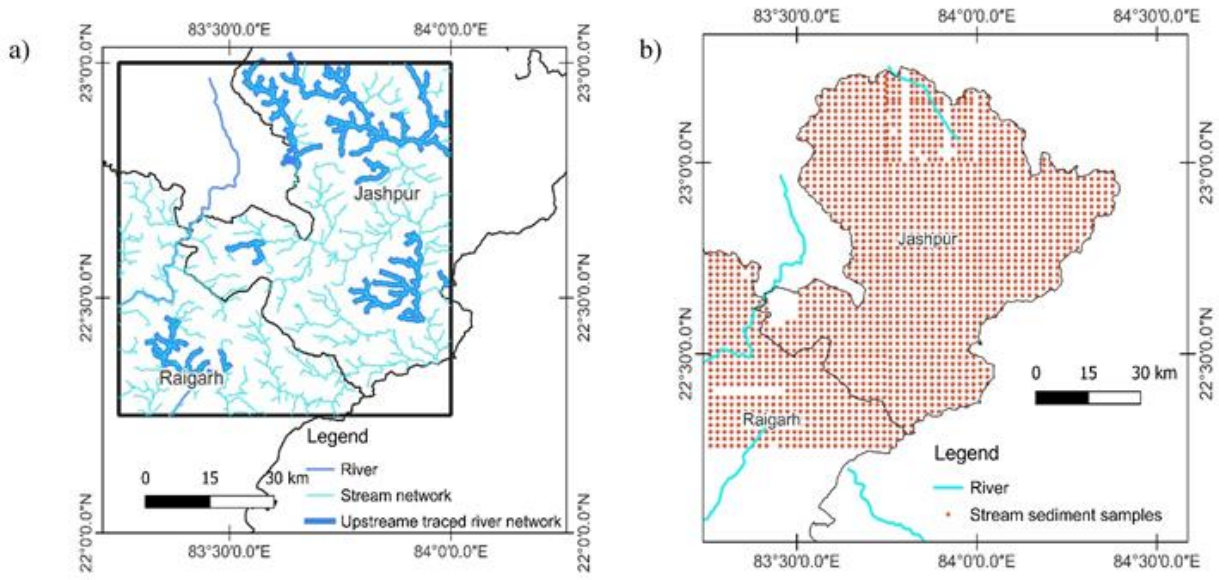

Figure 4. **(a)** River and stream network within the study area. **(b)** Stream sediment sampling locations.

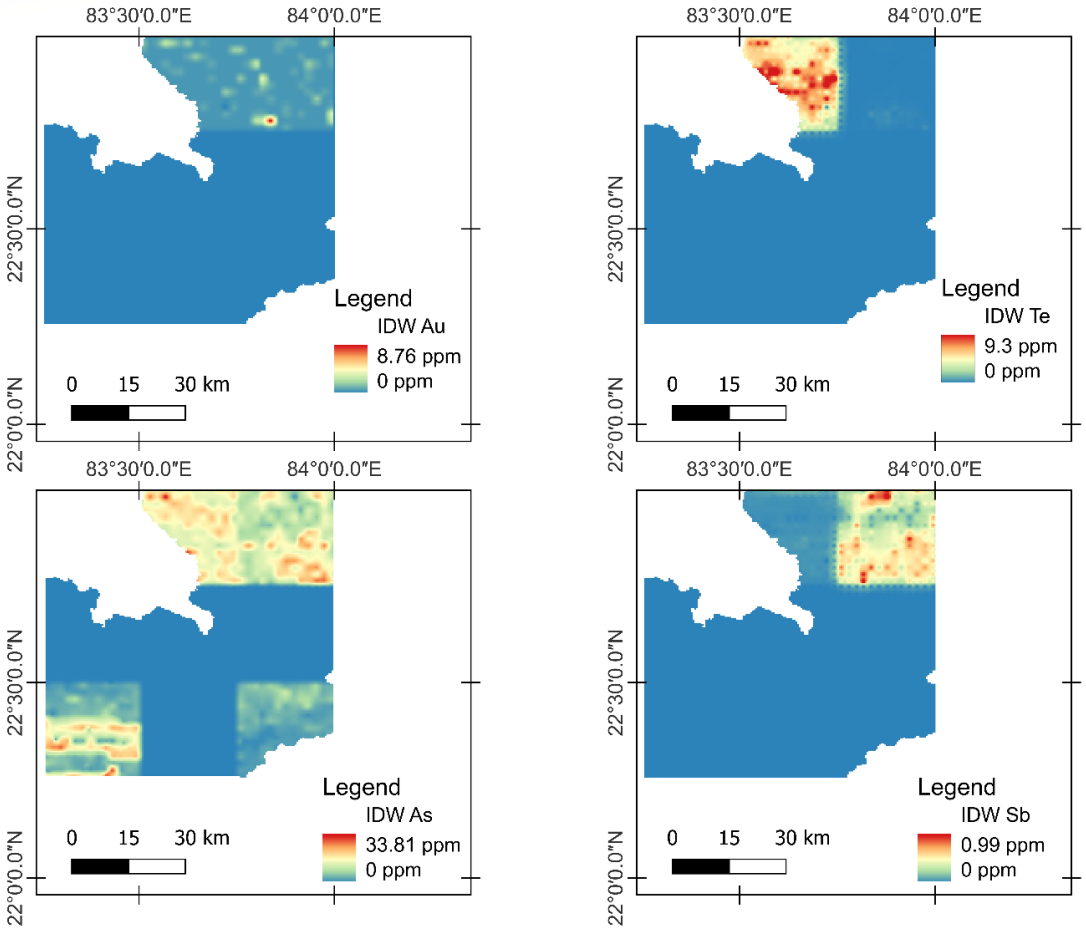

Figure 5. Inverse Distance Weighted (IDW) interpolation of Au, Te, As and Sb pathfinder element in the study area.

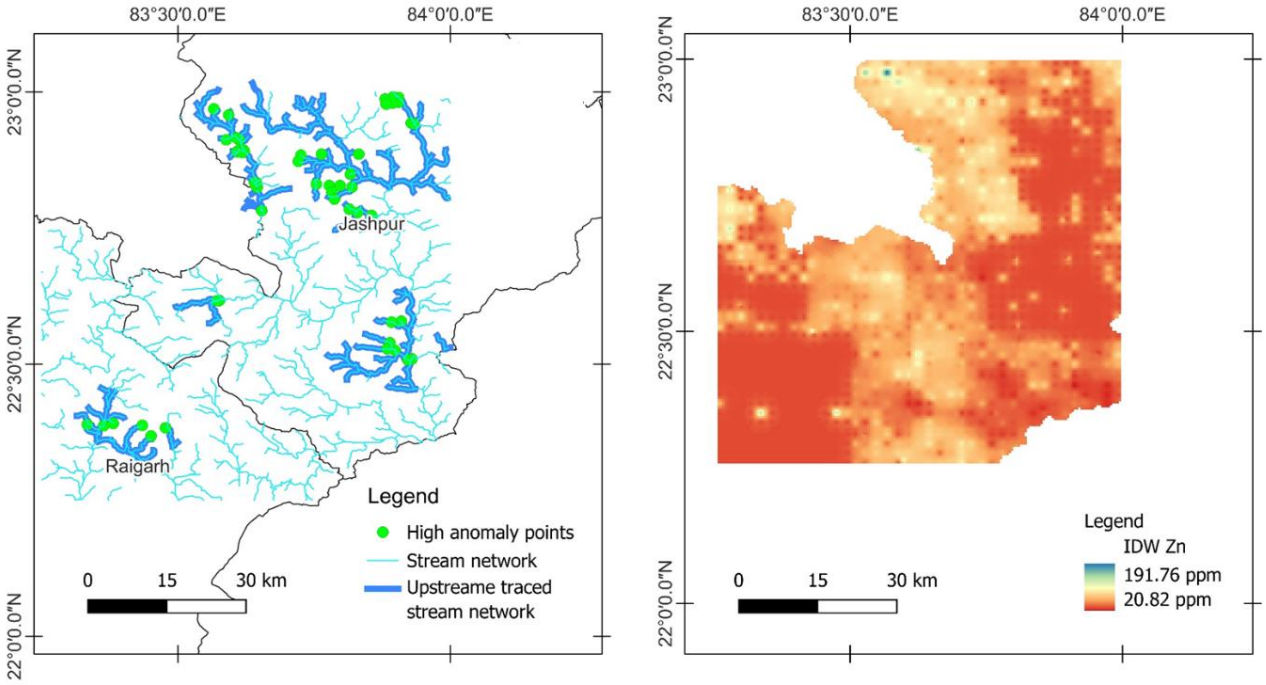

Figure 6. Upstream traced network from high anomaly zones to possible source rocks (left panel) and Inverse Distance Weighted (IDW) Zn anomaly (right panel) in the study area

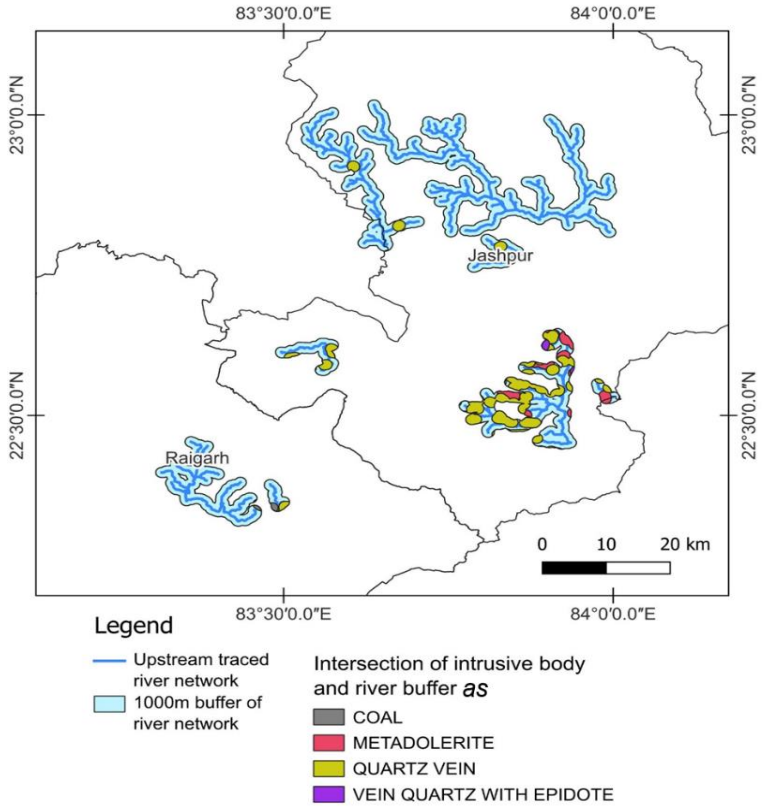

Figure 7. The intersection of intrusive body and river buffer in the study area.

In addition, vector input layers namely lithology, structural discontinuity, upstream traced river network and buffers (Figures 2-7) were converted into grid and resampled, using Quantum Geographic Information System (QGIS) and then the grid cells of the input thematic layers was resized. Thereafter, reclassification using GRASS reclass algorithms was carried out to put all the factor classes. This reclassification to a scale of 1 to 5 was made to harmonize the results so obtained. This was the final input, which was then subjected to Weighted Overlay Analysis (WOA). The final consistency ratio (CR) is obtained by the ratio of the consistency index (CI) to the random index (RI) following Saaty (1977). The CR ratio indicates the level of consistency that is expected when randomly completing reciprocal matrices using values on a scale of 1-9. It is used to determine whether the evaluations are adequately consistent or not. The value of 0.1 is considered to be the maximum acceptable limit for CR. If the final CR surpasses this threshold, the review process must be repeated in order to enhance coherence of the evaluation.

Weighted Overlay Analysis (WOA)

The weighted overlay analysis is a modelling method for constructing an integrated map by merging the geometry and characteristics of every related geological layer in a GIS environment (Ramadhani Mussa et al., 2020). Weighted overlay analysis is applied to achieve a cumulative possibility model that represents the potential mineral zones in a given region as a result of the selected parameters and their corresponding groups. A comprehensive literature review was conducted, to ensure the accuracy and objectivity of the ranking. In pairwise comparison, matrix parameters were ranked on a scale from 1 to 9. For equal influence 1 and as the influence of other parameters decreases, the scale shifts towards a higher number. All thematic maps (Table 1) were used for WOA. For WOA, we assigned weightage based on the literature review. Within the thematic map, all classes were classified in the range of 1-5 based on their importance and correlation with gold mineralization (Rahmati et al., 2015; Ibrahim-Bathis and Ahmed, 2016; Andualem and Demeke, 2019; Abijith et al., 2020).

Additionally, the Multicriteria Decision Analysis (MCDA) method is also integrated for preparing mineral prospect maps. It provided unbiased decisions about the highest possibility of mineralization based on all 5 factors considered in the study (Table 1). In this process, we did a pairwise comparison matrix (Table 2). Ultimately, the value of each cell in the input raster, was multiplied by the normalized weighted values of each raster layer. This process finally resulted in the calculation and the evolution of the mineral prospect map (MPM). The computations were performed using the raster calculator tool within the ArcGIS environment.

Table 1. Thematic maps and their priority with ranks

Category	Priority (%)	Rank
Lithology (1)	34.2	1
Lineament (2)	29.2	2
IDW (3)	13	4
Intersection (4)	15	3
Dyke buffer (5)	8.6	5

Table 2. Comparison matrix of various thematic maps

Thematic Maps	Lithology (1)	Lineament (2)	IDW (3)	Intersection (4)	Dyke buffer (5)
Lithology (1)	1.00	1.00	3.00	2.00	5.00
Lineament (2)	1.00	1.00	3.00	2.00	2.00
IDW (3)	0.33	0.33	1.00	1.00	2.00
Intersection (4)	0.50	0.50	1.00	1.00	2.00
Dyke buffer (5)	0.20	0.50	0.50	0.50	1.00

RESULTS

Interpretation of electrical tomography models at different sites

(i) Tamamunda

The resistivity at Tamamunda site show large resistivity contrast from 20–13,300 Ohm.m (Figure 8a), suggesting diverse mineralogical composition within the subsurface rocks. Whereas, the chargeability varies from 1.5 – 12 mV/V (Figure 8b). A thick weathered layer ~15 m with a resistivity <100 Ohm.m is seen in the near surface zone (Figure 8a). The model resistivity indicates high resistivity granitic-gneissic rocks as basement, followed by uniform high resistivity at deeper depths. This resistivity model also indicates the presence of a uniform resistivity body (igneous intrusive structure) (Figure 8a). Towards northern and southern side, the model revealed high chargeability 8.42 mV/V anomaly between 20 to 40 m depth (Figure 8b) corresponding to moderate resistivity ~1433 Ohm.m at the same depths (Figure 8a). Hydrothermal fluid deposited in the bedrock cracks and the mineralisation have resulted in moderate chargeability, which is also ascribed to the concentration of low-grade minerals. In contrast, from north to south, it shows low chargeability variation (Figure 8b).

(ii) Majiamha

The resistivity model indicates weathered rock with an average thickness of 20 m towards the eastern end of the profile, which shows low resistivity <100 Ohm.m (Figure 9a). Further, from 20 m to deeper depths, hard rock is mapped till 131 m depth (Figure 9a). Two prominent low resistivity anomaly from the middle to the western end of the resistivity model, indicates highly fractured rock mass due to the intense rock fracturing (Figure 9a). We can further see a low IP zone corresponding to the same low resistivity anomaly indicating water saturated fractured zone within the rock mass.

The resistivity model also indicates granitic plutonic intrusion from the deeper depths (Figure 9a). Very high chargeability is seen at the right corner towards east end but at deeper depths from 100 to until 131 m depth the chargeability is >11 mV/V (Figure 9b). This site is foliated geologically. Compositionally, hard bedrock is granodiorite. From the lateral distance 160 m away from the west end of the profile, it shows very high contrasting resistivity from the near surface layers to bottom 131 m depth (Figure 9a). A zone of low resistivity <600 Ohm.m and low chargeability up to 1 mV/V, indicate weathered rock mass (Figure 9 a, b).

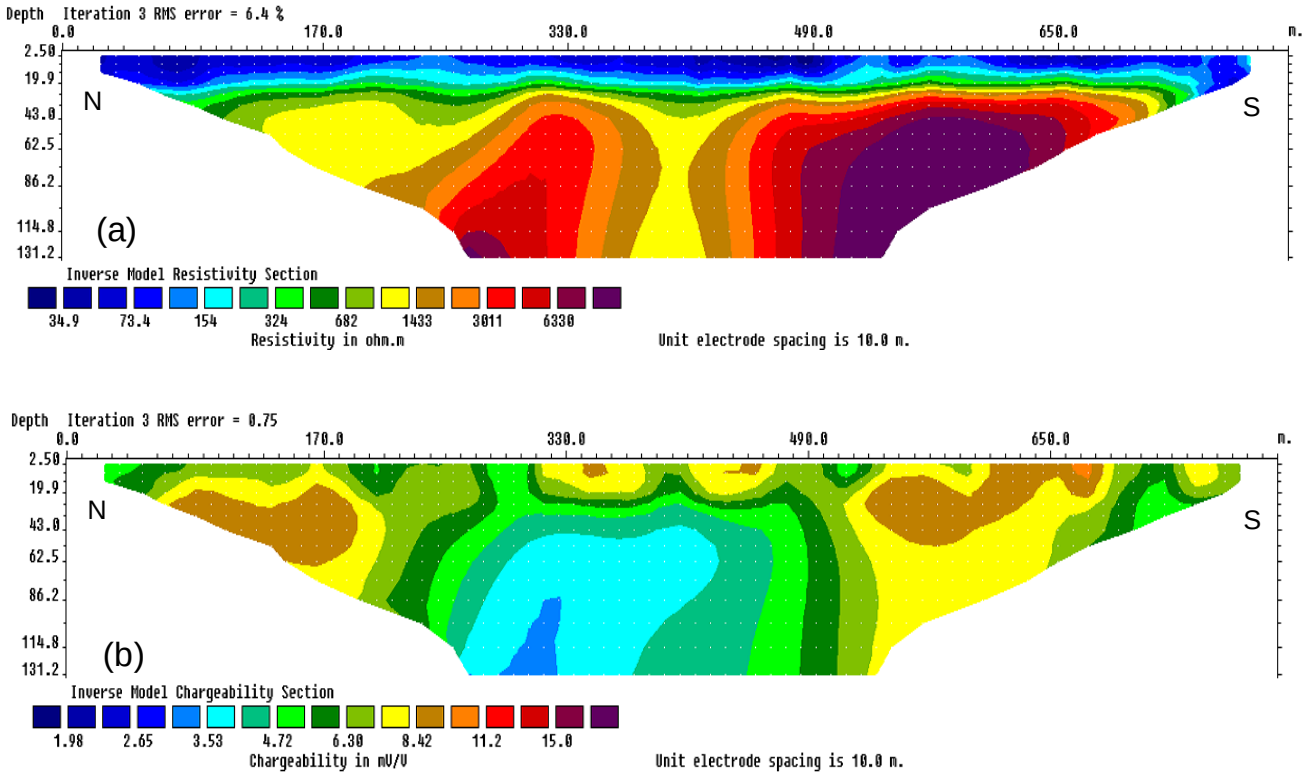

Figure 8. (a) 2D inverted resistivity model with two high resistivity bodies separated by a comparatively low resistivity zone, showing a resistivity contrast of ≥3000 Ohm.m. **(b)** Chargeability model depicting a large variation in chargeability from 3 to 7 mV/V just below the low resistivity anomaly at the Tamamunda site.

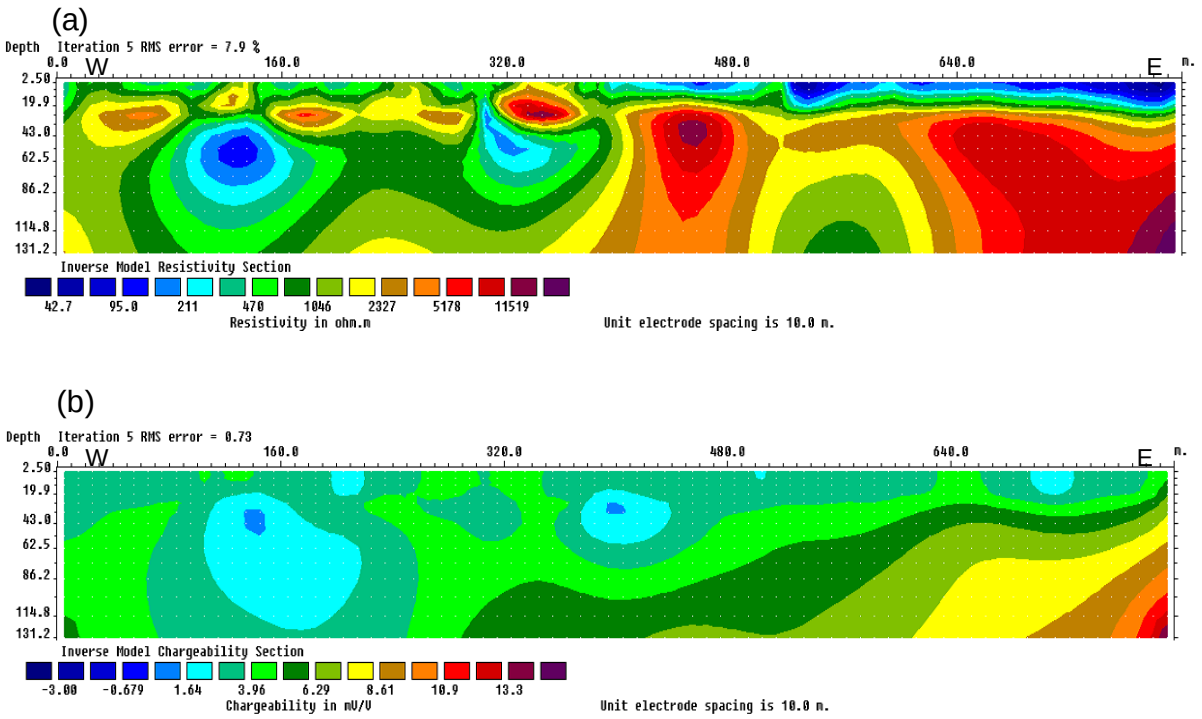

Figure 9. (a) 2D inverted resistivity model showing distorted geological structure with a large resistivity contrast of ≥10,000 Ohm.m at Majiamha site. **(b)** Chargeability model with a contrasting chargeability anomaly from west to east at the same site.

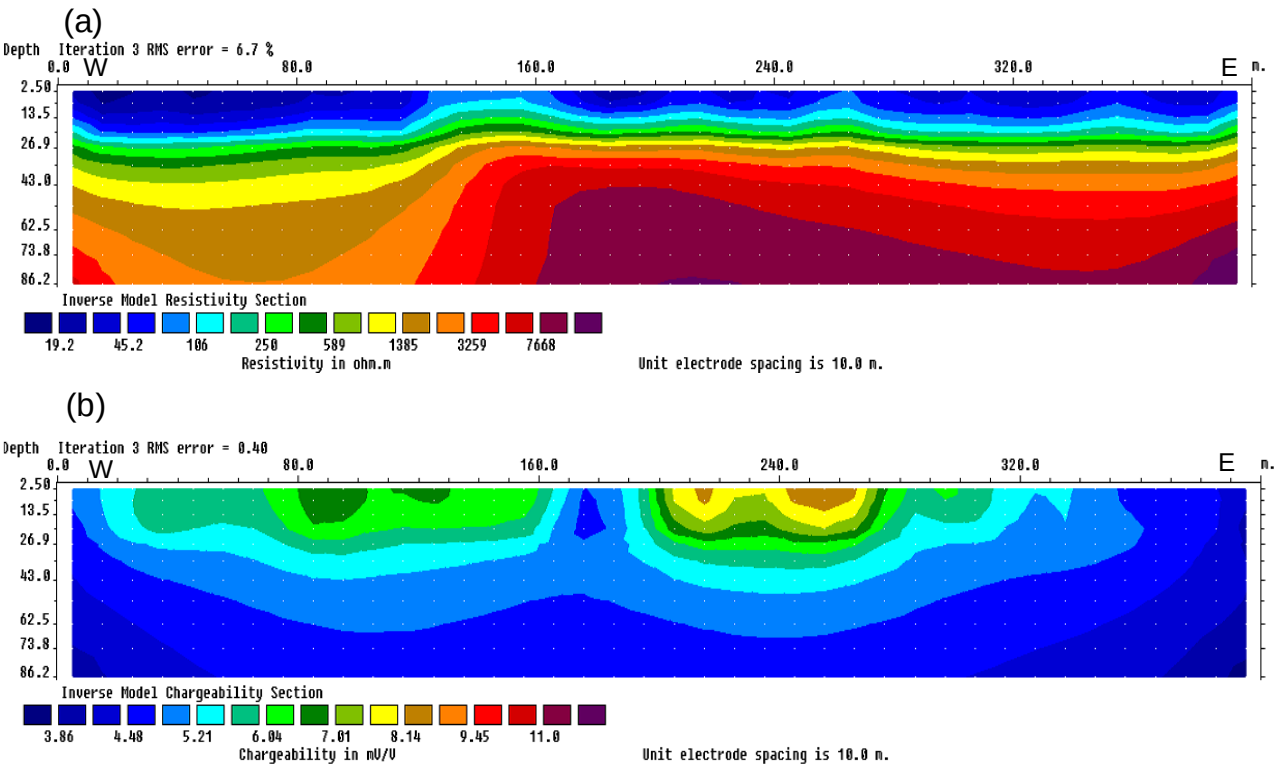

Figure 10. (a) 2D inverted resistivity model depicting homogeneous variation in lithology from west to east at Banagaon. **(b)** Chargeability model showing a high anomalous chargeability variation in the near surface layers up to 20 m depth. Below this depth, it shows homogeneous variation and low chargeability.

(iii) ***Banagaon***

The resistivity model depicts that the top 20 m is a highly weathered rock with a resistivity of <50 Ohm.m. The model resistivity varies from 10 to 18,000 Ohm.m (Figure 10a). This indicates that the basement rock at this site differs from the other sites and may consist of metabasalts as the basement. The resistivity model indicated a gradual variation in resistivity all along the profile (Figure 10a), which indicates stratified structure and homogenous lithological variation. This suggests that the basement rock at the deeper depths have high resistivity and low chargeability (Figure 10a, b). Nevertheless, chargeability model revealed two highly contrasting anomalies below 80 m and 240 m lateral distances and show chargeability values of 7- 8 mV/V and 8 – 9 mV/V respectively. These highly anomalous values of chargeability indicate the mineral deposit signature at shallow depths up to 20 m (Figure 10b).

(iv) Surangpani

The resistivity model clearly indicates the presence of an intrusive body or faulted structure from both sides around the center of the profile (Figure 11a). Fractures are mapped on both sides around the center of the profile (Figure 11a). Further, the chargeability model indicates gradual change in IP values (Figure 11b). Sharp resistivity changes are seen around the center of the resistivity profile while no significant change is noticed in IP model (Figure 11a, b). The basement rock with resistivity >4920 Ohm.m, possibly represents granodiorite rock at the deeper depths on either side of the faulted structure (Figure 11a).

MINERAL PROSPECT MAP (MPM)

The derived mineral prospect map can be divided into five classes based on the probability of the economic presence of mineral(s)/ ore deposits in the area. They are: (i) very low, (ii) low, (iii) moderate, (iv). high and (v) very high (Figure 12). Out of the total prospected 4864.285 sq. km area, 7.46 sq. km area is covered by a very high prospecting zone in terms of mineral deposits. In comparison, the other divisions having very low, low, moderate and high are respectively occupied by 4509.58, 166.55, 46.49 and 130.40 sq. km area. This would indicate that major area are occupied by very low and low classes of deposition. Mineral prospects are high near the significant fault zones and lineament structures due to the favourable tectonic setting for hydrothermal mineralization. The area has shown a few pockets of very high mineralisation due to favourable conditions, like country rocks, lithology of surrounding rocks, age of formation and tectonic setting, which plays a significant role in mineral deposition (**Figure 12**). Geochemical analysis of stream sediments also gives the physical presence of minerals.

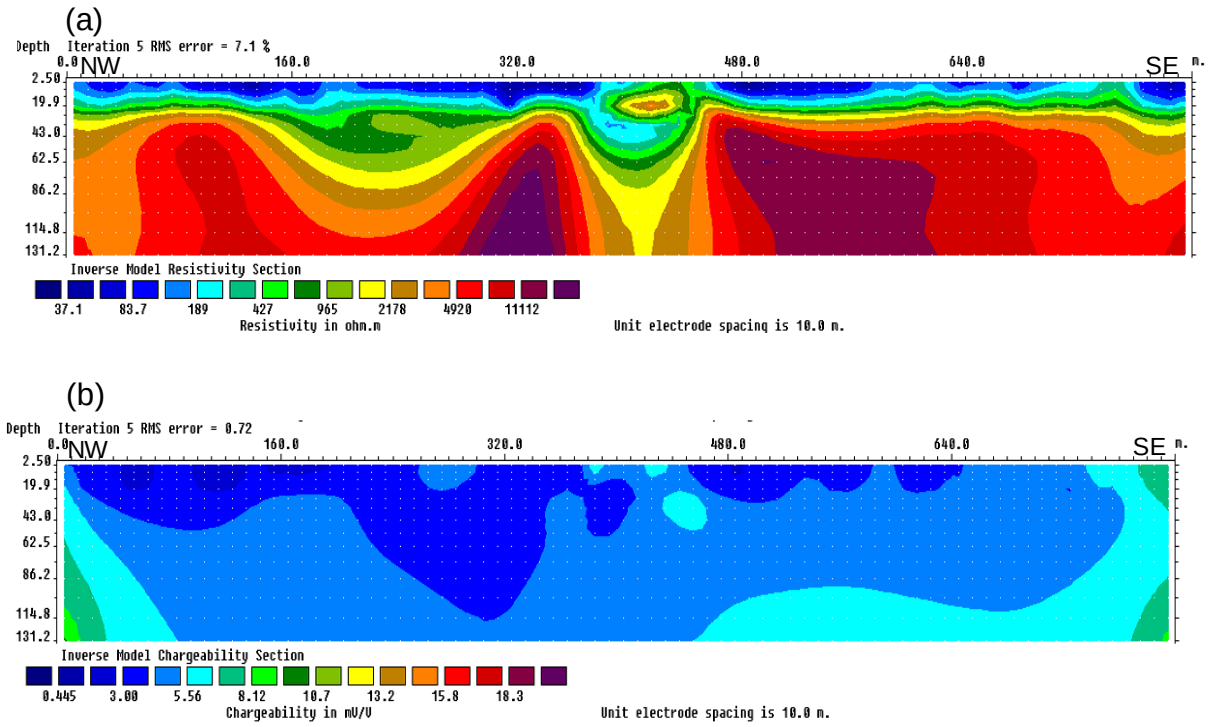

Figure 11. (a) 2D inverted resistivity model with a faulted structure on either sides around the center of profile thereby depicting two high resistivity bodies separated by a low resistivity zone at Surangpani. **(b)** Chargeability model showing gradual variation in chargeability all along the model.

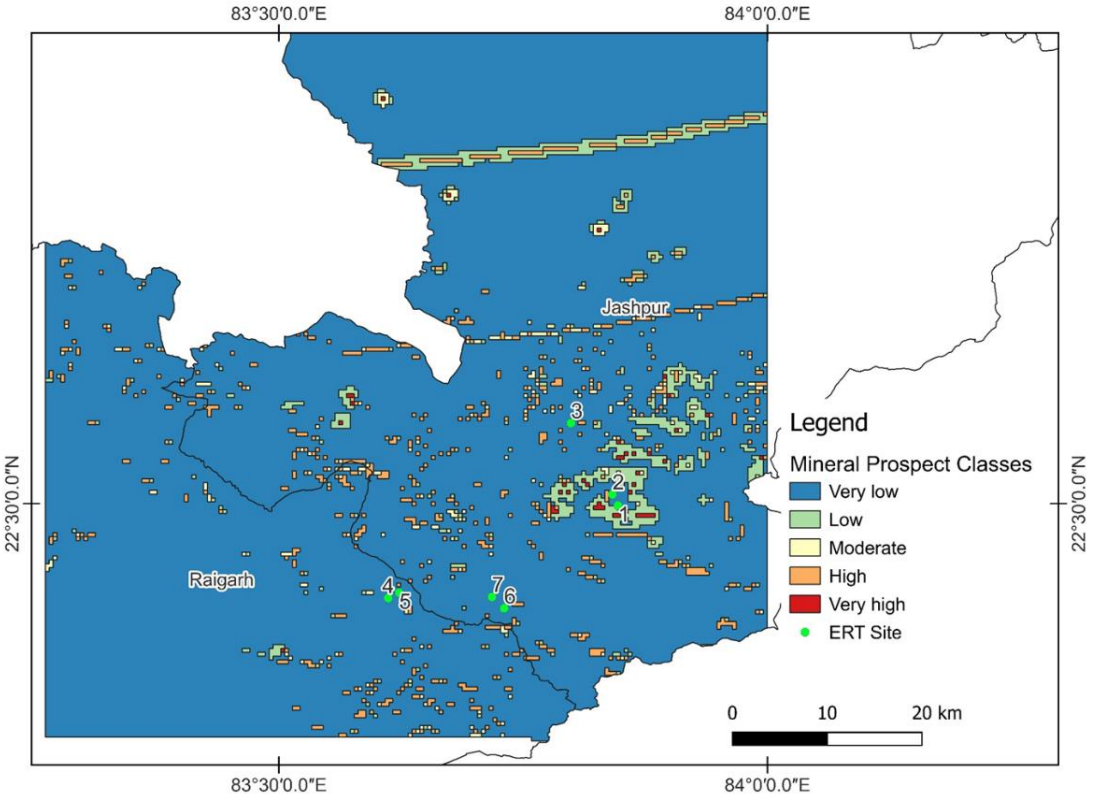

Figure 12. Derived mineral prospect map of the study area.

DISCUSSION

The study exemplify that the buffer of selective river networks indicates the high probability of the presence of source rock for pathfinder minerals within the buffered areas for mineralization. During the geological period, the source rocks get eroded and transported through the river networks. By tracing them back upstream, we get source rock and within this region also demarcated quartz dykes, which are primary suspects of our study contributing sediments to this river network. As a buffer of selective river networks and dykes intersects, those areas have high potential and the intrusive dykes can have high mineral potential. These results are validated from the resistivity and IP tomography model results that show significant variation both in resistivity and chargeability anomalies. The study area is classified as a limited zone for massive mineralization while in the disseminated form, high prospects for mineralization are mapped based on high resolution geophysics results along with the mineral prospect map. Further, it is suggested that only a few intrusive bodies contain gold minerals, including those with common intersections within the selective river buffers.

CONCLUSIONS

Distinct conducting anomalies are seen in the study area, which indicate the potentiality from low to very high concentration of mineral deposits in disseminated form. The chargeability varies from 0.44 to ~14 mV/V while the resistivity contrast ranges between ~10 to 25000 Ohm.m. The model results from chargeability, indicated disseminated sulphide mineral deposits within the host rock with varying mineral concentrations and metallic character. The resistivity tomography results clearly depicted the structural control for mineral deposits and illustrated the subsurface geological structures based on large resistivity contrasts. It is thus necessary to target faults, lineament and dykes for prospect gold exploration. Electrical resistivity tomography has the advantage to delineate both conductive and non-conductive subsurface geological formations within the study area, which is very crucial for knowing the mineralized zones. Nevertheless, integrating and correlating the results of resistivity and chargeability tomography models together, we achieved comprehensive understanding of the subsurface mineralization pockets at various locations and the anomalous zones signifying mineral deposition. On the other hand, the mineral prospect map has given an idea about the gold concentration based on geochemical and geophysical data analysis.

ACKNOWLEDGEMENTS

Authors are grateful to the Dr. Prakash Kumar Director, CSIR-National Geophysical Research Institute, Hyderabad, India, for

his kind permission and encouragement for publishing this research work. The 2nd author acknowledged Mr. Setbandhu Mondal and Mr. K. Rajesh research students for their untiring help during the electrical tomography data acquisition in the field areas. This work has been funded by CSIR through SHORE project number PSC0205 under the 12th five-year plan (FYP), which was completed successfully. The CSIR-NGRI library reference number of the manuscript is NGRI/Lib/2024/Pub-89. Authors thank the reviewers for their constructive comments, which improved the quality of the paper.

Author Credit Statement

Vishal Bajirao Nayakwdi carried out detailed geological study, prepared various maps and applied Analytic Hierarchy Process technique with the help of geophysical data. Dewashish Kumar acquired high resolution electrical resistivity tomography data, carried out modelling, integration and inversion of the geophysical dataset. Both the authors wrote the paper.

Data Availability

The various data used in the present work are available with us and can be provided upon reasonable request.

Compliance with ethical standards

The authors declare in the present research work there is no conflict of interest and adhere to copy right norms.

REFERENCES

ABEM, 2012. ABEM Instruction manual: Terrameter LS Toolbox, 31 pp.

Abijith, D., Saravanan, S., Singh, L., Jennifer, J. J., Saranya, T. and Parthasarathy, K. S. S., 2020. GIS-based multi-criteria analysis for identification of potential groundwater recharge zones—A case study from Ponnaniyaru watershed, Tamil Nadu, India. Hydro. Res., 3, 1–14. https://doi.org/10.1016/j.hydres.2020.02.002

Andualem, T. G. and Demeke, G. G., 2019. Groundwater potential assessment using GIS and remote sensing: A case study of Guna tana landscape, upper blue Nile Basin, Ethiopia. J. Hydrol: Regional Studies, 24, 100610. https://doi.org/10.1016/j.ejrh.2019.100610

Barnes, S.J., 2018. Chalcophile Elements. In: W. M. White (Ed.), Encyclopedia of Geochemistry, pp. 229–233. Springer Int. Publishing. https://doi.org/10.1007/978-3-319-39312-4_220

Bullock, L., Parnell, J., Perez, M., Feldmann, J. and Armstrong, J., 2017. Selenium and Other Trace Element Mobility in Waste Products and Weathered Sediments at Parys Mountain Copper Mine, Anglesey, UK. Minerals, 7(11), 229. https://doi.org/10.3390/min7110229

Cheng, Q., 1999. Spatial and scaling modelling for geochemical anomaly separation. J. Geochem., Expo., 65(3), 175–194.

Cheng, Q., Agterberg, F. P. and Ballantyne, S. B., 1994. The separation of geochemical anomalies from background by fractal methods. J. Geochem., Expo., 51(2), 109–130.

Choudhary, R. K., 1969. Geological mapping in parts of Raigarh district, MP progress report for the field season 1968-69. Submitted to Ministry of Mines.

Dora, M. L., 2014. PGE mineralization in Bastar Craton, central India: Prospects and constraints. Ind. J. Geosci., 68 (2- 3), 147–160.

Du, X., Zhou, K., Cui, Y., Wang, J., Zhang, N. and Sun, W., 2016. Application of fuzzy analytical hierarchy process (AHP) and prediction-area (P-A) plot for mineral prospectivity mapping: A case study from the Dananhu metallogenic belt, Xinjiang, NW China. Arab. J. Geosci., 9(4), 298. https://doi.org/10.1007/s12517-016-2316-y

Ge, Y., Liu, Z., Yu, Z., Wang, H., Lu, X., Zhang, L. and Xia, L., 2023. Distribution Behaviors of As, Sb, Bi, Sn, Se, Te, Au and Ag Between Cu and Liquid Metal Phases in the Cu-Pb Binary System at 500–1080°C. JOM, 75(5), 1515–1529. https://doi.org/10.1007/s11837-022-05633-1

Haldar, S. K., 2018. Mineral Exploration: Case Histories. In S. K. Haldar (Ed.), Mineral Exploration, Second Edition, pp. 313–352. Elsevier. https://doi.org/10.1016/B978-0-12-814022-2.00015-0

Ibrahim-Bathis, K. and Ahmed, S. A. ,2016. Geospatial technology for delineating groundwater potential zones in Doddahalla watershed of Chitradurga district, India. The Egyptian J. Rem. Sen. Sp. Sci., 19(2), 223–234.

Kalsotra, M. R. and Narang, J. L., 1983. Preliminary assessment of Gold occurrance in parts of Jashpur and Dharamjaygarh thesils, Raigarh district, Madhya Pradesh. Unpub. Rep. Geol. Surv. India.

Kumar, D., Satyanarayanan, M., Satish Kumar, K. and Sunder Raju, P.V., 2022. Electrical resistivity tomography of Mesoarchaean chromitite bands from Katpal in Sukinda Ultramafic Complex, Odisha. J. Earth. Sys. Sci., 131. https://doi.org/10.1007/s12040-021-01766-0

Kumar, D., Subba Rao, D.V., Mondal, S., Sridhar, K., Rajesh, K. and Satyanarayanan, M., 2017. Gold—Sulphide mineralization in ultramafic-mafic-granite complex of Jashpur, Bastar craton, central India: Evidences from geophysical studies. J. Geol. Soci. Ind., 90, 147–153.

Mansouri, E., Feizi, F., Rad, A. J. and Arian, M., 2017. A Comparative analysis of index overlay and TOPSIS (based on AHP weight) for iron skarn mineral prospectivity mapping, A case study in Sarvian area, Markazi Province, Iran. https://bulletin.mta.gov.tr/

Mishra, B. K., Hemraj, B., S. and Shreeramamurthy, A., 2008. Regional search for lamprolite/kimberlite in Tapti lineament zone in Raigarh, Jashpur and Surguja district of Chhattisgarh. Unpub. Rep. Geol. Surv. Ind., F.S. 1997 to 2000.

Pradhan, B., Jena, R., Talukdar, D., Mohanty, M., Sahu, B. K., Raul, A. K. and Abdul Maulud, K. N., 2022. A new method to evaluate gold mineralisation-potential mapping using deep learning and an explainable artificial intelligence (XAI) model. Remo. Sens., 14(18), 4486.

Rahmati, O., Nazari Samani, A., Mahdavi, M., Pourghasemi, H. R. and Zeinivand, H., 2015. Groundwater potential mapping at Kurdistan region of Iran using analytic

hierarchy process and GIS. Arab. J. Geosci., 8(9), 7059–7071.

Ramadhani Mussa, K., Mjemah, I. and Machunda, R., 2020. Open-Source Software Application for Hydrogeological Delineation of Potential Groundwater Recharge Zones in the Singida Semi-Arid, Fractured Aquifer, Central Tanzania. Hydrol., 7, 28. https://doi.org/10.3390/hydrology7020028

Saaty, T. L., 1977. A scaling method for priorities in hierarchical structures. J. Mathem. Psycho., 15(3), 234–281. https://doi.org/10.1016/0022-2496(77)90033-5

Zuo, R., Xiong, Y., Ziye Wang, Z., Wang, J. and Oliver P. Kreuzer, O.P., 2023. A New Generation of Artificial Intelligence Algorithms for Mineral Prospectivity Mapping. Nat. Reso. Res., 32 (5), https://doi.org/10.1007/s11053-023-10237-w

Received on: 11-12-2024; Revised on: 05-03-2025 ; Accepted on: 27-03-2025

J. Ind. Geophys. Union, 29(4) (2025), 248-259
https://doi.org/10.71122/JIGU.29(4)2025.0024

Temporal and spatial analysis of dissolved oxygen, sea surface temperature and sea surface salinity in northern Indian Ocean: Implication for environmental trends and variability

Siddharth Srivasatv, Vivek Kumar Pandey*,Yaduvendra Singh and Prabha Kushwaha
K. Banerjee Centre of Atmospheric and Ocean Studies, Institute of Interdisciplinary Studies, Nehru Science Centre, University of Allahabad, Prayagraj - 211002, India.
*Corresponding author:vivekbhuoa@gmail.com

ABSTRACT

The Indian Ocean, a vital part of the world's climate system, influences both local and global environmental trends. Dissolved Oxygen (DO), Sea Surface Temperature (SST) and Sea Surface Salinity (SSS) in the northern Indian Ocean, are three crucial oceanographic parameters that provide a comprehensive temporal and spatial analysis. The main goal is to examine environmental trends and variability in this region, shedding light on the potential impacts of anthropogenic activities and climate change. Using data from the Copernicus Marine Environment Monitoring Service, with resolution of 0.25°, spanning from 1998 to 2020, we aim to understand the physical and biogeochemical dynamics of the Arabian Sea and the Bay of Bengal. The analysis reveals significant temporal and regional patterns in DO, SST, and SSS across the Indian Ocean basin, including clear seasonal variations, temporal long-term trends, and notable annual cycles. Variations in DO concentrations underscore the vulnerability of marine life to hypoxic or anoxic conditions, which could negatively affect biodiversity. Our results and statistical analyses emphasize the critical importance of ongoing monitoring and research in the northern Indian Ocean to understand the environmental changes occurring in this region. This study provides valuable insight into the intricate interplay of environmental trends and variability through a detailed examination of the temporal and spatial dynamics of DO, SST and SSS in the Northern Indian Ocean. It highlights the urgent needs for proactive measures to mitigate the impacts of climate change and human activities on this essential marine environment.

INTRODUCTION

Over the past few decades, global warming has significantly impacted weather, climate, human society and the economy (IPCC, 2018). Understanding the dynamics of critical oceanic parameters in these regions is essential for grasping their complex interactions and ecological processes. SSS, SST and DO are fundamental parameters that greatly influence the physical and biological properties of these oceanic areas (Smith et al., 2020). Detailed long-term studies of dissolved oxygen concentrations in the ocean, reveal a steady decline over the 50 years (Bushinsky and Emerson, 2018; Schmidtko et al., 2019). Decreasing DO levels are particularly evident in coastal oceans, leading to the proliferation and expansion of 'dead zones'. The oxygen cycle is associated with changes in ecosystem dynamics, nutrient availability and ocean circulation by global climate models (Emerson and Bushinsky, 2014).The loss of DO can have far-reaching consequences, affecting pelagic and benthic fisheries, tourism, ocean nutrient cycling, and the oceanic production of N_2O, a potent greenhouse gas.

The ocean obtains DO primarily through air-sea gas exchange and photosynthesis. DO is a critical parameter for marine organisms, as it reflects the availability of oxygen in seawater and is essential for their respiration and metabolic processes. The Arabian Sea and the Bay of Bengal, exhibit significant temporal and spatial variations in dissolved oxygen due to several factors. Subsurface dissolved oxygen is advected via water mass distribution pathways and mixed into adjacent water masses. Other contributing factors include surface solubility (affected by warming), decreased ventilation (due to increased stratification), and enhanced deep ocean respiration (driven by higher surface primary production and increased particle flux), all of which can result in de-oxygenation(Diaz and Rosenberg, 2008; Keeling et al., 2010; Peña et al., 2010). Physical, chemical and biological variables also play a crucial role in the dynamics of DO (Menzel and Spaeth, 1962). These include ocean currents, temperature, salinity, nutrient availability and biological productivity. Large-scale variability in seasonal average atmospheric inputs is reflected in the temporal and spatial variability of sea surface temperature, sea surface salinity and dissolved oxygen. Lower sea-surface oxygen concentrations, reduced mid-water ventilation due to ocean warming, and local eutrophication episodes, contribute to the expansion of marine dead zones (Stramma et al.,2008; Diaz and Rosenberg,2008).

Sea Surface Temperature (SST) refers to the temperature of the ocean's uppermost layer, while Sea Surface Salinity (SSS) denotes the concentration of dissolved salts in the same layer. Both SST and SSS are fundamental oceanographic indices critical for understanding the physical and chemical properties of the ocean and their influence climate and ecosystems (Schmidt et al., 2019). SST variability is a multidimensional phenomenon driven by various natural and anthropogenic factors. SST oscillations are influenced by solar radiation, air-sea heat exchanges, monsoonal circulation patterns, oceanic forcing mechanisms and human activities (Smith et al., 2020). These intricate interactions of mechanisms, underscore the need for comprehensive research into the complex dynamics of SST and its implications for climate and ecosystems. SSS concentration is regulated by multiple factors, including river freshwater discharge, precipitation, evaporation, climate variability, and oceanic currents (Rao and Sivakumar, 2003).

The annual SST fluctuation in the Arabian Sea(AS) and the Bay of Bengal (BoB), is bi-modal (Colborn et al., 1975), with surface warming occurring in April-May and October, and surface cooling observed during the SW monsoon and winter months. However, the Arabian Sea experiences faster cooling during the SW monsoon. Previous studies highlight the significance of Arabian Sea. SST is significant due to its potential influence on the inter-annual variability of the Indian summer monsoon (Li et al., 2001; Vinayachandran,2004; Wilson-Diaz et al., 2009).

During the south-west monsoon, winds are stronger over the Arabian Sea than over the Bay of Bengal due to the presence of the Findlater Jet (Shenoi et al., 2002). These stronger winds enhance evaporation, upwelling, and the spread of coastal cold waters along the shores of Arabia and Somalia, resulting in a broad distribution of cooler SST water into the central Arabian Sea. SST also influence monsoon onset (Vinayachandran2004) and biological productivity (Murtugudde et al., 2007) in the Arabian Sea. In both the Arabian Sea and Bay of Bengal, surface heat fluxes predominantly drive monthly SST variation, except the upwelling zone along the western boundary of the Arabian Sea(Chowdary et al., 2014;Du et al., 2019). SST fluctuation is further influenced by salinity effects and subsurface processes such as barrier layers, vertical entrainment, in solar radiation penetration depth, and zonal advection (Thangaprakashet al., 2016). Monsoon driven variability in rainfall significantly impacts near-surface salinity variations, especially in the Bay of Bengal which exhibits a pronounced annual cycle of sea surface salinity (Akhil et al., 2014). Freshwater influx at the bay's northern end forms a shallow, stratified mixed layer with low salinity which is advected southwards along India's east coast being diminished by vertical mixing (Akhil et al., 2014). This variability in freshwater input also contributes to the seasonal cycle of barrier layer thickness in the Bay of Bengal (Jana et al., 2015). Sea surface salinity has been widely used to describe oceanic phenomena such as ocean circulation, sea-level changes, instability waves, and Rossby waves. Changes in seawater density, caused by colder and saltier water, can lead to sinking to greater depth sustaining global ocean circulation.The Indian monsoon drives strong mixing and high productivity in the Arabian Sea, while in the Bay of Bengal, heavy rainfall and stratification limit mixing, but enhance atmospheric convection (Shenoi et al., 2002).

Understanding the interaction of DO, SSTand SSS in these regions, is crucial for a comprehensive description of their marine environments. These parameters play an essential role in shaping the physical, chemical, and biological aspects of ecosystem dynamics, hypoxia and anoxia, climate change and ocean-atmosphere interactions.These parameters are interconnected, influencing one another and driving the physical and biogeochemical processes that define marine ecosystems and climate dynamics. This study synthesizes relevant literature and research findings to provide a comprehensive understanding of the variability and interdependencies of SSS, SST and DO in the Arabian Sea and Bay of Bengal. It highlights their ecological implications and contributes to a holistic assessment of these vital oceanic regions. DO dynamics are particularly significant in the Arabian Sea and Bay of Bengal. A multidisciplinary approach involving field measurements, remote sensing and modeling techniques, has been employed to uncover the driving mechanisms and ecological impacts of DO variability. Similarly, SST or SSS are critical drivers of weather patterns, ocean currents, and marine ecosystems in these regions. Research on SST and SSS variations leverages satellite observations, in-situ measurements, and numerical models to unravel there complex patterns and underlying mechanisms, and temporal and spatial dynamics. By exploring the interdependencies of these parameters and their implications for the marine environment, this study provides valuable insights into the ecological and climatic processes shaping the Arabian Sea and Bay of Bengal.

STUDY AREA

The study area in the Arabian Sea and the Bay of Bengal (Figure 1), provides a unique opportunity to investigate the inter-connectedness of physical and bio-geochemical processes and their impact on marine ecosystems. Through this study, we aim to enhance the broader understanding of complex oceanic dynamics, and ecological responses and the factors influencing the health and sustainability of marine environments. To facilitate a better understanding of variability, the study area is divided into specific regions, northern Arabian Sea , western Arabian Sea, eastern Arabian Sea, central Arabian Sea, northern Bay of Bengal, western Bay of Bengal, eastern Bay of Bengal and central Bay of Bengal.

DATA AND METHODOLOGY

Data

Copernicus Marine Environment Monitoring Service (http://marine.copernicus.eu/), utilizing a horizontal resolution of 0.25^{o}, provided the data for this study. The analysis employed the Global ocean analysisv3.6 NEMO (Nucleus for European Modeling of the Ocean), integrated with the PISCES (Pelagic Interaction Scheme for Carbon and Ecosystem Studies) biogeochemical model, using atmospheric forcing from European Centre for Medium-Range Weather Forecasts (ECMWF). Data spanning from 1998 to 2020 was used to understand the physical and biogeochemistry of the Arabian Sea and Bay of Bengal.

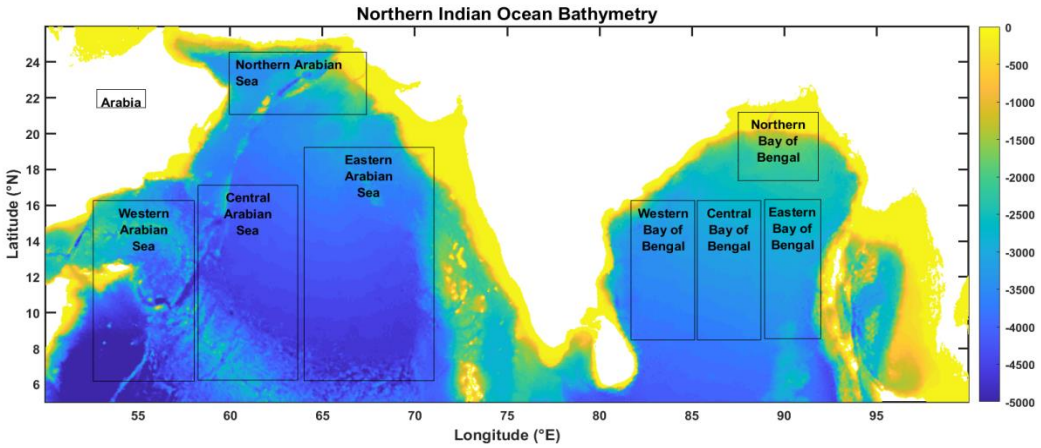

Figure 1. Different studied regions of the Northern Indian ocean

Methodology

In the present study, line graphs were used to illustrate the time series distribution of vital biogeochemical variables over the study period in the Arabian Sea and Bay of Bengal. This visual representation enables the observation of temporal patterns and trends, providing valuable insights into the variability of these variables. To explore the relationships between these variables, Pearson's correlation test was conducted and statistical analysis assessed the strength and direction of the relationships among the biogeochemical variables. By quantifying the magnitude of these correlations, the study deepened our understanding of how the variables influence each other within the study area. Additionally, multiple linear regression models were developed separately for the Arabian Sea and Bay of Bengal, with DO concentration as the dependent variable. The analysis considered other biogeochemical variables as independent predictor to identify significant drivers of DO concentration. This approach revealed the critical factors influencing DO levels in the region and provided insights into the relative importance of different variables in shaping its distribution. Ultimately, this research enhanced our understanding of the factor affecting DO concentration in the Arabian Sea and Bay of Bengal. By identifying significant predictors and quantifying their impacts, it contributes to the broader understanding of biogeochemical processes and the dynamics of these vital oceanic regions.

Descriptive Statistics

Descriptive statistics were employed to summarize the biogeochemical data.

Mean (μ)

The arithmetic average of the dataset, calculated as:

$$\mu = \frac{\sum x_i}{n}$$

where x_i represents individual data points, and n is the total number of observations.

Standard Deviation (σ)

A measure of data dispersion around the mean, computed as:

$$\sigma = \sqrt{\frac{\sum_{i=1}^{n}(x_i - \mu)^2}{n}}$$

Pearson Correlation Coefficient (r)

This correlation coefficient between two variables (X and Y) is given as:

$$r = \frac{\Sigma_{i=1}^{n}(x - \bar{x})(y_i - \bar{y})}{\sqrt{\Sigma_{i=1}^{n}(x_i - \bar{x})^2 \sum_{i=1}^{n}(y - \bar{y})^2}}$$

where, x_i and y_i represent the individual data points for variables X and Y, while $\bar{x}$ and $\bar{y}$ are their respective means.

Regression Analysis

To identify significant predictors of dissolved oxygen (DO) concentration, multiple linear regression models were developed for both the Arabian Sea and Bay of Bengal. The dependent variable in these models was DO concentration**,** while independent variables included the other biogeochemical parameters. The following model summary statistics were used to evaluate model performance:

Model Summary Statistics

$$R^2 = \frac{\text{Explained variance}}{\text{Total variance}}$$

Adjusted R^2, corrects R^2 for the number of predictors in the model which can be given as,

$$\text{Adjusted } R^2 = 1 - \frac{(1 - R^2)(n-1)}{n-k-1}$$

Where$n$is the number of observations, k is the number of predictors, R is the correlation between observed and predicted values of the dependent variable.

Standard error of the estimate (SE) measures the accuracy of predictions and can be written as a

$$SE = \sqrt{\frac{\sum_{i=1}^{n} (Y_i - \hat{Y})^2}{n-k-1}}$$

where Y_i is the observed value, and $\hat{Y}$ is the predicted value.

Change Statistics

R^2 Change: The increment in R^2 due to additional predictors.

F Change: The F-statistic for the change in R^2, and can be calculated as,

$$\text{F change} = \frac{(R^2\text{new} - R^2\text{old})/m}{(1 - R^2\text{new})/(n-k-1)}$$

where m is the number of new predictors added.

RESULTS

Seasonal variability of dissolved oxygen, sea surface temperature and sea surface salinity

During the pre-monsoon season (Figure 2) in the northern Arabian Sea, DO levels range from 200-210mmol/m^3, SST 24.5-25ºC and SSS, 37-37.5PSU.These comparatively high values indicate that northern Arabian Sea waters have adequate oxygen levels, which are crucial for marine organisms that are reliant on dissolved oxygen for respiration. This temperature range is conducive to normal ocean circulation and weather patterns, and supports many marine species. The salinity levels suggest moderately saline waters, which influence ocean currents, density and the distribution of marine species. It also suggest, moderately saline waters, which influence ocean currents, density, and the distribution of marine species, as some are adapted to specific salinity conditions. In the western Arabian Sea region, the DO ranges from 200-210 mmol/m^3, SST 28-28.5ºC, and SSS 36-36.5PSU. Similarly, in the eastern Arabian Sea, DO concentrations are slightly lower at around 198-200 mmol/m^3, with SST increasing from 27ºC in the north to28.5ºC in the south, and SSS decreasing southward from 34.5 PSU. In the central Arabian Sea, DO ranges from 190-200 mmol/m^3,with a declining trend from north to south.SST varies between 26.5-29ºC,increasing southward,while SSS decreases from37 PSU in the north to 35.5 PSU in the south. In the northern Bay of Bengal, DO concentration is highest near the Ganges-Brahmaputra river mouth, at 260 mmol/m^3 and decreasing southward. SST near the river mouth is 25.5ºC, with regional variations ranging from 25.5-26.5ºC north to south. SSS in the northern Bay of Bengal is relatively low at 32 PSU during pre-monsoon season, reflecting the influence of freshwater input. In the western Bay of Bengal, DO ranges from 210-220 mmol/m^3, with a decreasing trend from north to south. SST ranges from 27.5ºC in the north to 29ºC in the south, while SSS varies from 32 PSU in the north to 33.5PSU in the south.

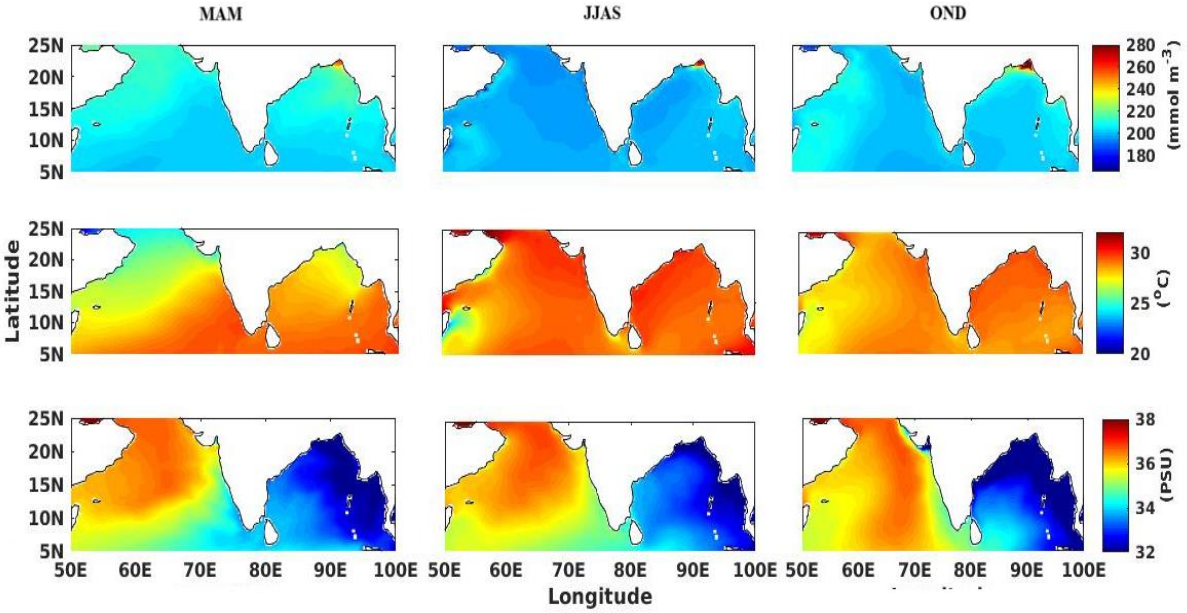

Figure 2. Seasonal mean climatology of dissolved oxygen, sea surface salinity, and sea surface temperature over the Arabian Sea and Bay of Bengal.

In the eastern Bay of Bengal, DO concentration ranges from 200-215 mmol/m^3, slightly higher than those observed in the western Bay of Bengal and central Bay of Bengal. SST varies between 26.5-27ºC in the northern segment of the eastern Bay of Bengal with a slight increase toward the south. SSS remains steady at 32 PSU in this region. In the central Bay of Bengal, DO concentration show a declining trend, ranging from 205 mmol/m^3 in the north to 196 mmol/m^3 in the south. SST increases from 27.7ºC in the northern region to 29ºC in the southern region, while SSS is 32 PSU in the north, slightly increasing to 33.5 PSU in the southern central Bay of Bengal. During the monsoon season, the DO concentrations decline in the northern Arabian Sea to 190-195 mmol/m^3. SST rises to 30ºC, and SSS remains at 37 PSU. In the western Arabian Sea, DO levels are slightly higher, ranging from 200-210 mmol/m^3, with values near the Arabian coast reaching 210 mmol/m^3. This elevated DO spreads from the Arabian coast to the Socotra region. SST increases to (27.5ºC), although lower temperatures are recorded near the Arabian coast (26.5ºC) and in the Socotra region (26ºC). SSS in the western Arabian Sea varies from 36 PSU in the north to 37 PSU in the south, showing a decreasing trend from north to south. In the eastern Arabian Sea, DO levels vary from 190-200 mmol/m^3, with a decreasing trend from north to south. SST ranges from 25.5ºC - 29ºC, with the Arabian coast experiencing temperatures of 26.5ºC and the Socotra region 25.5ºC. SSS varies from 35.5 PSU near the coast to 36 PSU farther offshore, increasing toward the central Arabian sea. Salinity generally decreases from north to south in the eastern Arabian sea region. In the central Arabian Sea, DO levels range from 190 to 200 mmol/m^3, with a slight increase observed southward. SST during the monsoon season ranges from 29.5ºC in the north to 30ºC in the south. SSS starts at 37 PSU in the northern central Arabian Sea and decreases southward to 35.5 PSU.

During the pre-monsoon season of the northern Arabian Sea, the DO is 200-210 mmol/m^3, the SST is 24.5 - 25ºC and SSS in the range of 37 - 37.5 PSU. In the western Arabian Sea region, the DO is 200-210 mmol/m^3, SST is 28-28.5ºC, and the SSS value is 36-36.5 PSU. In the eastern Arabian Sea, DO concentration is 198-200 mmol/m^3, The SST varies from 27-28.5ºC, showing a gradual increase from the northern to southern segment of the eastern Arabian Sea. The SSS decreases southward, starting at 34.5 PSU in the northern region. In the central Arabian Sea, the DO is 190-200 mmol/m^3.There is a decreasing trend in DO from north to south in the central Arabian Sea region. SST ranges from 26.5-29ºC, showing an increase from north to the south. The SSS in the central Arabian Sea region varies from 35.5-37 PSU, decreasing gradually from north to south. In the northern Bay of Bengal, dissolved oxygen is highest near the Ganges-Brahmaputra river mouth (260 mmol/m³), decreasing southward (230–260 mmol/m³). Sea surface temperature (SST) ranges from 25.5°C near the river mouth to 26.5°C in the south, while sea surface salinity (SSS) is 32 PSU during pre-monsoon. In the western Bay of Bengal, DO ranges from 210–220 mmol/m³, also decreasing southward. SST in the western Bay of Bengal varies from 27.5ºC-29ºC.The SST is 27.5ºC in the northern region and increases to 29ºC in southern segment of western Bay of Bengal. The SSS in north-western Bay of Bengal is 32 PSU increasing to 33.5 PSU in southern segment of western Bay of Bengal region. The DO concentration in eastern Bay of Bengal region is 200-215 mmol/m^3, slightly higher than in western Bay of Bengal and central Bay of Bengal. SST in the eastern Bay of Bengal ranges from 26.5-27ºC. The northern segment of the eastern Bay of Bengal has a lower SST, which slightly increases toward the south. The SSS is 32 PSU in eastern Bay of Bengal. In the central Bay of Bengal, it is 205 mmol/m^3 in the northern region, showing a decreasing trend toward the south, where it drops to 196 mmol/m^3. The SST in the northern central Bay of Bengal is 27.7ºC and increases to 29ºC toward the south. The SSS starts at 32 PSU in the northern region and increases slightly toward the southern region, reaching 33.5 PSU.

During the monsoon season, the DO declines to190-195 mmol/m^3 in the northern Arabian Sea region. The temperature in the northern Arabian Sea is 30ºC, and the SSS is 37 PSU. In the western region of the Arabian Sea, DO is slightly more than northern Arabian Sea 200-210 mmol/m^3 and 210 mmol/m^3 reported near the Arabian coast. This increase in DO extends from the Arabian coast to the Socotra region. SST increases to 27.5ºC, but low temperature is found near the Arabian coast, where SST is 26.5ºC, and in the Socotra region, where it is 26ºC. SSS varies from 36 PSU to 37 PSU, showing a decreasing trend from north to south in the western Arabian Sea region. The DO in the eastern Arabian Sea varies from 190-200 mmol/m^3, with a decreasing trend observed from north-to-south in the eastern Arabian Sea region. SST ranges from 25.5ºC to 29ºC during monsoon season. Near the Arabian coast, the SST is 26.5ºC and in the Socotra region, it is 25.5ºC. SSS ranges from 35.5 PSU to 36 PSU, with lower salinity observed near the coast areas of eastern Arabian Sea. Salinity increases toward the central Arabian Sea region within eastern Arabian Sea. In the central Arabian Sea region, DO ranges from 190 to 200 mmol/m^3, with a slight increase in concentration observed from north to south. SST during the monsoon season varies from 29.5ºC to 30ºC. SSS in the northern central Arabian Sea 37 PSU, which decreases southward, reaches 35.5 PSU. In the monsoon season, the northern Bay of Bengal near the Ganges-Brahmputra river mouth has a DO of 280 mmol/m^3, which decreases as it moves away from the northern coastal region. SST in the northern region is above 27.5-28ºC, and SSS is 32 PSU. In the western Bay of Bengal region, the DO near the coastal area is

195 mmol/m^3, decreasing toward the central and eastern directions, reaching 190 mmol/m^3. SST is about 29ºC near the western Bay of Bengal coastal region, showing a prolonged decreasing trend toward the central and southern western Bay of Bengal region, reaching 33.5 PSU. In the eastern Bay of Bengal region, DO is 198 mmol/m^3. With only a slight variation during the monsoon season. SST is around 29ºC, showing only slight variation southward in the eastern Bay of Bengal. SSS in the eastern Bay of Bengal is 32 PSU during the monsoon season. In the central Bay of Bengal region, the DO is 196 mmol/m^3, with a slight increase to 196.8 mmol/m^3 from southern to the northern segment central Bay of Bengal. SST is 28ºC, decreasing to 27.8ºC toward the southern region of the central Bay of Bengal. SSS in the northern Bay of Bengal is 33.1 PSU, decreasing to 32 PSU toward the south, then increasing again in the same direction.

In the post-monsoon season, the DO in the northern Arabian Sea region is 200 mmol/m^3. In the western region northern Arabian Sea region, the DO concentration is higher compared to the eastern part of the northern Arabian Sea region. SST in the northern Arabian Sea is 27 – 27.5ºC, and SSS is 37 PSU during the post-monsoon season. In the western Arabian Sea, the DO is 210 mmol/m^3, slight decrease to 207 mmol/m^{3}in the mid-western Arabian Sea. The SST near the coast of the western Arabian Sea is 26.5ºC, and the DO increases to 21 mmol/m^{3}in the southern western Arabian Sea. Salinity in the western Arabian Sea region from 35.7 - 35.5 PSU with slight variations. The northern western Arabian Sea exhibits elevated salinity (+0.2 PSU) compared to southern freshening (−0.1 to −0.3 PSU), driven by evaporation-precipitation and riverine contrasts. In the eastern Arabian Sea, DO ranges from 192-197 mmol/m^3. The DO concentration increases southward along coastal region. SST in eastern Arabian Sea is 27.5ºC, with slight decrease in the SST observed in the coastal and central regions of the eastern Arabian Sea. The SSS in the eastern Arabian Sea varies from 32.2-36PSU, with the lowest salinity (32 PSU) found near the Gulf of Khambhat. It slightly increases to 34 PSU toward the southern eastern Arabian Sea and reaches 36 PSU in the central-eastern Arabian Sea. In the central Arabian Sea, the DO is 200 mmol/m^3, which is lower than the eastern Arabian Sea region. A slight increase in DO is observed from east to west, while it decreases from north to south in the central Arabian Sea region. SST in the central Arabian Sea region varies from 27-29ºC, with lower SST in the northern central Arabian Sea and decreases toward the southern central Arabian Sea. The SSS is 37 PSU and decreases toward the western Arabian Sea region. In the northern Bay of Bengal, highest DO concentration is 280 mmol/m^3, present in the broad northern region near the Ganges-Brahmaputra river mouth. This high DO concentration gradually decreases toward the central open region of the Bay of Bengal. SST in northern Bay of Bengal is slower than during monsoon season, ranging from 27-28ºC, and it declines toward the central Bay of Bengal. The SSS in the northern Bay of Bengal is very low, at 32 PSU, and slightly increases toward the central Bay of Bengal.

Annual variability of dissolved oxygen, sea surface temperature and sea surface salinity

During the pre-monsoon season (Figure 3), DO levels in the Arabian Sea decline from 206 mmol/m^3 to 197 mmol/m^3. Simultaneously, SST increases from 26°C at the onset of pre-monsoon to 29.7°C in mid-pre-monsoon, followed by a further rise during the transition from pre-monsoon to monsoon. Throughout the monsoon season, DO levels rise from 197 mmol/m^3 to 204 mmol/m^3, while sea surface salinity experiences an initially increase but shows a slight decline from July onwards. Meanwhile, SST decreases consistently from 29.8°C to 27.5°C during the monsoon period. In the post-monsoon season, DO levels in the Arabian Sea remain relatively stable, showing a slight increase from 197 mmol/m^{3}to 204 mmol/m^3. Sea surface salinity exhibits a marginal increase initially, followed by a gradual decline. Concurrently, Sea surface temperature decreases steadily from 29.8°C to 27.5°C throughout the post-monsoon period.

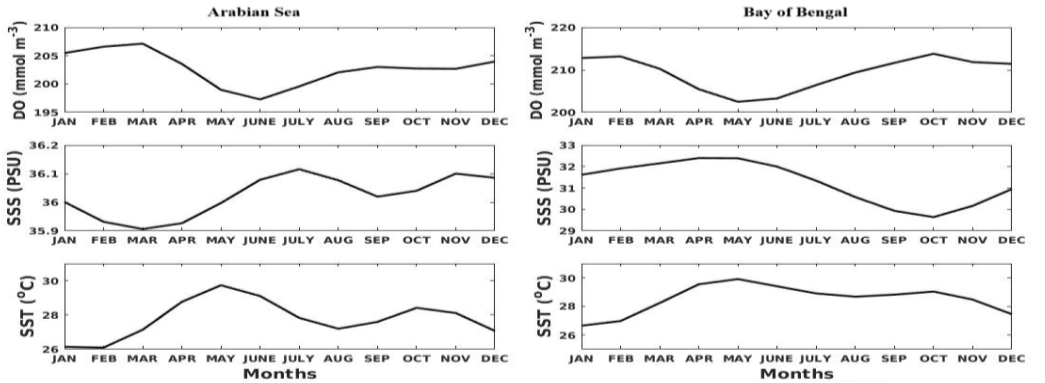

Figure 3. Annual cycle of the dissolved oxygen (mmol/m^3), sea surface salinity(PSU) and sea surface temperature(˚C) over the Arabian Sea and Bay of Bengal.

In Contrast to the Arabian Sea region, the Bay of Bengal displays different trends in dissolved oxygen, sea surface salinity, and sea surface temperature. During the pre-monsoon season, dissolved oxygen levels decline rapidly from 214 mmol/m^3 to 204 mmol/m^3, while sea surface salinity and sea surface temperature increases from 0.5 PSU to 27.8°C and 28.8°C, respectively. Throughout the monsoon season, dissolved oxygen levels steadily raise from 203 mmol/m^3 to 214 mmol/m^3, In contrast, sea surface salinity decreases from 32.1 PSU to 29.9 PSU and sea surface temperature shows an initial slight decline followed by an increase towards the end of the monsoon period. In the post-monsoon season in the Bay of Bengal region, DO levels experience a slight decrease from 215 - 213 mmol/m^3 initially, stabilizing toward the end of the season. Conversely, sea surface salinity exhibits an increasing trend from 29.8 PSU to 31 PSU, while sea surface temperature decreases from 29°C to 27.5°C.

Inter-annual trend of dissolved oxygen, sea surface temperature and sea surface salinity

A decreasing trend in the concentration of dissolved oxygen in the Arabian Sea is observed (Figure 4). The plot indicates a yearly decrease in DO concentration of 0.0061 mmol/m^3, alongside an increase in sea surface temperature is 0.0017 and an increase in sea surface salinity to 0.00026 PSU. During the study period, the concentration of dissolved oxygen varied from 195.5 to 209 mmol/m^3, sea surface salinity ranged from 35.8 to 36.3 PSU, and sea surface temperature fluctuated between 25.4 and 30.1ºC.

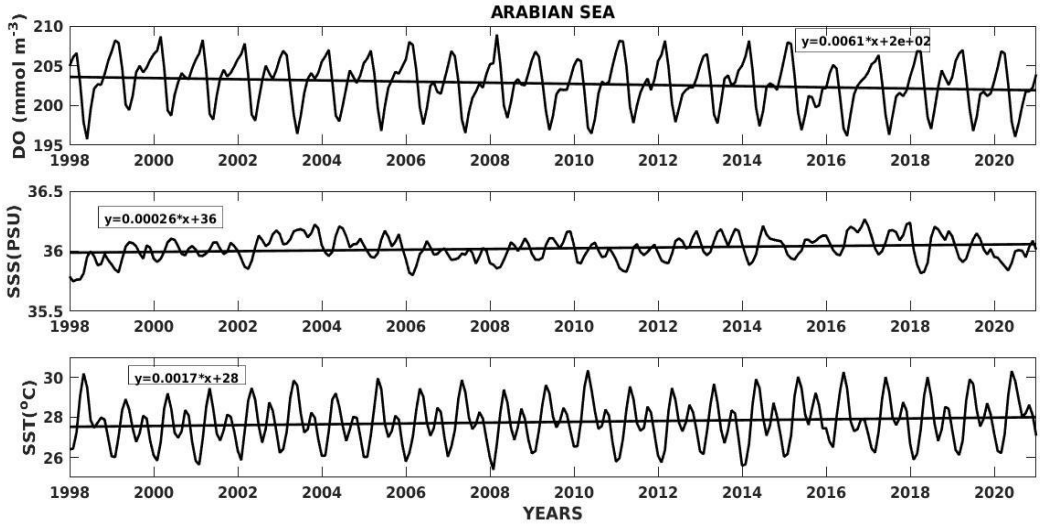

Figure 4. Temporal trend of DO (mmol/m^3), SSS (PSU) and SST (˚C) from 1998 to 2020 in the Arabian Sea.

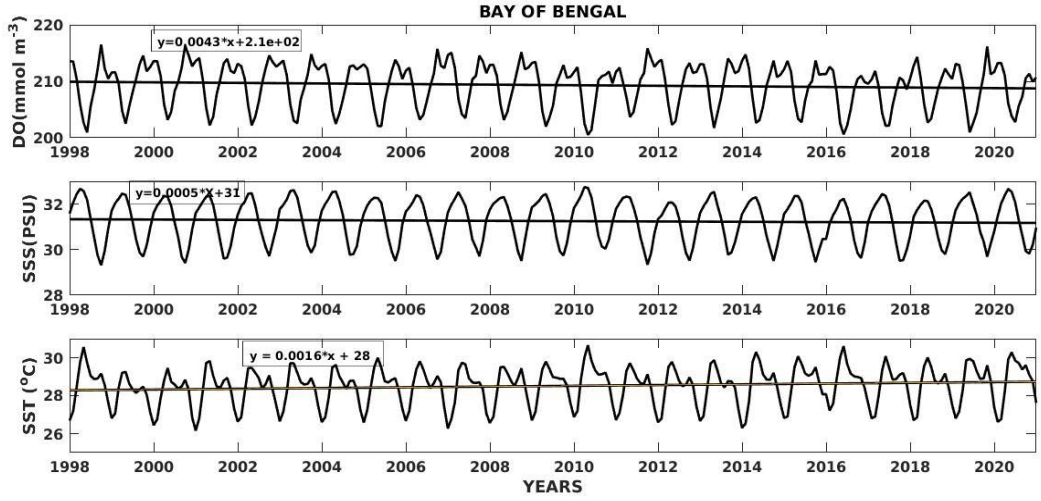

Figure 5. Temporal trend of DO (mmol/m^3), SSS (PSU) and SST (˚C) from 1998 to 2020 in Bay of Bengal region.

A decreasing trend in the concentration of dissolved oxygen in the Bay of Bengal is also observed (Figure 5). The plot indicates a yearly decrease in dissolved oxygen concentration of 0.0043 mmol/m^3, an increase in sea surface temperature is 0.0016ºC, and a decrease in sea surface salinity of 0.00059 PSU. During the study period, the concentration of DO varied from 200.5 to 216 mmol/m^3, sea surface salinity ranged from 29.5 to 32.8 PSU, and sea surface temperature fluctuated between 26.4 and 30.5ºC.

Anomaly of dissolved oxygen, sea surface temperature and sea surface salinity The dissolve oxygen anomaly (Figure 6) shows both increasing and decreasing trends, with dissolve oxygen and sea surface salinity exhibiting an increasing trend or vice versa. Sea surface salinity is influenced by global warming, IOD (Indian Ocean Dipole), monsoon and ENSO (El Niño-Southern Oscillation),while precipitation, cold currents or the winter season negatively impact Sea surface salinity. Cold current increase SSS or dissolve oxygen due to presence of high nutrient levels and a positive anomaly in dissolve oxygen, sea surface salinity and SST reflects an increase in dissolve oxygen, sea surface salinity concentration, and temperature. The line plot of the Arabian Sea anomaly indicates difference between actual dissolve oxygen, sea surface salinity, SST and the long-term average. An increase in the anomaly of dissolve oxygen may suggest the water is becoming more eutrophic or nutrient-rich, leading to increased primary productivity, decreased decomposition, mixing of water layers, reduced water temperature, improved and support of aquatic life growth. Similarly, an increase in the sea surface salinity anomaly indicates changes such as increased evaporation, decreased precipitation, or altered ocean currents, potentially harming marine life, altering food webs, and reducing water quality. An increase in the SST anomaly reflects influences from phenomenon like El Niño-Southern Oscillation (ENSO), increased stratification, and changes in ocean currents, alongside climate-related impacts, such as rising sea levels, ocean acidification, and shifts in precipitation patterns.

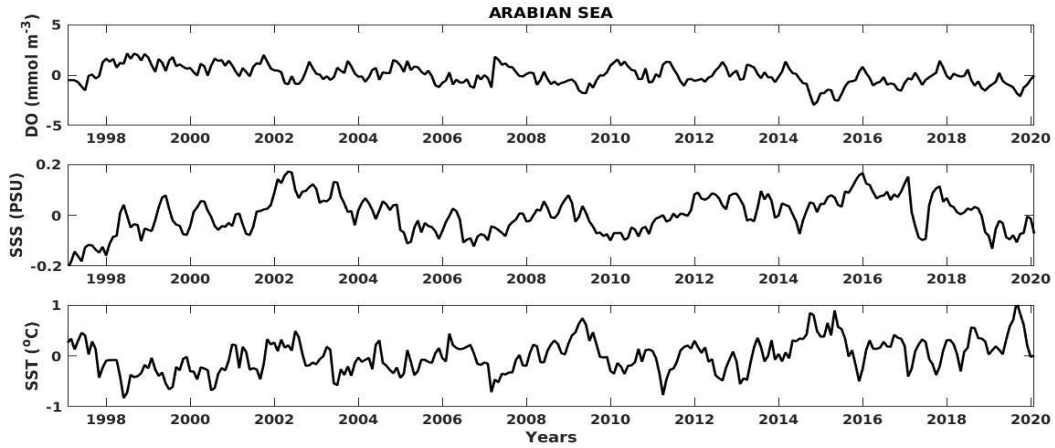

Figure 6. Anomaly of the dissolved oxygen (mmol/m^3), sea surface salinity (PSU) and sea surface temperature (˚C) from 1998 to 2020 in Arabian Sea.

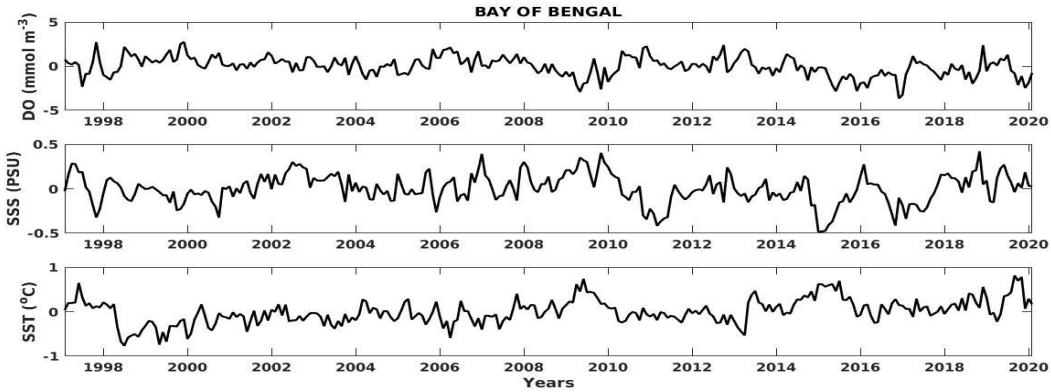

Figure 7. Anomaly of the dissolved oxygen (mmol/m^3), sea surface salinity(PSU) and sea surface temperature(˚C) from 1998 to 2020 in the Bay of Bengal region.

The line plot (Figure 7) illustrates anomalies in the Bay of Bengal (BoB), representing deviations from the long-term average in DO, sea surface salinity, and SST. These anomalies carry significant implications for the marine ecosystem. Specifically, we observe notable increases in DO anomalies during various periods. Such elevated DO anomalies may indicate a shift toward eutrophic conditions, characterized by increased nutrient enrichment. These conditions tend to enhance primary productivity, reduce decomposition rates, promote vertical mixing of water layers, and lower water temperatures, thereby improving overall water quality and supporting aquatic life. Additionally, the anomalies in sea surface salinity suggest changes in ocean conditions. These anomalies align with increased evaporation, decreased precipitation, and alterations in ocean currents, which may harm marine life and disrupt the marine food web. Such changes can ultimately lead to reduced water quality. In this case, SST anomalies variations may be linked to climatic phenomena such as the El Niño-Southern Oscillation (ENSO) and monsoonal influences. For instance, significant rainfall during the summer monsoon reduces salinity levels in the Bay of Bengal, while lower rainfall during the winter monsoon results increased salinity. These fluctuations can lead to stratification, shifts in ocean currents, and broader climate-related impacts, including rising sea levels, ocean acidification, and changes in precipitation patterns.

Statistics of dissolved oxygen, sea surface temperature and sea surface salinity

This comprehensive descriptive analysis of key environmental parameters in the Arabian Sea region (Table 1a), including dissolved oxygen in Arabian sea, sea surface salinity, and sea surface temperature, provides valuable insights into the current state of the region's environmental conditions. These parameters play a fundamental role in determining the health, sustainability and dynamics of the marine ecosystem. This analysis has revealed important results: The mean dissolved oxygen in the Arabian Sea is calculated to be 202.50 ± 2.61 mmol/m³, indicating relatively low variability. Sea surface salinity Arabian Sea exhibits an average value of 35.90 PSU, with a small standard deviation of 0.14. Sea surface temperature records a mean value of 27.91ºC; with a standard deviation is 1.03ºC. These findings underscore the relatively stable environmental conditions of the Arabian Sea, critical for maintaining its marine ecosystem.

Pearson correlation (Table 1b**)** analysis of key environmental parameters in the Arabian sea region, including dissolved oxygen, sea surface salinity, and sea surface temperature was conducted to examine the relationships between these variables. The study aims to unravel potential associations and their implications for marine ecosystem dynamics in the Arabian sea region. The dissolved oxygen exhibits a weak negative correlation with sea surface salinity (r = -0.294), indicating that higher sea surface salinity is associated with slightly lower dissolved oxygen levels. Furthermore, dissolved oxygen shows a strong negative correlation with sea surface temperature (r = -0.711), implying that higher sea surface temperature corresponds to significantly lower DO levels. In contrast, sea surface salinity and sea surface temperature demonstrate a weak negative correlation (r = -0.102).

Table 1(a).Analysis of key environmental parameters in the Arabian Sea

Serial number	Parameters	Mean	Standard deviation
1.	Dissolved oxygen	202.50	2.61
2.	Sea surface salinity	35.89	0.13
3.	Sea surface temperature	27.90	1.03

Table 1(b). Pearson correlation and Sigma (1-tailed) over the Arabian Sea

Correlation		Dissolved oxygen	Sea surface salinity	Sea surface temperature
Pearson correlation	Dissolved oxygen	1.00	-0.29	-0.71
	Sea surface salinity	-0.29	1.00	-0.10
	Sea surface temperature	-0.71	-0.10	1.00
Note:Significance: $p < 0.05$; $p < 0.001$.				

Table 1(c) Multiple linear regression models predicting dissolved oxygen in Arabian Sea

Multiple linear regression model								
Data	R	R square	Adjusted R square	Std. error of the estimate	Change statistics			
					R square change	F Change	Degree of freedom 1	Degree of freedom 2
	0.800	0.640	0.638	1.5726232	0.640	243.940	2	274
a. Dependent variable: Dissolved oxygen [mmol/m³]								
b. Predictors: Sea surface temperature [°C], Sea surface salinity [PSU]								

Table 2(a). Descriptive statistics of the Bay of Bengal

Serial number	Parameters	Mean	Standard deviation
1.	Dissolved oxygen	204.14	2.73
2.	Sea surface salinity	32.44	0.41
3.	Sea surface temperature	28.71	0.82

Table 2(b). Pearson correlation matrix for environmental parameter in Bay of Bengal.

Correlation		Dissolved oxygen	Sea surface salinity	Sea surface temperature
Pearson correlation	Dissolved oxygen	1.000	-0.272	-0.837
	Sea surface salinity	-0.272	1.000	-0.272
	Sea surface temperature	-0.837	-0.224	1.000
Note: Significance: $p < 0.05$; $p < 0.001$.				

Table 2(c). Multiple linear regression models statistics Bay of Bengal.

Multiple linear regression model								
					Change statistics			
Data	R	R Square	Adjusted R Square	Std. error of the estimate	R Square change	F change	Degree of freedom 1	Degree of freedom 2
	0.842	0.709	0.707	1.4832988	0.709	333.798	2	274
a. Dependent Variable: Dissolved oxygen [mmol/m³] b. Predictors: Sea surface temperature [°C], Sea surface salinity [PSU]								

A multiple linear regression model (Table 1c) was developed to predict dissolved oxygen (DO) variability in the Arabian Sea using sea surface temperature (SST) and salinity (SSS) as predictors. The model explains 64% of the variance in DO levels ($R^2 = 0.640$, Adjusted $R^2 = 0.638$) and demonstrates strong statistical significance ($F = 243.940$, $p < 0.001$). The high correlation coefficient ($R = 0.800$) and low standard error (1.573 mmol/m³) underscore the model's precision and confirm that SST and SSS are critical drivers of dissolved oxygen dynamics in the region, indicating that the inclusion of the predictor variables has significantly improved the model's fit.

Bay of Bengal exhibits (Table 2a) stable environmental conditions, with dissolved oxygen averaging 204.15 mmol/m³ (±2.73), sea surface salinity at 32.45 PSU (±0.41), and sea surface temperature of 28.71°C (±0.82). Low variability across these parameters suggests consistent hydrological and thermal regimes. These stable conditions likely enhance ecological resilience, supporting complex marine ecosystems. Such equilibrium underscores the Bay's role as a vital refuge for marine life amid global environmental changes.

Dissolved oxygen in the Bay of Bengal (Table 2b) declines significantly with rising sea surface temperature ($r = -0.837$, $p < 0.001$) and moderately with increasing salinity ($r = -0.272$, $p < 0.05$). Salinity and temperature show no significant correlation ($r = -0.224$, $p > 0.05$), highlighting sea surface temperature as the dominant driver of oxygen variability. These results align with the thermodynamic principle that warmer waters reduce oxygen solubility. The findings emphasize sea surface salinity critical role in predicting climate-driven oxygen depletion, vital for managing marine ecosystems.

The multiple linear regression model (Table 2c) accounted for 70.9% of the variance ($R^2 = 0.709$, $F(2, 274) = 333.80$, $p < 0.001$) in dissolved oxygen concentrations within the Bay of Bengal, with sea surface temperature and sea surface salinity emerging as statistically significant predictors. Sea surface temperature demonstrated the strongest inverse association, consistent with the thermodynamic regulation of oxygen solubility in aqueous systems, wherein elevated temperatures reduce gas retention capacity. Sea surface salinity exhibited a moderate negative correlation, suggesting salinity-driven stratification or mixing processes may marginally attenuate oxygen availability. These results underscore sea surface temperature as the principal determinant of oxycline variability, with critical implications for predicting hypoxia under anthropogenic warming scenarios and informing adaptive management of pelagic ecosystems.

CONCLUSIONS

Following major conclusions can be drawn from the present study

1. Significant decline in dissolved oxygen levels in both the Arabian sea and the Bay of Bengal, with Arabian sea experiencing a sharper decrease compared to Bay of Bengal. This oxygen loss coincides with increasing sea surface temperature in both regions, with Arabian sea also showing a slight rise in sea surface salinity, while Bay of Bengal exhibits freshening.

2. A strong inverse correlation between sea surface temperature and dissolved oxygen is observed, with regression models attributing dissolved oxygen variability to sea surface temperature changes.

3. Regionally, Arabian sea maintains higher salinity with moderate dissolved oxygen, while Bay of Bengal, influenced by freshwater influx, has lower salinity but slightly higher dissolved oxygen.

4. Seasonal dynamics reveal a pre-monsoon dissolved oxygen drop in Arabian Sea, as sea surface temperature rises, followed by a monsoon-induced recovery, while Bay of Bengal, experiences post-monsoon dissolved oxygen peaks due to mixing but pre-monsoon stratification-induced declines.

5. Anthropogenic influences and climate drivers, including warming, salinification, and monsoon variability, exacerbate hypoxia risks, with Arabian sea show increased stratification and reduced ventilation, while Bay of Bengal freshening trends intensify oxygen loss.

6. Predictive models confirm sea surface temperature and SSS as major dissolved oxygen determinants, with Arabian sea regression model indicating moderate predictive power, whereas Bay of Bengal model underscores sea surface temperature dominant influence.

ACKNOWLEDGEMENTS

The authors are very thankful to the Copernicus Marine Environment Monitoring Service (http://marine.copernicus.eu/) for providing the data used in this study.

The authors also thank the anonymous reviewer for their objective evaluation and useful suggestions, which greatly enhanced the quality of this work. The authors acknowledge the K. Banerjee Centre of Atmospheric and Ocean Studies, Institute of Inter disciplinary Studies, Nehru Science Centre, University of Allahabad, Prayagraj for providing facilities.

Author Credit Statement

Siddharth Srivasatv, Vivek Kumar Pandey, Yaduvendra Singh, and Prabha Kushwaha conducted data analysis and wrote the manuscript. Siddharth Srivasatv contributed to data analysis and interpretation.

Data Availability Statement

The data sets used in this study are publicly available Global ocean analysisv3.6 NEMO (EU, 2023).

Compliance with Ethical Standard

The authors declare that they have no conflict of interest and adhere to copyright norms.

REFERENCE

Akhil, V.P., Durand, F., Lengaigne, M., Vialard, J., Keerthi, M.G., Gopalakrishna, V.V., Deltal, C., Papa, F. and Montegut, C., 2014. A modelling study of the processes of surface salinity seasonal cycle in the Bay of Bengal. J. Geophys. Res., Oceans, 119(6), 3926-3947.

Bushinsky, S.M. and Emerson, S.R., 2018. Biological and physical controls on the oxygen cycle in the Kuroshio Extension from an array of profiling floats. Deep-Sea Res. I: Oceanogr. Res. Pap., 141, 51–70.

Chowdary, J.S., Chaudhari, H.S., Gnanaseelan, C., Parekh, A., Suryachandra Rao, A., Sreenivas, P. and Singh, P., 2014. Summer monsoon circulation and precipitation over the tropical Indian Ocean during ENSO in the NCEP climate forecast system. Clim. Dyn., 42(7–8), 1925–1947.

Colborn, J.G., 1975. The thermal structure of the Indian Ocean (Vol.2) Honolulu: University of Hawaii Press.

Diaz, R.J. and Rosenberg, R., 2008. Spreading dead zones and consequences for marine ecosystems. Science, 321(5891), 926–929.

Du, Y., Zhang, Y. and Shi, J., 2019. Relationship between sea surface salinity and ocean circulation and climate change. Science China Earth Sci., 62(5), 771–782.

Emerson, S.R. and Bushinsky, S., 2014. Oxygen concentrations and biological fluxes in the open ocean. Oceanography, 27(1), 168–171.

EU., 2023. Copernicus marine service information (CMEMS) (dataset). Marine data store (MDS) GLOBAL -Multiyear-PHY-001-030. https://doi.org/10.48670/moi-00019.rg

IPCC, 2018. Global warming of 1.5°C: an IPCC special report on the impacts of global warming of 1.5°C above pre-industrial levels and related global greenhouse gas emission pathways, in the context of strengthening the global response to the threat of climate change, sustainable development, and efforts to eradicate poverty. Cambridge Univ. Press, Cambridge. https://doi.org/10.1017/9781009157940

Jana, S., Gangopadhyay, A. and Chakraborty, A., 2015. Impact of seasonal river input on the Bay of Bengal simulation. Continental Shelf Res., 104, 45–62.

Keeling, R.F., Körtzinger, A. and Gruber, N., 2010. Ocean deoxygenation in a warming world. Ann. Rev. Marine Sci., 2(1), 199–229.

Li, T., Zhang, Y., Chang, C.P. and Wang, B., 2001. On the relationship between Indian Ocean sea surface temperature and Asian summer monsoon. Geophys. Res. Lett., 28(14), 2843–2846.

Menzel, D.W. and Spaeth, J. P., 1962. Occurrence of ammonia in Sargasso Sea waters and in rainwater at Bermuda 1. Limnol. Oceanogr, 7(2), 159–162.

Murtugudde, R., Seager, R. and Thoppil, P., 2007. Arabian Sea response to monsoon variations. Paleoceanography, 22(4), PA4216.

Pena, M.A., Katsev, S., Oguz, T. and Gilbert, D., 2010. Modeling dissolved oxygen dynamics and hypoxia. Biogeosciences, 7(3), 933–957.

Rao, R.R. and Sivakumar, R., 2003. Seasonal variability of sea surface salinity and salt budget of the mixed layer of the north Indian Ocean. J. Geophys. Res., Oceans, 108(C1), 3009.

Schmidt, J.O., Bograd, S.J., Arrizabalaga, H., Azevedo, J.L., Barbeaux, S.J., Barth, J.A. and Zawislak, P.A., 2019. Future ocean observations to connect climate, fisheries, and marine ecosystems. Front. in Marine Sci., 6, 550.

Shenoi, S.S.C., Shankar, D. and Shetye, S.R., 2002. Differences in heat budgets of the near-surface Arabian Sea and Bay of Bengal: Implications for the summer monsoon. J. Geophys. Res., Oceans, 107(C6), 5-1.

Smith, C.J., Kramer, R.J., Myhre, G., Alterskjær, K., Collins, W., Sima, A., and Forster, P.M., 2020. Effective radiative forcing and adjustments in CMIP6 models. Atmosph. Chem. Phys., 20(16), 9591–9618.

Stramma, L., Johnson, G.C., Sprintall, J. and Mohrholz, V., 2008. Expanding oxygen-minimum zones in the tropical oceans. Science, 320(5876), 655–658.

Thangaprakash, V.P., Girishkumar, M.S., Suprit, K., Kumar, N.S., Chaudhuri, D., Dinesh, K. and Weller, R.A., 2016. What controls seasonal evolution of sea surface temperature in the Bay of Bengal? Mixed layer heat budget analysis using moored buoy observations along 90°E. Oceanography, 29(2), 202–213.

Vinayachandran, P.N., 2004. Summer cooling of the Arabian Sea during contrasting monsoons. Geophys. Res. Lett., 31(13), L13305.

Wilson-Diaz, D., Mariano, A.J. and Evans, R.H., 2009. On the heat budget of the Arabian Sea. Deep-Sea Res. I: Oceanogr. Res. Pap, 56(2), 141-65.

Received on: 11-02-2024; Revised on: 01-05-2025 ; Accepted on: 19-05-2025

J. Ind. Geophys. Union, 29(4) (2025), 260-275
https://doi.org/10.71122/JIGU.29(4)2025.0025

Seismic risk assessment using analytic hierarchy process: An integrated approach for Varanasi city, India

Shashank Shekhar[1], Anurag Tiwari[1, 2*], J. L. Gautam[2] and G. P. Singh[1]
[1]Department of Geophysics, Banaras Hindu University, Varanasi-221005, India
[2]National Centre for Seismology, Ministry of Earth Sciences, New Delhi-110003, India
* Corresponding author: aaanuragt@gmail.com

ABSTRACT

Seismic hazards present significant risks to urban areas, highlighting the need for a comprehensive earthquake risk assessment (ERA) to enhance disaster preparedness. This study utilizes the Analytic Hierarchy Process (AHP) methodology to construct an integrated ERA map using Geographic Information System (GIS) for Varanasi city, which is one of the most densely populated cities of Northern India, located in the Indo-Gangetic plain. The AHP framework created a pairwise comparison matrix to assess the relative significance of factors affecting seismic risk, such as peak ground acceleration, geology, geomorphology, building density, population density, literacy, transports and building typology. Weights were based on global studies with similar characteristics, expert advice and consistency checks to ensure coherence in comparisons. Integrated AHP model is used to generate seismic hazard index and vulnerability index which is then integrated to develop a comprehensive seismic risk map using GIS. As a result, Varanasi City is classified into five zones of seismic risk levels, ranging from very low to very high for the seismicity occurrence with a 10% probability of exceedance and a 2% probability of exceedance in 50 years. Our study finds that 6.92% of the area of Varanasi city lies in the very high seismic risk zone (Zone 5), followed by 23.88% in high risk, 21.32% moderate, 20.25% low, and 27.66% very low risk (zone 1) for the seismicity occurrence with 10% probability of exceedance in 50 years (DBE). For a 2% probability of exceedance in 50 years (MCE), the distribution slightly changes, with 26.14% in very low, 21.24% low, 23.31% moderate, 21.69% high, and 7.62% area lie in very high seismic risk zones (Zone 5).

Keywords: Seismic, hazard, vulnerability, risk, Varanasi city, Analytic Hierarchy Process (AHP).

INTRODUCTION

Varanasi, an ancient city in northern India, known for its rich cultural and religious heritage, is at significant seismic risk due to its location in the seismically active Gangetic Plain. As one of the most populated cities in northern India, Varanasi is vulnerable to potentially devastating earthquakes from nearby faults and tectonic features such as the Himalayan Frontal Thrust (HFT), ridges, and faults (Sahu and Saha, 2014; Singh et al., 2020). The city's aging infrastructure, with many buildings either very old and damaged or possessing specific structural weaknesses, further compounds its vulnerability to earthquake hazards (Jha and Bajwa, 2023). The presence of geological structures like the Faizabad Ridge, Allahabad Fault, Azamgarh Fault, Devoria Fault, Patna Fault, and the Siwan Fault, are capable of generating earthquakes or reactivating during large Himalayan seismic events, which is a matter of grave concern (Sahu and Saha, 2014; Singh et al., 2020). Notably, the HFT, the surface expression of the Main Himalayan Thrust, facilitates the northward movement of the Indian plate, often resulting in large earthquakes (Seeber and Armbruster, 1984). The thick quaternary alluvial deposits, ranging from clay to gravelly sand formations (Shukla and Raju, 2008), coupled with the low-lying terrain, heighten the city's susceptibility to seismic events and flooding hazards (Pandey et al., 2021). Geomorphological investigations have unveiled the intricate network of drainage systems and fluvial landforms that shape the Varanasi district, with the Varuna River basin serving as a focal point for comprehensive analysis (Prakash et al., 2016). These geological and geomorphological factors contribute to the region's complex hazard profile, necessitating a thorough understanding for effective risk assessment and mitigation strategies. The Varanasi city region chosen for the comprehensive risk assessment is shown in Figure 1.

Several studies have earlier assessed seismic hazard and risk in Varanasi and other regions using geological, geophysical, and geotechnical data (Nath et al., 2019; Singh, 2022; Tiwari et al., 2024). Using GIS and seismic hazard parameters, a seismic microzonation map for Delhi (India), has been developed by Mohanty et al. (2007). Anbazhagan et al. (2010) utilized probabilistic and deterministic approaches to assess seismic hazard and develop seismic risk maps for the Bangalore region. The Seismotectonic setup around Varanasi city is shown in Figure 1 (Bhukosh-GSI, 2023).

Various approaches have been employed for seismic risk assessment and hazard mapping in past. These include Probabilistic Seismic Hazard Analysis (PSHA), which incorporates the probability of seismic events, ground motion attenuation models, and site conditions to estimate ground motion levels (Kramer, 1996), and Deterministic Seismic Hazard Analysis (DSHA), which considers the worst-case scenario of a maximum credible earthquake (Rasool et al., 2024; Tilara et al., 2024).

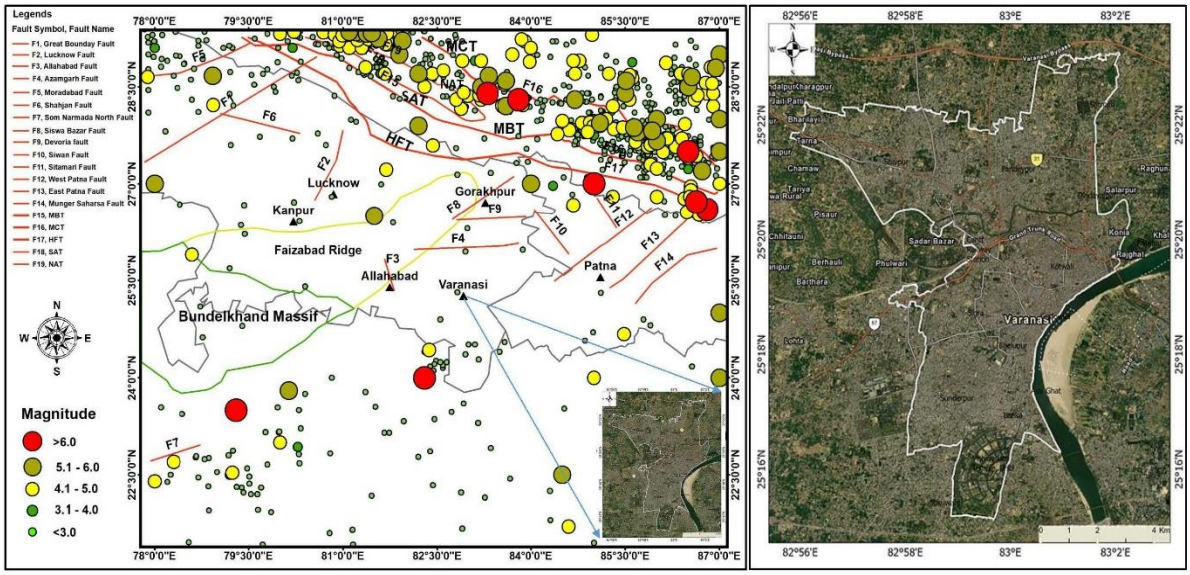

Figure 1. Seismotectonic setup around Varanasi city, India (Left) adopted from GSI (Bhukosh-GSI.gov.in) and study area of Varanasi City (Right)

Other techniques involve Geographic Information System (GIS) for spatial data analysis and integration of geology, geomorphology, and seismic sources (Napieralski et al., 2012), Artificial Neural Networks (ANNs) and Machine Learning (ML) for pattern recognition, data analysis, and predictive modelling (Raschka and Mirjalili, 2017), as well as Multicriteria Decision Analysis (MCDA) techniques like TOPSIS, ELECTRE, and PROMETHEE for decision-making processes (Ishizaka and Nemery, 2014). However, these methods may not fully account for the complex interplay of various geological, geomorphological, and anthropogenic factors that can significantly influence seismic hazard at a local level.

In this study, we developed a seismic risk map for the city of Varanasi, India, using the Analytic Hierarchy Process (AHP), which is a powerful multi-criteria decision-making technique. The AHP, introduced by Saaty (1980), is a structured method that involves pairwise comparisons of decision criteria to derive their relative weights or priorities. These weights are then used to evaluate and rank alternative decisions or scenarios. The AHP has been widely applied in various domains, including natural hazard risk assessment (Ayalew et al., 2004; Ercanoglu and Gokceoglu, 2004; Lari et al., 2009). Specifically, for seismic risk mapping, the AHP allows the integration of multiple factors influencing seismic hazard, such as peak ground acceleration, geology, soil characteristics, and building density, into a comprehensive decision model. In present study, by constructing pairwise comparison matrices, calculating priority vectors, and ensuring consistency in judgments, the AHP provided a robust framework for evaluating and prioritizing seismic risk factors, ultimately leading to the generation of a seismic risk map for Varanasi city.

DATA SOURCE

The data for the various parameters influencing seismic hazard in Varanasi City, were acquired from diverse sources. The geological information was obtained from the Geological Survey of India (Bhukosh-GSI, 2023). The geomorphological data were derived from USGS satellite imagery, Google Earth data, and manual field visits to the study area (USGS, 2023). The seismotectonic data, including information on active faults and historical seismicity, were compiled from the Geological Survey of India and the International Seismological Centre databases (Bhukosh-GSI, 2023; ISC, 2023). The rock level peak ground acceleration (PGA) values were sourced from the study of Nath (2017) and Nath et al. (2019) and surface PGA values were sourced from Tiwari et al. (2024). Shear wave velocity data was obtained from Singh et al. (2020). Population density data were obtained from the 2011 Census of India and the Ministry of Housing and Urban Affairs (Census India, 2011). Information on building typologies was gathered through manual field visits, satellite imagery, google earth and surveys conducted within the city limits. The water table depth data were acquired from the reports of Central Ground Water Board (CGWB, 2023). Additionally, data on soil properties, such as the Standard Penetration Test (SPT-N) values, were obtained from the Varanasi Development Authority's records and site investigations (VDA, 2022).

ANALYTIC HIERARCHY PROCESS FRAMEWORK

The Analytic Hierarchy Process (AHP) is a technique for dealing with complex decisions by breaking them down into a

hierarchy of criteria of goal, criteria, and alternatives (Saaty, 1980). In 1970, it was developed after recognizing the human mind's limited ability to integrate large amounts of information in making reasoned choices. AHP provided a way to combine logic and intuition in a structured, multi-criteria decision-making process. AHP has been applied extensively in business, government, healthcare, and other sectors to evaluate alternatives against qualitative and quantitative factors (Ishizaka and Labib, 2011). Its key innovation was using pairwise comparisons derived from expert judgments and a proven mathematical foundation to derive accurate priority weights for each element (Saaty, 2008). AHP's sophisticated consistency checking mechanisms and systematic approach allow decision-makers to validate the integrity of their judgments. While computationally intensive compared to other techniques, AHP's inherent strength lies in modelling complex, multi-attribute decisions in a hierarchical structure reflecting real-world systems (Velasquez and Hester, 2013; Saaty, 2013). AHP methodology can be performed under following steps:

Step 1: Problem identification and model build-up

Identify the problem and decide the goal. The decision problem is structured into a hierarchical model. This hierarchical structure facilitates the analysis of the relationships between the elements within the inverted tree-structured network (Alizadeh et al., 2018; Saaty, 2008).

Step 2: Structure the hierarchy (Goal ϵ Criteria ϵ Sub Criteria ϵ Alternatives)

Break down the decision into a hierarchy of criteria, sub-criteria, and alternatives. The goal is placed at the top level, followed by the main criteria, sub-criteria (if any), and finally, the alternatives at the bottom level (Ishizaka and Labib, 2011).

Step 3: Pairwise Comparison Matrix formation

In the AHP, the decision problem is structured into clusters and decision elements at multiple levels of abstraction. For instance, in a vulnerability mapping problem, the first cluster is goal (e.g., vulnerability mapping), the second cluster could represent the main criteria or dimensions, and the third cluster could consist of the indicators or sub-criteria (Saaty, 1980; Alizadeh et al., 2018).

A pairwise comparison of the decision elements is conducted within each group, their relative importance is determined by comparing them in pairs against the criteria or higher-level element they belong to. The different criteria are also compared in pairs to assess how they depend on each other. These paired comparisons use a scale from 1 to 9, where 1 means the two elements are equally important, and 9 means one element is extremely more important than the other (Saaty, 1980; Panahi et al., 2014). Saaty, (1980) used rating scale as, 1 = Equal importance, 3: Moderate importance, 5: Strong importance, 7: Very strong importance, and 9: Extreme importance. To facilitate the compromises between slightly differing judgments, the numbers 2, 4, 6, 8, and their reciprocals could be used. The pairwise comparisons are organized in a square matrix, where the matrix element a_{ij} represents the relative importance of the i_{th} element over the j_{th} element. For the reciprocal comparison, the matrix element a_{ji} is set as the reciprocal value of a_{ij}, indicating the relative importance of the j_{th} element over the i_{th} element (Alizadeh et al., 2018).

Step 4: Derive priority vectors (weights)

The local priority vector (V), representing the relative weights or priorities of the decision elements, is obtained by calculating the principal eigenvector of the pairwise comparison matrix (A). This can be represented by the equation:

$$AW = \lambda\max * V \quad (1)$$

Where A is the pairwise comparison matrix, W is the eigenvector representing the priority vector, and λ_{max} is the maximum eigenvalue of the matrix A (Alizadeh et al., 2018).

Step 5: Consistency check

To ensure the consistency of the pairwise comparisons, the Consistency Ratio (CR) is calculated using the following equations

Consistency Index, $CI = (\lambda max - n) / (n - 1)$ (2)

Consistency Ratio, $CR = CI / RI$ (3)

Where n denotes order of the pairwise comparison matrix, and RI denotes Random Consistency Index, which represents the average consistency index for randomly generated matrices of the same order (Saaty, 1980). If the calculated CR value is less than or equal to 0.1, the pairwise comparisons are considered acceptably consistent. Otherwise, the pairwise comparisons need to be revised until an acceptable consistency ratio is achieved (Saaty, 1980; Alizadeh et al., 2018).

Step 6: Calculation of the Super matrix

In the AHP, pairwise comparisons are used to estimate the super matrix, which is partitioned based on the clusters and elements of the decision hierarchy. The super matrix is a matrix representation of the relationships between the elements and clusters (Saaty, 1980; Alizadeh et al., 2018). Consider a decision problem with N clusters, denoted as C_1, C_2, C_3, ..., C_n. Each cluster C_k contains m_k elements, represented as (e_{k1}, e_{k2}, ..., e_{kmk}). The super matrix can be expressed as:

$$W = \begin{vmatrix} W_{11} & W_{12} & \dots & W_{1N} \\ W_{21} & W_y & \dots & W_{1N} \\ \dots & \dots & \dots & \dots \\ W_{N1} & W_{N2} & \dots & W_{NN} \end{vmatrix} \quad (4)$$

Where W_{ij} is the priority vector representing the relative importance or priority of the elements in cluster i with respect to the elements in cluster j. The priority vectors are derived from the pairwise comparison matrices (Alizadeh et al., 2018).

Step 7: Selection of Alternatives

The super matrix is used to select the best alternative based on the overall priorities derived from the AHP analysis by raising the super matrix to powers until it converges to a stable state, known as the limiting super matrix, which represents the overall priorities of the alternatives with respect to the goal. The alternative with the highest priority is considered the best choice. Sensitivity analysis can be performed to assess the robustness of the alternative rankings by varying the criteria weights. This process is essential for making informed decisions and achieving the desired objectives (Saaty, 1980; Alizadeh et al., 2018). A flow chart of holistic AHP framework is illustrated in Figure 2.

Weightage parameters and rankings

In this study, we employed the Analytic Hierarchy Process (AHP) to generate a comprehensive seismic risk map for Varanasi City, India, by evaluating and integrating multiple weighted parameters. The parameters considered were Peak Ground Acceleration (PGA), geology and geomorphology, water table depth, shear wave velocity (Vs30), EBR based SPT-N (Standard Penetration Test), population density, building density, educated people density, Distribution of universities, major offices, transport nodes, district office, and distance from service centres. These parameters were selected based on their significant influence on seismic hazard and vulnerability assessment. Population density accounts for the exposure of people and infrastructure to ground shaking, while PGA quantifies the maximum ground acceleration experienced during an earthquake. Geology, geomorphology, and water table depth affect the propagation and amplification of seismic waves, as well as the potential for ground failure and liquefaction. Building typology represents the structural characteristics and construction materials, which play a crucial role in their vulnerability to seismic events. Vs30 and SPT-N, provide insights into site amplification effects and soil strength, respectively, influencing the potential for structural damage

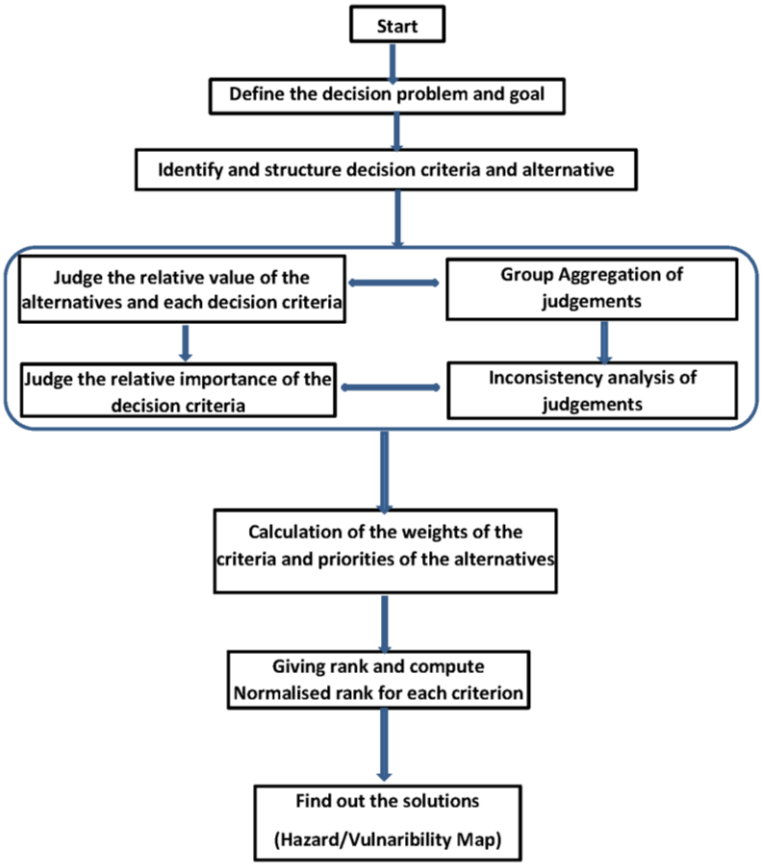

Figure 2. Flow chart of Analytic Hierarchy Process (AHP) methodology

Table 1. Evaluation of weights and ranks of layer for hazard estimation

Category	Rank	Weight
PGA	1	5
EBR(N)	2	4
GG	3	3
Vs (30)	4	2
WT	5	1

Table 2. Evaluation of weights and ranks of layer for vulnerability estimation

Factors	Rank	Weight
a) Population density	1	8
b) Educated people density	2	7
c) Building density	3	6
d) Distribution of universities	4	5
e) Major offices	5	4
f) Transport nodes	6	3
g) District office	7	2
h) Distance from service centres	8	1

Table 1 represents the assigned weights and ranks for various layers used in hazard estimation and Table 2 represents the assigned weights and ranks for various layers used in vulnerability estimation. The layers are prioritized and weighted based on their importance in assessing hazards and vulnerability. In hazard evaluation, the Peak Ground Acceleration (PGA) is ranked first with the highest weight of 5, indicating its critical role. The engineering bed rock depth based on SPT-N values (EBR(N)) follows as the second most important layer with a weight of 4. Geology and geomorphology (GG) is ranked third and assigned a weight of 3, reflecting its moderate significance. The fourth rank is held by the average shear wave velocity Vs (30), with a weight of 2, suggesting a lower relative importance. Finally, water table (WT) is ranked fifth and given the lowest weight of 1, indicating it has the least impact among the evaluated layers. This hierarchical structuring helps in systematically assessing and prioritizing the factors involved in hazard estimation. Ranks and weights' assignment done after several iterative process by checking consistency of pair wise matrix is presented in Table 3 as a result of ranks and weights' assignment.

Pair wise comparison and consistency check

The level of seismic hazard in the study area was defined based on a combination of historical earthquake records, statistical analyses, and the AHP-based prioritization of seismic hazard factors. The Varanasi region is situated in the proximity to seismically active Himalayan Frontal Thrust (HFT) and other tectonic features, making it susceptible to potential high-intensity earthquakes (Bilham, 2004; Malik et al., 2015). Using the AHP methodology, various seismic hazard parameters PGA, local geological and geomorphological factors, water table depth, Vs30 and Engineering bed rock depth were weighted and integrated to develop a composite seismic hazard index map. The decision matrix based on weighted and ranked hazard parameters (Table 1) is shown in Table 3 for hazard assessment. A total 10 pairwise comparisons were performed, to achieve a consistency ratio (CR) of 0.0004 (i.e., 0.04%), which quite acceptable range, indicating that our scrutinized judgments are consistent. The calculated principal eigenvalue for this pair matrix was 5.001, and the eigenvector solution achieved after four iterations. The eigen vector solution is shown in Table 3.

Similarly, the pair wise comparison matrix for vulnerability assessment is shown in Table 4, which is used for priority matrix calculation (Table 2), along with their corresponding eigenvalues and consistency ratios. Consistency of pair wise matrix reviewed through several iterative process and validated the obtained weights and ranks, ensuring the appropriate adaptation of the AHP approach and the accuracy of the resulting vulnerability map. All the relevant layers, representing different vulnerability factors, were analysed for their significance using the AHP ranking approach and subsequently integrated within a Geographic Information System (GIS) environment for vulnerability mapping.

A total 28 pairwise comparisons were performed, to get consistency ratio (CR) of 0.0026 (i.e., 0.26%), which quite acceptable range, indicating that our scrutinized judgments are consistent. The principal eigenvalue was 8.03, and the eigenvector solution achieved after five iterations**.** Priority weights for hazard map is shown in Table 5(a) and for vulnerability estimation shown in Table 5(b).

Table 3. Decision matrix for hazard assessment

Goal	PGA	EBR(N)	GG	Vs(30)	WT
PGA	1	3	5	7	9
EBR(N)	0.33	1	3	5	7
GG	0.20	0.33	1	3	5
Vs (30)	0.14	0.20	0.33	1	3
WT	0.11	0.14	0.20	0.33	1

CR = 0.0004 (or 0.04%)
λ max = 5.0016

Table 4. Decision matrix for vulnerability assessment

Goal	a	b	c	d	e	f	g	h
a	1	3	5	7	9	9	9	9
b	0.33	1	3	5	7	7	7	9
c	0.20	0.33	1	3	5	5	7	7
d	0.14	0.20	0.33	1	3	3	5	5
e	0.11	0.14	0.20	0.33	1	1	3	3
f	0.11	0.14	0.20	0.33	1	1	3	3
g	0.11	0.14	0.14	0.20	0.33	0.33	1	1
h	0.11	0.11	0.14	0.20	0.33	0.33	1	1

CR = 0.0026 (or 0.26%)
λmax = 8.02612

Table 5(a). Priority weights for Hazard estimation

Parameters	Priority Weights
PGA	0.53
WT	0.23
EBR	0.13
GG	0.07
Vs30	0.03

Table 5(b). Priority weights for Vulnerability estimation

Parameters	Priority weights
a) Population density	0.43330
b) Educated People density	0.28570
c) Building density	0.20240
d) Distribution of universities	0.11430
e) Major offices	0.05710
f) Transport nodes	0.05710
g) District office	0.02860
h) Distance from service centres	0.02860

The heat map in Figure 3 illustrates the relative priority of various factors (layers) used in vulnerability mapping, labelled as (a) to (h). These factors correspond to the layers detailed in Table 2 and include: (a) Population density, (b) Educated people density, (c) Building density, (d) Distribution of universities, (e) Major offices, (f) Transport nodes, (g) District office, and (h) Distance from service centres. The heat map visually represents the weight or significance of each factor in the context of vulnerability assessment, with varying colour intensities indicating their relative importance. For instance, factors such as population density and building density might show higher priority due to their direct impact on vulnerability, while others like the distribution of universities or distance from service centres may have comparatively lower priority.

This visualization helps stakeholders identify which factors contribute most significantly to vulnerability, enabling more targeted and effective planning and mitigation strategies.

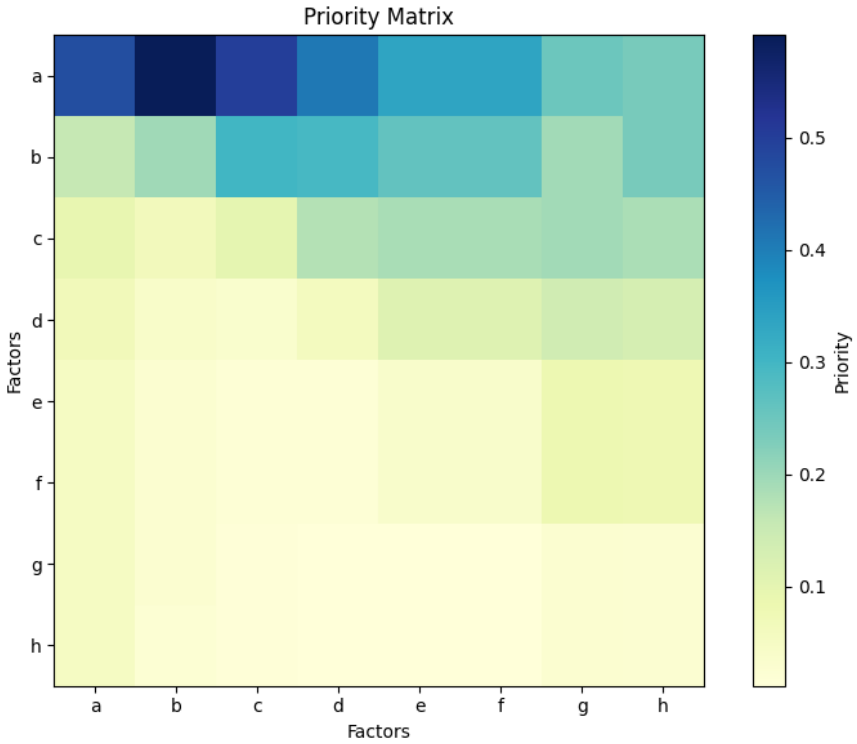

Figure 3. Heat map showing assigned relative priority weights of factors, **a**. Population density, **b**. Educated people density, **c**. Building density, **d.** Distribution of universities, **e**. Major offices, **f.** Transport nodes, **g.** District office, and **h.** Distance from service centres for vulnerability mapping

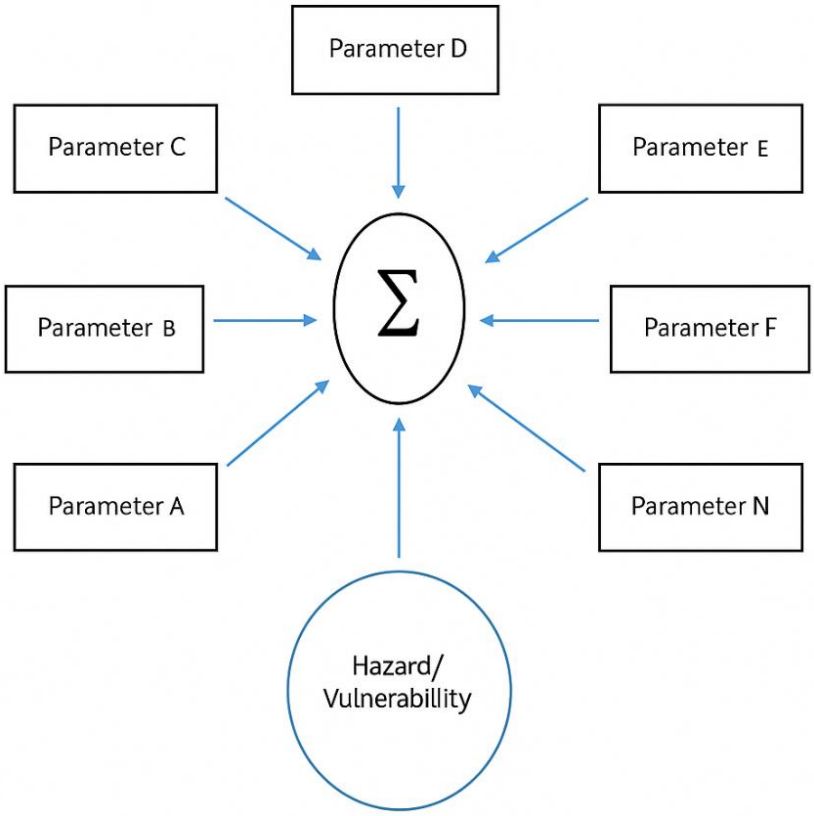

Figure 4. Generalised integration model for hazard and vulnerability assessment

Integration model

The hazard map of Varanasi city has been generated by integrating the various hazard parameters as mentioned in Table 1 and for vulnerability map by integrating the various vulnerability parameters as mentioned in Table 2. A general integration model for accessing the hazard index map and vulnerability index map is illustrated in the Figure 4, in which parameters A to N are general parameter which has been replaced by Table 1 parameters for the generation of integrated hazard map, while by Table 2 parameters used for the generation of integrated vulnerability map.

RESULTS AND DISCUSSION

The assessment of seismic risk in the Varanasi region necessitates a comprehensive evaluation of multiple geological, geomorphological, seismological, and socio-economic indicators. The local geological setting of Varanasi is characterized by unconsolidated Quaternary alluvial sediments (Shukla and Raju, 2008), that could play a significant role in amplifying ground motions during earthquakes (Nath et al., 2008; Alizadeh et al., 2018; Manna et al., 2022). Geomorphological parameters such as curvature and aspect provide insights into sedimentary basin delineation and fault orientation, respectively, contributing to a better understanding of seismic behaviour and ground motion propagation (Kamp et al., 2008; Zebardast, 2013). Seismological indicators, including earthquake magnitude distribution, peak ground acceleration mapping, seismicity spatial distribution, proximity to seismic sources, and fault density, play a crucial role in identifying areas with higher seismic hazard potential (Rashed and Weeks, 2003; Martins et al., 2012; Alizadeh et al., 2018).

Vulnerability assessment considers various socio-economic factors that can exacerbate the impact of seismic events. The region's increasing population particularly in urban areas and thick alluvium settlements, raises concerns about vulnerability (Bilham, 2004; Armas, 2012; Malik et al., 2015; Alizadeh et al., 2018). Educational institutions play a vital role in fostering awareness and preparedness, to potentially reduce vulnerability (Martins et al., 2012; Alizadeh et al., 2018). The resilience of critical infrastructure, services, transportation networks, environmental infrastructure, significantly influences community's ability to respond and recover from seismic events (Rashed and Weeks, 2003; Wisner et al., 2004; Alizadeh et al., 2018). Integrating these multi-faceted indicators through a comprehensive seismic hazard and vulnerability assessment framework is crucial for informed decision-making and risk mitigation strategies in the Varanasi region.

Hazard estimation

A seismic hazard map for the Varanasi region was generated by integrating the results of the Analytic Hierarchy Process incorporating various seismic hazard parameters like PGA, local geological and geomorphological factors, water table depth, Vs30 and engineering bed rock depths. The seismic hazard map for study area of Varanasi city has been developed for 10% probability of exceedance in 50 years (Figure 5) and 2% probability of exceedance in 50 years (Figure 6). The composite seismic hazard map was then classified into five hazard levels as shown in Figures 5 and 6 and hazard index, shown in Tables 6 and 7 using a quantile classification technique.

Very high hazard: Areas with the highest seismic hazard index values greater than 0.70 for seismicity occurrence 10% probability of exceedance in 50 years (DBE) and greater than 0.80 for seismicity occurrence 2% probability of exceedance in 50 years (MCE), indicate a high likelihood of experiencing severe ground shaking and potential damage.

High hazard: Areas with high seismic hazard index values ranges from 0.55 to 0.70, for DBE and ranges from 0.65 to 0.80, for MCE scenario, suggesting a significant risk of strong ground motions and potential damage

Moderate hazard: Areas with moderate seismic hazard index values ranges from 0.40 to 0.55, for DBE and ranges from 0.50 to 0.65, for MCE scenario, where moderate ground shaking and damage may occur.

Low hazard: In areas with lower seismic hazard, index values ranges from 0.25 to 0.40 for DBE and from 0.35 to 0.50 for MCE scenario, indicating a reduced risk of severe ground shaking and damage.

Very low hazard: Areas with the lowest seismic hazard index values less than 0.25 for DBE and less than 0.35 for MCE scenario, suggesting a minimal risk of significant ground shaking and damage.

The resulting seismic hazard map (Figures 5 and 6) identifies the spatial distribution of hazard levels within the study area of Varanasi region. It is important to note that the seismic hazard map should be used in conjunction with vulnerability assessments and risk analyses, to provide a comprehensive understanding of the potential impacts of earthquakes on the built environment, infrastructure, and population. Additionally, regular updates and refinements to the hazard map may be necessary as new data and improved methodologies become available.

Table 6. Hazard index table for 10% probability of exceedance in 50 years

Zone	Hazard level	Hazard index
Zone 1	Very low	<0.25
Zone 2	Low	0.25 -0.40
Zone 3	Moderate	0.40 -0.55
Zone 4	High	0.55 -0.70
Zone 5	Very High	> 0.70

Table 7. Hazard index table for 2% probability of exceedance in 50 years

Zone	Hazard level	Hazard index
Zone 1	Very low	<0.35
Zone 2	Low	0.35 -0.50
Zone 3	Moderate	0.50 -0.65
Zone 4	High	0.65 -0.80
Zone 5	Very High	> 0.80

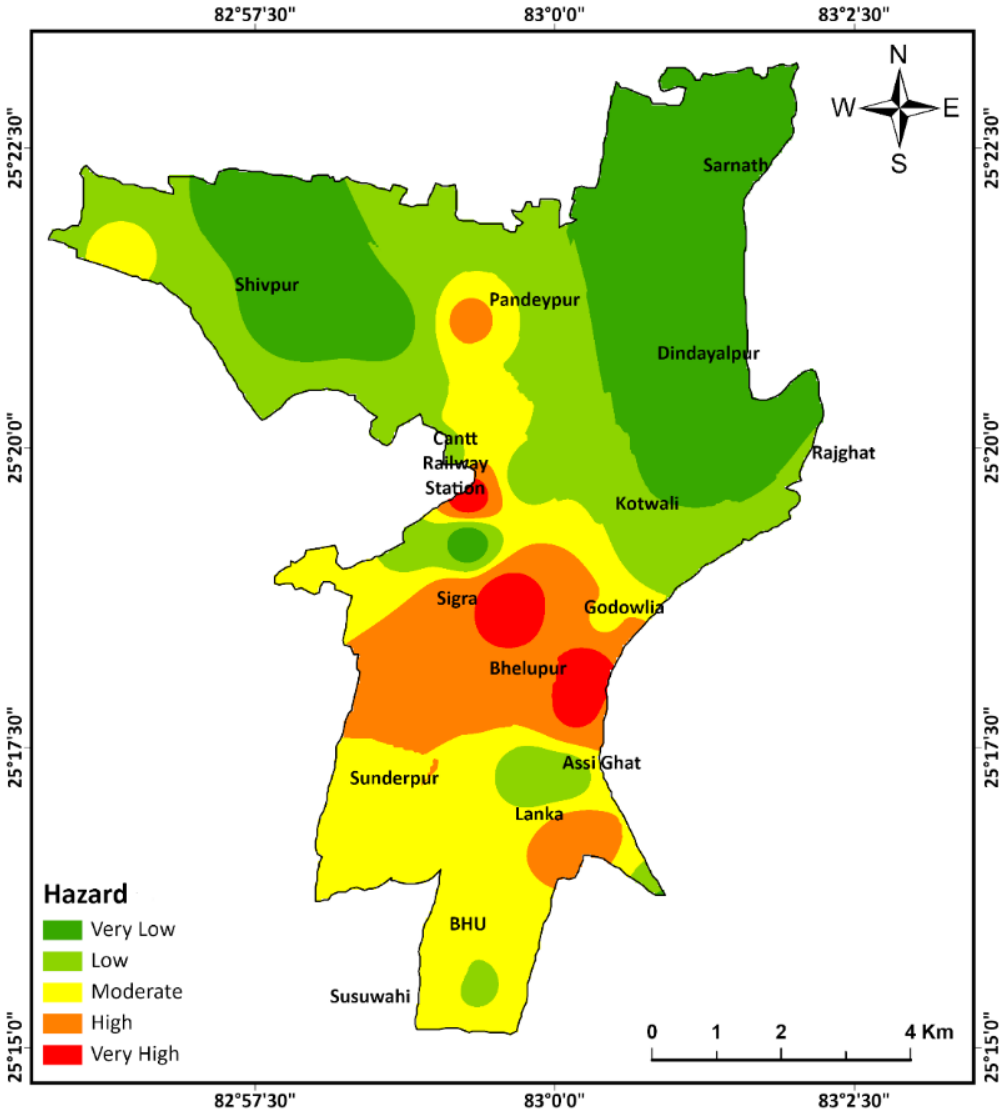

Figure 5. Seismic hazard map of Varanasi city region for 10% probability of exceedance in 50 years

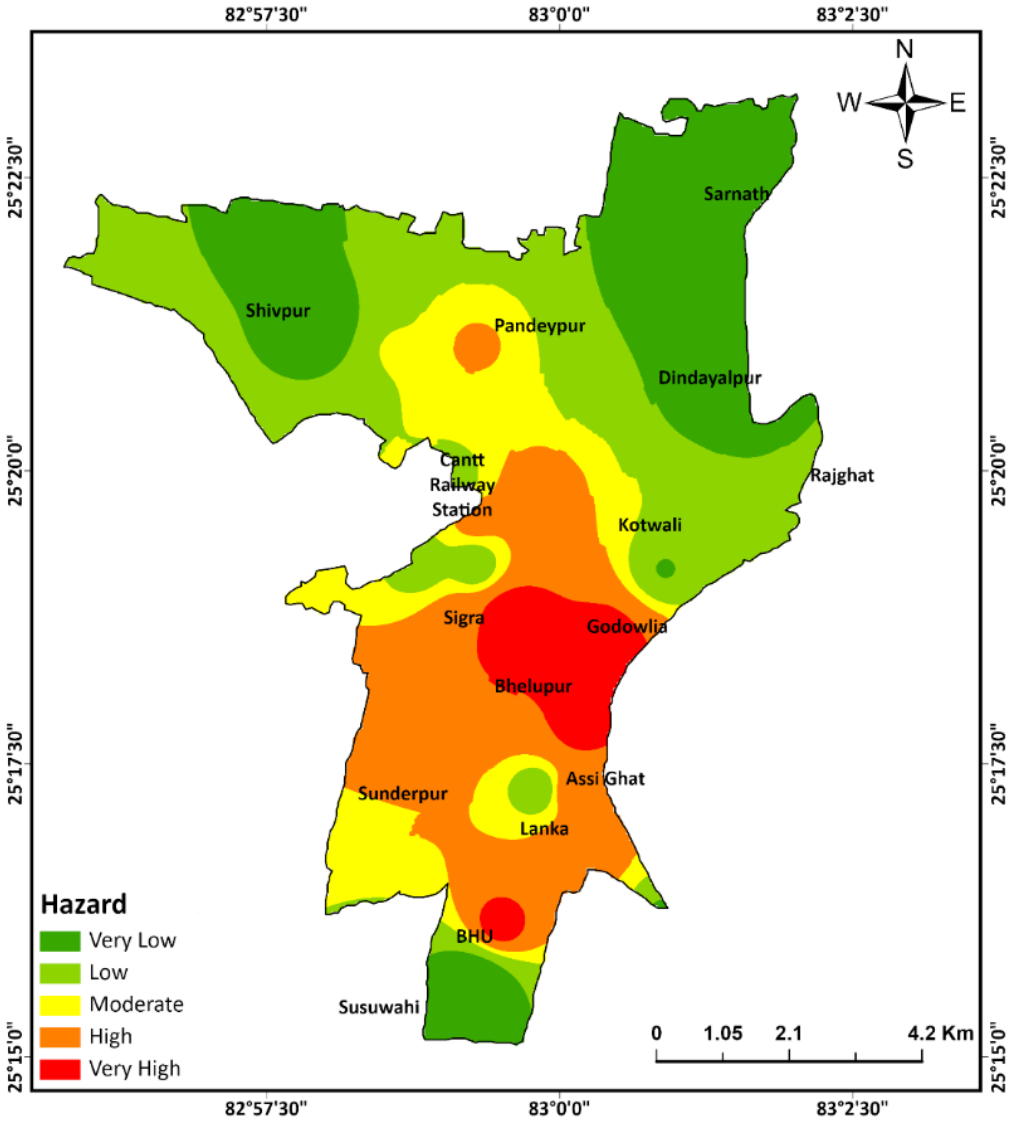

Figure 6. Seismic hazard map of Varanasi city region for 2% probability of exceedance in 50 years

Vulnerability index estimation

The Analytic Hierarchy Process was employed to integrate and aggregate various significant indicators as illustrated in Table 2 for estimating the seismic vulnerability index. A hierarchical structure was developed, considering the relevant criteria and sub-criteria that contribute to seismic vulnerability. The priority of layers and their rankings which used in integration to generate seismic vulnerability map, is given in Table 2. The AHP analysis showed that population density, educational attainment, and building density were ranked as the top three (Table 2) most important criteria, with weights of 43.33%, 28.57%, and 20.24% respectively (Tables 3b and 5b). Major offices, transport nodes, district offices, and distance from service centres are weighted 4, 3, 2, and 1, respectively, reflecting their varying degrees of influence on seismic vulnerability. The resultant vulnerability map is classified into five categories: very low, low, medium, high, and very high vulnerability. The spatial distribution of these vulnerability levels was analysed, and the areas corresponding to each category are illustrated in Figure 7. The vulnerability index categorized zones at distinct levels (Table 8), are based on their susceptibility areas. Zone 1 is classified as having a very low vulnerability with an index of less than 0.25. Zone 2 falls under the Low category, with indices ranging from 0.25 to 0.45. Zones with a moderate vulnerability Zone 3, have indices between 0.45 and 0.65. Similarly, zone 4 is considered a high vulnerability region, with an index range of 0.65 to 0.85. In comparison, zone 5 is marked by a very high vulnerability level, having an index greater than 0.85.

Table 8. Hazard index table for 2% probability of exceedance in 50 years

Zone	Vulnerability level	Vulnerability index
Zone 1	Very low	<0.25
Zone 2	Low	0.25-0.45
Zone 3	Moderate	0.45-0.65
Zone 4	High	0.65-0.85
Zone 5	Very high	>0.85

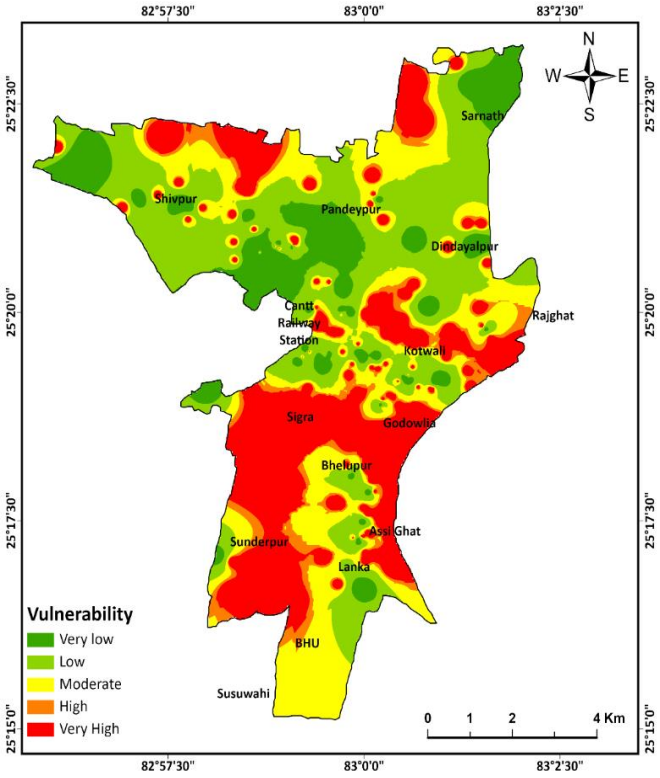

Figure 7. Seismic vulnerability map of Varanasi study region

The Present investigation indicates that the areas with very high vulnerability are concentrated in the central part of the study region due to factors such as high building and population density, the presence of government offices, and a higher concentration of educated individuals. In contrast, very low vulnerability was observed in the northern and north-western part of the region, where these conditions were reversed.

Risk Estimation

A comprehensive seismic risk map for the Varanasi study region was prepared by combining the seismic hazard map and the vulnerability map through spatial multiplication utilizing geographic information system tools. The resultant risk map was classified into five categories (very low, low, moderate, high, and very high risk) using a quantile classification technique (Welle and Birkmann, 2015). The areas corresponding to each risk category was calculated for the entire region and for different zones within the city. The analysis revealed that 6.92% of the total area fell under the very high risk category, while high, moderate, low, and very low-risk zones are represented by 23.88%, 21.32%, 20.25% and 27.66% of the total area, respectively as shown in Table 9 for seismicity occurrence 10% probability of exceedance in 50 years while 7.62% of the total area fell under the extreme risk category, while high, moderate, low, and very low-risk zones represented 21.69%, 23.31%, 21.24 % and 26.14% of the total area, respectively (Table 10) for seismicity occurrence 2% probability of exceedance in 50 years.

Based upon the geographic spatial distribution, the central parts of the city, comprising zones 4, and 5, were identified as areas with high seismic risk. Whereas, northeastern and northwestern part of city belonging to zones 1, 2 and 3 were classified as low-risk areas. High-risk areas are characterized by factors such as high population density, high building density, the presence of educated individuals, government offices, and

proximity to potential seismic sources effects. The potential impacts, population data for the Varanasi region were utilized to estimate the population at risk. Risk mapping was conducted for all the zones within the city, as illustrated in Figures 8 and 9 and graphically presented in Figure 10, highlighting the most clustered risk zones. Based upon detailed calculations of seismic risk area-wise for the different zones, the studied Varanasi city region can be categorized into 5 zones from 1 to 5 as illustrated in Tables 9 and 10 and Figures 8 and 9. Zone 1 showing low risk while zone 5 signifies high risk. Figure 10 is graphical representation of city area belonging to very to very low seismic zone for DBE and MCE scenario both. This risk assessment provided valuable insights for prioritizing risk mitigation efforts, such as targeted seismic retrofitting programs, land-use planning, and emergency preparedness measures within the Varanasi region.

Table 9. Risk level for Varanasi study region for seismicity occurrence for 10% probability of exceedance in 50 years

Zone	Area (%)	Risk level
Zone 1	27.66	Very low
Zone 2	20.25	Low
Zone 3	21.32	Moderate
Zone 4	23.88	High
Zone 5	6.92	Very high

Table 10. Risk level for Varanasi region for seismicity occurrence for 2% probability of exceedance 50 years

Zone	Area (%)	Risk level
Zone 1	26.14	Very low
Zone 2	21.24	Low
Zone 3	23.31	Moderate
Zone 4	21.69	High
Zone 5	7.62	Very high

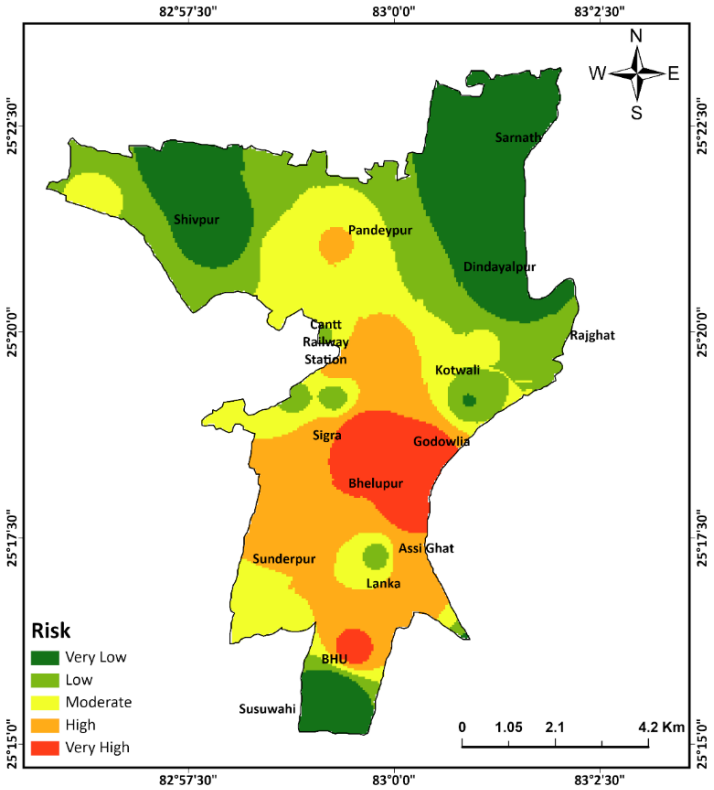

Figure 8. Risk map of Varanasi region for seismicity occurrence 10% probability of exceedance in 50 years

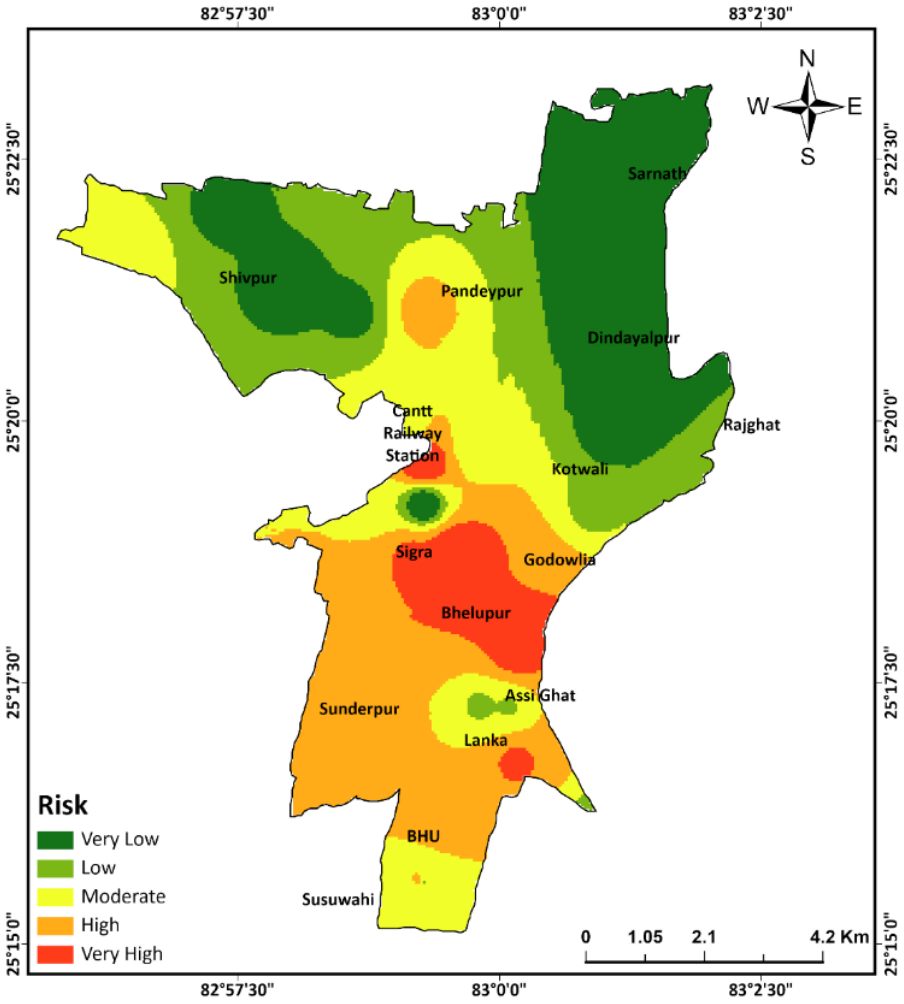

Figure 9. Risk map of Varanasi region for seismicity occurrence 2% probability of exceedance in 50 years

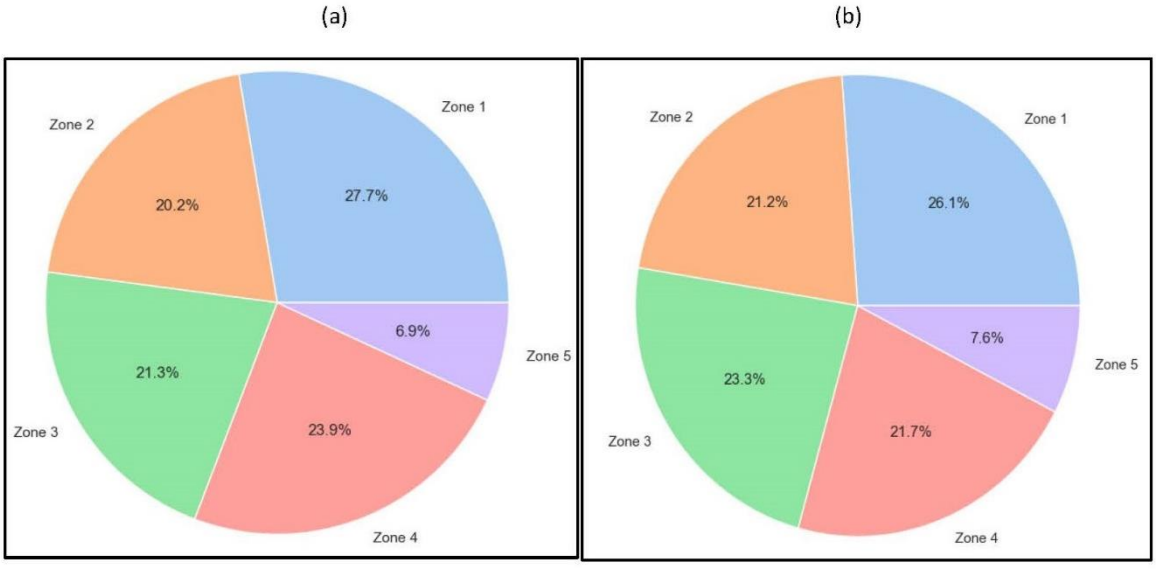

Figure 10. (a) Pie chart showing area coverage of risk levels by categorized zone for seismicity occurrence with a 10% probability of occurrence in 50 years. **(b)** Pie chart showing area coverage of risk levels by categorized zone for seismicity occurrence with a 2% probability of occurrence in 50 years.

Validation

The validation process ensured the robustness and reliability of the seismic risk assessment by triangulating the results with authoritative sources, empirical data, and on-site observations, as well as benchmarking against relevant research articles. The seismic hazard component was compared with the probabilistic seismic hazard assessment of Varanasi city by Nath et al. (2019), and the geological, geomorphological factors, and possible liquefaction hazard were cross-referenced with the regional study (Shukla and Raju, 2008; Prakash et al., 2016; Pandey et al., 2021; Shams et al., 2022; Singh, 2024; Tiwari et al., 2024) which showed that the central region of Varanasi city is more vulnerable to seismic risk, in comparasion to the northern and southern part of varanasi city. Additionally, extensive field visits corroborated the vulnerability assessment with on-site observations. The vulnerability assessment aligned closely with the study by Karunarathne and Lee (2020) and Ramli et al. (2023). The overall risk assessment methodology and AHP application were validated by comparing with similar studies in seismic-prone regions, such as Sitharam et al. (2013) in Lucknow, Jena et al. (2020) for Aceh Province in Indonesia, Bhochhibhoya and Maharjan (2022) in Nepal, ensuring consistency in the methodological approach and plausibility of results. All the above components and a detailed seismic microzonation study of Varanasi done by Singh (2022) were also taken into account for validation of the result, exhibiting coherence in hazard values and seismic zonation patterns.

CONCLUSIONS

The present study addressed the critical need for a comprehensive seismic risk assessment in Varanasi city by integrating the Analytic Hierarchy Process (AHP) with Geographic Information System (GIS). The research aimed to evaluate seismic risk by incorporating multiple factors, such as peak ground acceleration, geology, geomorphology, Vs30, population density, building density, literacy, and transportation. The AHP-GIS methodology produced a detailed probable seismic risk map, classifying Varanasi into five risk levels (very low to very high). Key findings reveal that 6.92% of the city's area falls under the very high seismic risk zone for a 10% probability of exceedance in 50 years, while 7.62% falls into the very high-risk zone for a 2% probability. These results highlight the urgent need for targeted mitigation strategies in high-risk areas to reduce vulnerability and enhance resilience. However, the study acknowledges certain limitations, including the dependence on the quality and availability of input data, the need for localization of the weighting scheme to better reflect region-specific conditions, and the necessity of continuous updates to the risk model due to the dynamic nature of urban development.

Acknowledgment

Major data for the analysis were collected from the website of Varanasi Development Authority, Geological Survey of India, International Seismological Centre, USGS Earth explorer, Google earth, Research Papers, Reports and Manual field surveys. We acknowledge the residents of Varanasi City for their cooperation and support during data collection and fieldwork.

Author Credit Statement

SS: Data collection, manuscript review and editing, AT: Conceptualization, modelling, data collection, manuscript writing; JLG: Manuscript writing, review and editing; GPS: Manuscript writing.

Data availability

Data can be made available on a reasonable request.

Compliance with Ethical Standards

The authors declare no conflict of interest and adhere to copyright norms.

References

Alizadeh, M., Ngah, I., Hashim, M., Pradhan, B. and Pour, A. B., 2018. A Hybrid Analytic Network Process and Artificial Neural Network (ANP-ANN) Model for Urban Earthquake Vulnerability Assessment. Remote Sens., 10(6), 975.

Anbazhagan, P., Thingbaijam, K.K.S., Nath, S.K., Narendara Kumar, J.N. and Sitharam, T.G., 2010. Multi-criteria seismic hazard evaluation for Bangalore city, India. J. Earth Sci., 38(5), 186–198.

Armaş, I., 2012. Multi-criteria vulnerability analysis to earthquake hazard of Bucharest, Romania. Nat. Hazards, 63, 1129–1156.

Ayalew, L., Yamagishi, H. and Ugawa, N., 2004. Landslide susceptibility mapping using GIS-based weightedlinear combination, the case in Tsugawa area of Agano River, Niigata Prefecture, Japan. Landslides, 1, 73–81.

Bhochhibhoya, S. and Maharjan, R., 2022. Integrated seismic risk assessment in Nepal. Nat. Hazards Earth Syst. Sci., 22(10), 3211-3230.

Bhukosh-GSI, 2023. Geological Survey of India, https://bhukosh.gsi.gov.in/Bhukosh/MapViewer.aspx.

Bilham, R., 2004. Earthquakes in India and the Himalaya: Tectonics, geodesy and history. Ann. Geophys., 47. 10.4401/ag-3338.

Census India, 2011. https://censusindia.gov.in/census.website/data/census-tables

CGWB, 2023. Central Ground Water Board., January 9. http://cgwb.gov.in

Ercanoglu, M. and Gokceoglu, C., 2004. Use of fuzzy relations to produce landslide susceptibility map of a landslide prone area (West Black Sea Region, Turkey). Eng. Geol., 75(3–4), 229–250.

ISC, 2023. International Seismological Centre, ISC-GEM Earthquake Catalogue, https://doi.org/10.31905/d808b825

Ishizaka, A. and Labib, A., 2011. Review of the main developments in the analytic hierarchy process. Expert Syst. Appl., 38(11), 14336-14345.

Ishizaka, A. and Nemery, P., 2014. Assigning machines to incomparable maintenance strategies with ELECTRE-SORT. Omega, 47, 45–59.

Jena, R., Pradhan, B., Beydoun, G., Nizamuddin, Ardiansyah, Sofyan, H. and Affan, M., 2020. Integrated model for earthquake risk assessment using neural network and analytic hierarchy process: Aceh province, Indonesia. Geosci. Front., 11(2), 613-634.

Jha, P. and Bajwa, S., 2023. Cultural tangibles and intangibles and disaster challenges: Narratives from Varanasi. In: Singh, A. (Ed.), International Handbook of Disaster Research. Springer, Singapore. https://doi.org/10.1007/978-981-19-8388-7_60

Kamp, U., Growley, B. J., Khattak, G. A. and Owen, L. A., 2008. GIS-based landslide susceptibility mapping for the 2005 Kashmir earthquake region. Geomorphology, 101(4), 631-642.

Karunarathne, A.Y. and Lee, G., 2020. Developing a multi-facet social vulnerability measure for flood disasters at the micro-level assessment. Int. J. Disaster Risk Reduct., 49. 101679. 10.1016/j.ijdrr.2020.101679.

Kramer, S.L., 1996. Geotechnical earthquake engineering. Prentice Hall, Upper Saddle River, New Jersey.

Lari, S., Frattini, P. and Crosta, G. B., 2009. Integration of natural and technological risks in Lombardy, Italy. Nat. Hazards Earth Syst. Sci., 9, 2085–2106.

Malik, J. N., Sahoo, S., Satuluri, S. and Okumura, K., 2015. Active fault and paleoseismic studies in Kangra valley: Evidence of surface rupture of a great Himalayan 1905 Kangra earthquake (Mw 7.8), northwest Himalaya, India. Bull. Seismol. Soc. Am., 105(5), 2325-2342.

Manna, F., Kennel, J. and Parker, B. L., 2022. Understanding mechanisms of recharge through fractured sandstone using high-frequency water-level-response data. Hydrogeol. J., 30, 1599–1618.

Martins, V. N., Sousa e Silva, D. and Cabral, P., 2012. Social vulnerability assessment to seismic risk using multicriteria analysis: the case study of Vila Franca do Campo. Nat. Hazards, 62, 385–404.

Mohanty, W., Walling, M., Nath, S. and Pal, I., 2007. First Order Seismic Microzonation of Delhi, India Using Geographic Information System (GIS). Nat. Hazards, 40, 245-260.

Napieralski, J., Barr, I., Kamp, U. and Kervyn, M., 2012. 3.8 Remote Sensing and GIScience in Geomorphological Mapping. Treatise on Geomorphology, 187-227. https://doi.org/10.1016/B978-0-12-374739-6.00050-6

Nath, S. K., 2017. Probabilistic Seismic Hazard Atlas of 40 Cities in India. Geoscience Division, Ministry of Earth Sciences, Government of India, New Delhi.

Nath, S. K., Raj, A., Sharma, J., Thingbaijam, K. K. S., Kumar, A., Nandy, D. R., Yadav, M. K., Dasgupta, S., Majumdar, K., Kayal, J. R. and Shukla, A. K., 2008. Site amplification, Qs, and source parameterization in Guwahati region from seismic and geotechnical analysis. Seismol. Res. Lett., 79(4), 526-539.

Nath, S.K., Adhikari, M.D., Maiti, S.K. and Ghatak C., 2019. Earthquake hazard potential of Indo-Gangetic Foredeep: its seismotectonism, hazard, and damage modeling for the cities of Patna, Lucknow, and Varanasi. J. Seismology, 23, 725–769.

Panahi, M., Rezaie, F. and Meshkani, S. A., 2014. Seismic vulnerability assessment of school buildings in Tehran city based on AHP and GIS. Nat. Hazards Earth Syst. Sci., 14, 969–979.

Pandey, M., Arora, A., Arabameri, A., Costache, R., Kumar, N., Mishra, V. N., Nguyen, H., Mishra, J., Siddiqui, M. A., Ray, Y., Soni, S. and Shukla, U. K., 2021. Flood susceptibility modeling in a subtropical humid low-relief alluvial plain environment: Application of novel ensemble machine learning approach. Front. Earth Sci., 9. https://doi.org/10.3389/feart.2021.659296

Prakash, K., Singh, S., and Shukla, U. K., 2016. Morphometric Changes of the Varuna River Basin, Varanasi District, Uttar Pradesh. J. Geomat., 10, 48-54.

Ramli, M. W. A., Alias, N. E., Mohd Yusof, H., Yusop, Z., Mat Taib, S., Abdul Wahab, Y. F. and Hassan, S. A., 2023. Spatial multidimensional vulnerability assessment index in urban area- A case study Selangor, Malaysia. Prog. Disaster Sci., 20, 100296. https://doi.org/10.1016/j.pdisas.2023.100296

Raschka, S. and Mirjalili, V., 2017. Python machine learning: Machine learning and deep learning with python. Scikit-Learn, and TensorFlow. Second edition ed, 3, 17.

Rashed, T. and Weeks, J., 2003. Assessing vulnerability to earthquake hazards through spatial multicriteria analysis of urban areas. Int. J. Geogr. Inf. Sci., 17(6), 547–576.

Rasool, Y., Agrawal, M., Shams, R., Ghosh, S. and Singh, D.K., 2024. Evaluation of Seismic Hazard for Northeastern Bihar (India): A Deterministic Approach. Indian Geotech J. https://doi.org/10.1007/s40098-024-01126-x

Sahu, S. and Saha, D., 2014. Geomorphologic, stratigraphic, and sedimentologic evidence of tectonic activity in Sone-Ganga alluvial tract in Middle Ganga Plain, India. J. Earth Syst. Sci., 123, 1335–1347.

Saaty, T.L., 1980. The Analytic Hierarchy Process: Planning, Priority Setting, Resources Allocation. Mcgraw-Hill, New York.

Saaty, T. L., 2008. Decision making with the analytic hierarchy process. Int. J. Serv. Sci., 1(1), 83–98.

Saaty, T. L., 2013. The modern science of multicriteria decision making and its practical applications: The AHP/ANP approach. Oper. Res., 61(5), 1101-1118.

Seeber, L. and Armbruster, J., 1984. Some elements of continental subduction along the Himalayan front. Tectonophys., 105(1–4), 263–278.

Shams, R., Agrawal, M. and Gupta, R.K., 2022. Probabilistic seismic hazard assessment of Kishanganj, Bihar, India. J Earth Syst. Sci., 131, 257

Shukla, U.K. and Raju, N.J., 2008. Migration of the Ganga river and its implication on hydro-geological potential of Varanasi area, U.P., India. J. Earth Syst. Sci., 117(4), 489-498.

Singh, M., 2024. Liquefaction hazard analysis of Varanasi city of Northern India. Nat. Hazards, 120, 1-21.

Singh, M., 2022. Seismic Microzonation Study of Varanasi City, PhD Thesis, Motilal Nehru National Institute of Technology, Allahabad].

Singh, M., Duggal, S. and Singh, V., 2020. A study to establish regression correlation between shear wave velocity and "N"-Value for Varanasi city, India. Proc. National Acad. Sci., India, Section A Physical Sciences, 91, 1-7.

Sitharam, T.G., Kumar, A. and Anbazhagan, P., 2013. Comprehensive seismic microzonation of Lucknow city with detailed geotechnical and deep site response studies. In Proc. Indian Geotech. Conf. December 22-24, Roorkee.

Tilara, C., Monika and Agrawal, M., 2024. Seismic hazard assessment of Mathura city (India): A deterministic approach. J. Earth Syst. Sci., 133, 209.

Tiwari, A., Rana, N. and Singh, G.P., 2024. A PGA amplification study for Varanasi city (India): Implications for seismic hazard assessment. J. Ind. Geophys. Union, 28(6), 417-429.

USGS., 2023, April 1. Earth Explorer. https://earthexplorer.usgs.gov/

VDA, 2022. Varanasi Development Authority, Official website. https://vdavns.com

Velasquez, M. and Hester, P. T., 2013. An Analysis of Multi-Criteria Decision Making Methods. Int. J. Oper. Res., 10(2).

Welle, T. and Birkmann, J., 2015. The World Risk Index – An Approach to Assess Risk and Vulnerability on a Global Scale. J. Extreme Events, 02(01), 1550003. https://doi.org/10.1142/s2345737615500037

Wisner, B., Blaikie, P., Cannon, T. and Davis, I., 2004. At Risk: Natural Hazards, People's Vulnerability and Disasters (2nd ed.). Routledge. https://doi.org/10.4324/9780203714775

Zebardast, E., 2013. Constructing a social vulnerability index to earthquake hazards using a hybrid factor analysis and analytic network process (F'ANP) model. Nat. Hazards, 65, 1331–1359.

Received on: 14-12-2024; Revised on: 22-04-2025 ; Accepted on: 21-05-2025

J. Ind. Geophys. Union, 29(4) (2025), 276-281
https://doi.org/10.71122/JIGU.29(4)2025.0026

Investigation of particulate matter in Perungudi, Chennai, Tamil Nadu (India) during the winter period

S. Tamil Selvi*[1] and S. Najma Nikkath[2]
[1] Department of Physics, KCG College of Technology, Chennai-600 097, Tamil Nadu, India
[2] Department of Physics, Bhaktavasalam Memorial College for Women, Chennai-600 080, Tamil Nadu, India
*Corresponding author: tssekar9773@gmail.com

ABSTRACT

Air pollution studies have found that the coarse and fine particulate matter are mainly responsible for various respiratory health effects for humans. This study focuses on the distribution and changes in the concentrations of PM_{10} and its precursors (SO_2, NO_2 and CO) in Perungudi, Chennai. Perungudi is chosen as the study area, as it is located on both commercial and residential site. The acquired data is used to estimate the various concentration levels of particulate pollution during the winter season of January and February 2022, using Pearson correlation and linear regression models .This statistical study helps in identify the significant relationship between the various pollutants SO_2, NO_2 and CO with PM_{10}. Pearson correlation and linear regression models were applied to evaluate the dependence of PM_{10} concentration on its precursors based on daily values. The correlation results indicated positive low and moderate values. The regression R^2 values show the variation of 20% to 25%. This study is an effective step toward a better understanding of PM_{10} changes in Perungudi under the changing influence of precursors.

Keywords: Particulate matter, Precursors, Perungudi, Chennai, Winter period, Pearson correlation, Regression

INTRODUCTION

The atmosphere is a blanket of air that surrounds the Earth. This is a mixture of gases that contains a huge number of solid and liquid particles (Lal, 2004). It is a source of essential gases, temperature, rain, air and protects from UV rays and meteors (Sharma, 2002). Air can be defined as combination of gaseous matter that forms the stratosphere or the invisible gaseous substances surrounding the Earth. Further, the local meteorological conditions can also influence the level of PM_{10} which include land surface temperature, precipitation and wind pressure (Zhang et al., 2015; Li et al., 2019; Faisal et al., 2022).

According to World Health Organization (WHO), one in eight total global deaths occurs as a result of exposure to air pollution. Over 3.5 million people die each year from outdoor air pollution. Low and middle-income countries, especially the Western Pacific and South-East Asian countries, account for about 88% of those premature deaths (WHO, 2012). Particulate matter which is often called as PM is a very fine proxy indicator for air pollution, strong evidence has been observed for the negative health impacts due to the exposure of this pollutant, whose components include sulphates, nitrates, ammonia, sodium chloride, black carbon, and water. The WHO has set thresholds on limits of key air pollutant to aid in the policies related to decision making process. 3,00,000 deaths would be saved worldwide annually with a PM concentration of around 35 $\mu g/m^3$.

These particulates in outdoor air pollution were recently designated as Group I carcinogen by the International Agency for Research on Cancer (Hamra et al., 2014). Many epidemiological studies have shown that particulates, especially inhalable particulates, are harmful to human health. In urban areas around the world, it is observed that on certain days, the atmospheric particulate matter is exposed to unhealthy concentrations. Therefore, using the Pearson's linear correlation coefficient, it was possible to analyze the interrelations between the occurrence of air pollution. The dust particle is mainly divided into different categories namely Suspended Particulate Matter (SPM), Respirable Suspended Particulate Matter (PM_{10} or RSPM), $PM_{2.5}$, PM_1 and ultrafine particles (Kushwaha et al., 2016). The classification and size of particles is given in Table 1.

Although the air quality at a specific site, depend on many factors, some common characteristics of changes could be determined using statistical methods. Therefore, in literature, the correlation coefficient is often used as a statistical tool to analyze the nature of changes in air pollution (Coyne and Bingham, 1977; Sonkin and Nikolaev, 1993; Karaca, 2012; Keresztes and Rapo, 2017)

Table 1. Classification and size of pollutant particles

Fraction	Size range
SPM	0.01-100μm in diameter
RSPM or PM_{10}	<=10μm diameter and diameter ranges from 2.5-10 μm is called coarse fraction.
Fine particles or $PM_{2.5}$	<=2.5 μm in diameter
PM_1	<=1 μm in diameter
Ultrafine particles (UFP)	<=0.1 μm in diameter

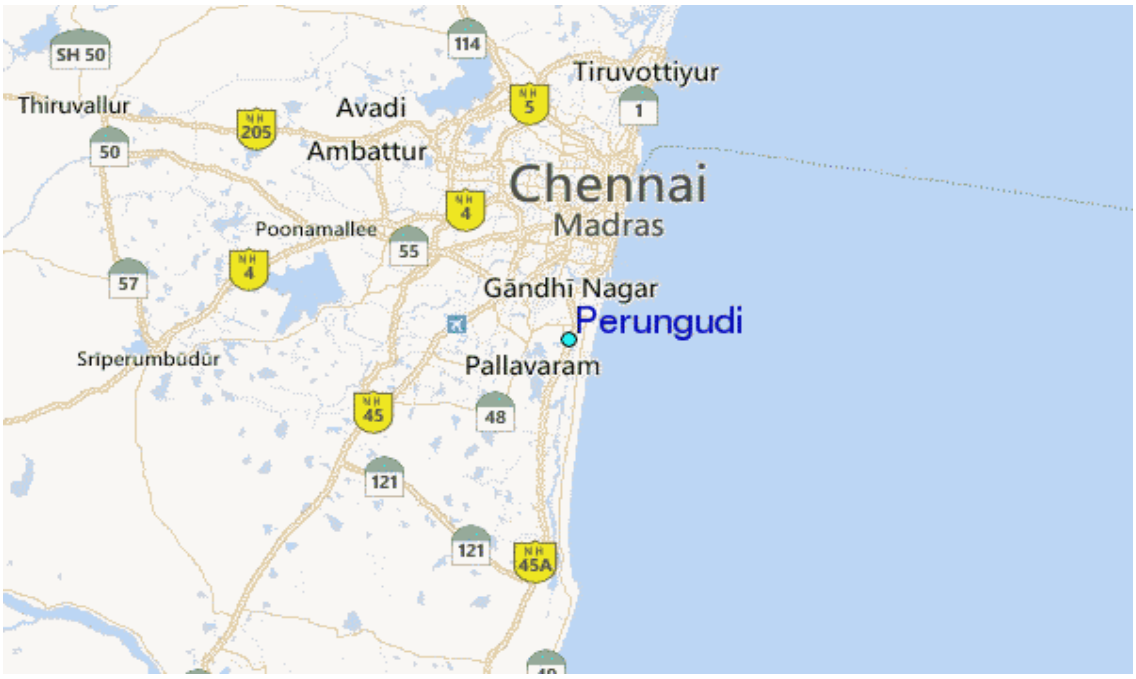

Figure 1. Study area of Perungudi in Chennai, located in Tamil Nadu (India)

DATA AND STUDY AREA

Perungudi is a neighbourhood of Chennai located in the state of Tamil Nadu (India), as shown in Figure 1. It is situated about 10 kilometres, south of Adyar. It is bordered on two sides by the Old Mahabalipuram Road and the Perungudi Lake. The PM_{10} data has been collected for Perungudi from the Tamil Nadu Pollution Control Board (TNPCB) website. TNPCB implements quality control measures for its data. It ensures data accuracy and all data is collected according to standards set by the Central Pollution Control Board (CPCB). Perungudi is chosen for study as it is one of the ambient air quality stations, and it is a residential cum commercial locality in the south Chennai area that is close to sea. Data chosen is for a monthly window from January 1, 2022 to February 28, 2022.

Perungudi is one of the fastest growing neighbourhoods in the Chennai city which is situated 10 km south of Adyar. This locality is a part of the eminent IT corridor and is been bordered by (OMR) Old Mahabalipuram road which is an expressway and it houses more than 60 top notch IT companies and several small-scale industries. It is being increasingly preferred as a residential place for software engineers. Perungudi has a lake which spreads over 50 acre of water body, once a major source for irrigation. Currently, it caters to the ever-growing water demand of the domestic needs and it helps in recharging ground water. When choosing variables to study air pollution, researchers typically select pollutants like particulate matter ($PM_{2.5}$, PM_{10}), nitrogen dioxide (NO_2), ozone (O_3), sulfur dioxide (SO_2), and carbon monoxide (CO) because they are well-established as significant contributors to health issues and have clear sources, allowing for targeted analysis of emission controls and mitigation strategies. The study of pollutants SO_2, NO_2 and CO with PM_{10} would give a better perspective of the concentration level and help in in both climatic and their health impacts .This study helps in modelling the future pollutants of Perungudi .

PEARSON'S CORRELATION COEFFICIENT

Testing the degree of correlation between two or more variables is one of the most important statistical procedures (Hashim et al., 2018). Pearson's linear correlation coefficient is used to analyse the dependencies between the presence of pollutants in the air, and various types of ailments and diseases occurring in the groups of the people exposed to these pollutants (Liu et al., 2016; Lee et al., 2017). By definition, this coefficient is used to determine the similarity of objects or variables and their linear interdependence (Thompson, 1984; Asuero et al., 2006). We also used Pearson correlation coefficient r, to measure the correlation between PM_{10} concentration and other air pollutants (Jafri et al., 2022). It can range from +1 to -1. A value of 0 indicates that there is no association between the two variables. A value greater than 0 indicates a positive association; that is, as the value of one variable increases, so does the value of the other variable. A value less than 0 indicates a negative association; that is, as the value of one variable increases, the value of the other variable decreases.

The Pearson's correlation coefficient (r) can be expressed as,

$$r = [n(\Sigma xy) - \Sigma x \Sigma y]/\sqrt{[n(\Sigma x^2) - (\Sigma x)^2][n(\Sigma y^2) - (\Sigma y)^2]}$$

Where, x is the independent variable, y is the dependent variable, n is the sample size, and Σ represents a summation of all values. Correlation analysis cannot be interpreted as establishing cause-and-effect relationships. It can indicate only how or to what extent variables are associated with each other. The correlation coefficient measures only the degree of linear association between two variables.

Interpretation of the calculated coefficient depends on its value. The stronger are the interdependencies between variables, the higher is the coefficient. Therefore, specific ranges of the coefficient are determined, depending on the field of knowledge, to describe the strength of the interdependencies (Akoglu, 2018). In this analysis, the interpretation of the R coefficient was adopted as per Table 2.

COEFFICIENT OF DETERMINATION

Linear regression is a powerful tool for predicting future events. It calculates an equation that minimizes the distance between the fitted line and all of the data points. R squared or R^2, coefficient of determination is a statistical measure that gives information about the plotted regression line that fits the actual data. R^2 measures the amount of variation between the actual and predicted values in the regression model. R^2 values range from 0 to 1 expressed as a percentage from 0% to 100%. The higher R^2 value shows the better regression line fitting to the data. If the value is close to 0, then the regression model is not a good fit. R^2 is used to find whether the independent and dependent variables have linear relationship between them.

RESULTS AND DISCUSSION

We discuss the correlation results of PM_{10} with its precursor pollutants. PM_{10} with NO_2, SO_2 and CO are not highly correlated in the studied Perungudi region. They show mostly low or moderate correlation. But all are positively correlated. When PM_{10} increases, other pollutants NO_2, SO_2 and CO also increases and vice versa. The correlation values are tabulated in the Table 3.

The time series plot of PM_{10} clearly shows that there is a variation in pollution for every day (Figure 2). Although, it is not consistent, there is a positive correlation between PM_{10} and other pollutants.

In our study, R^2 value for SO_2, NO_2 and CO are almost the same, ranging between 20% to 25% (Figures 3, 4 and 5). Since the correlation is low and moderate, R^2 values are less. The variation between the actual and predicted values are more in this region. It should be continuously monitored as other pollutants also begins to increase or decrease depends on PM_{10} level. If there is an increase in NO_2, SO_2 and CO levels, the severity of health issues also will raise in Perungudi region.

Exposure of NO_2 is known to cause adverse health effects on the respiratory system. Short term exposure is associated with an increased risk of death, both cardiovascular and respiratory system. Long term exposure contributes to the development of asthma, increase in respiratory infections and chronic lung diseases. NO_2 is also responsible for the formation of nitrate aerosols which cause haze and reduce visibility. This is called smog formation which is a pollution cloud. The highest concentrations of NO_2 are found in road traffic. Sulphur dioxide emissions are also known to be the precursor of sulphate aerosol, which is a key player in Earth's energy balance. Sulphate aerosols are considered to act as cloud condensation nuclei, favoring cloud formation. This reduces the amount of solar radiation that reaches the surface. Exposure to SO_2 produces impairment of respiratory function, asthma and also chronic obstructive pulmonary disease (COPD). Cardiovascular diseases are also produced due to long exposure. (Tran et al., 2020). Similarly, exposure to CO causes fatigue, chest pain, impaired vision, reduced brain function. The adverse health effects at low concentrations are impacts on cardiovascular and neurobehavioral processes and at high concentrations, it leads to unconsciousness or death (Raub et al., 2000).

Table 2. Interpretation of (r) linear correlation coefficient

0.90–1.00	Very high correlation
0.70–0.89	High correlation
0.50–0.69	Moderate correlation
0.30–0.49	Low correlation
0.00–0.29	Little correlation, if any

Table 3. Correlation values of PM_{10} with its precursors in Perungudi region, Chennai

	PM_{10}	NO_2	SO_2	CO
PM_{10}	1	0.457	0.473	0.506
NO_2	0.457	1	0.379	0.547
SO_2	0.473	0.379	1	0.481
CO	0.506	0.547	0.481	1

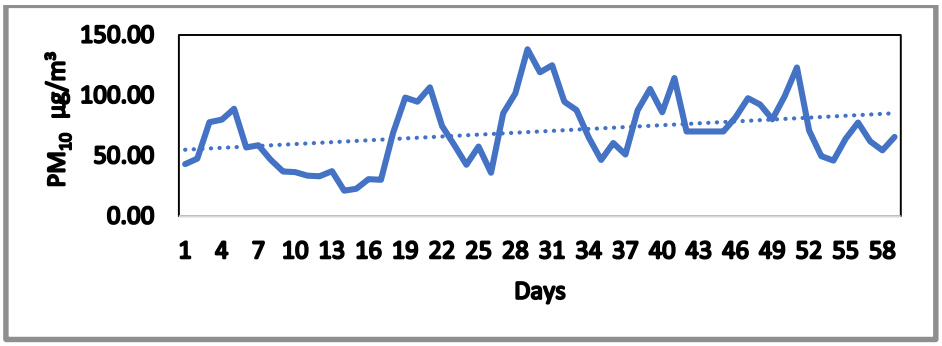

Figure 2. Time series plot of PM_{10} for Perungudi, Chennai (India)

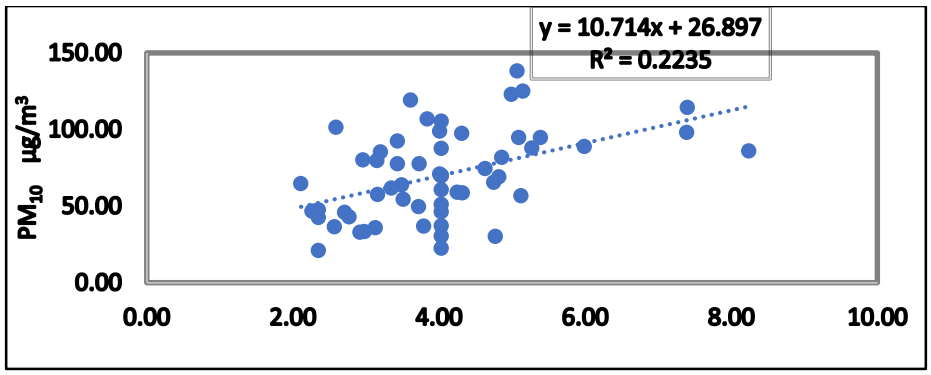

Figure 3. Regression plot of PM_{10} with SO_2 for Perungudi, Chennai (India)

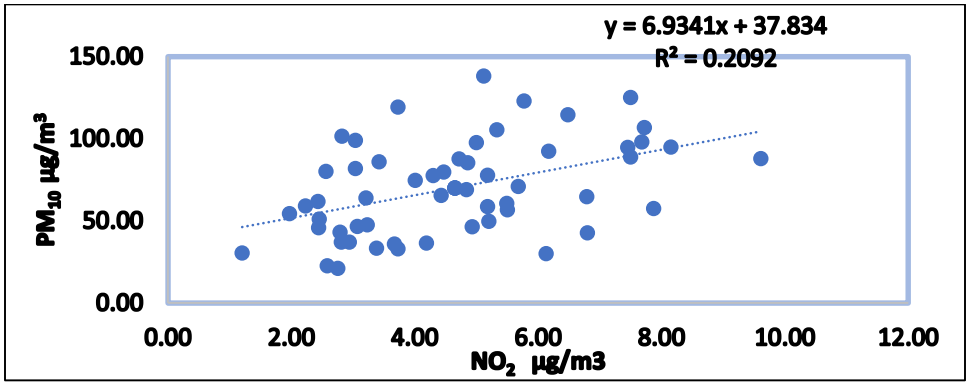

Figure 4. Regression plot of PM_{10} with NO_2 for Perungudi, Chennai (India)

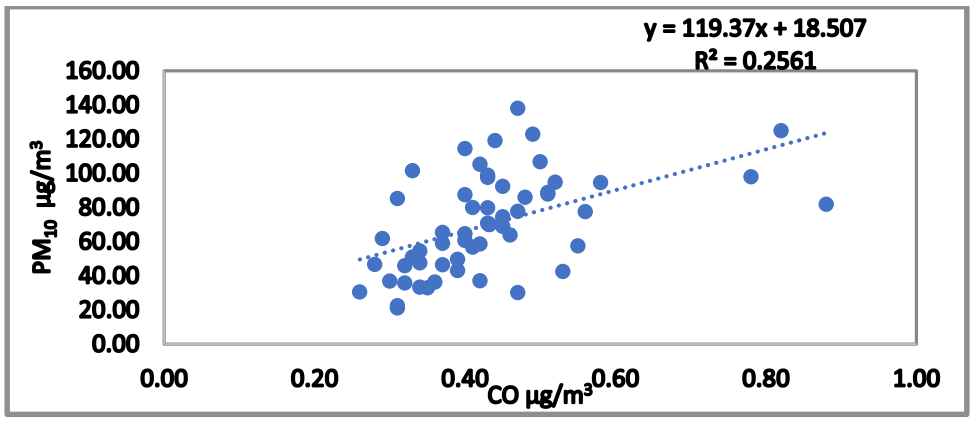

Figure 5. Regression plot of PM_{10} with CO for Perungudi, Chennai (India)

CONCLUSIONS

There is a positive correlation between PM_{10} and other gaseous pollutants like SO_2, NO_2 and CO which suggests that these gases also contribute to the formation of fine sulfate and nitrate particles as part of the PM_{10} concentration in the atmosphere. PM_{10} concentration is found to be less significant in Perungudi, as the linear relationship between them implies that the fraction of the variance (R^2) lies within 25%. The low R^2 suggests that the investigation of other variables contributing to the variability of pollutants at the site should be considered simultaneously. However, it should be remembered, that the correlation coefficients do not always prove the existence (or absence) of dependencies between the analyzed variables (Sharma, 2005), but may indicate the possible occurrence of such interdependencies. Therefore, it should be investigated if the significant impact to this phenomenon was related to similar weather conditions. Visual aids such as scatter plots or heatmaps could be added in future to enhance this type of work. This study is a part of broader research initiative focused on the study of mitigating pollutants, implementing climate friendly policies in urban planning such as energy-efficient housing, greener cities, shifting to cleaner modes of energy, low emission vehicles, use of free power sources, cleaner technology to reduce industrial emissions, and finally the municipal waste management that can control air pollution in Perungudi .

ACKNOWLEDGMENTS

The authors are thankful to the reviewers who have given critical and valuable suggestions to improve the manuscript to the present form. The authors express sincere thanks to Dr. O.P. Pandey, Chief Editor, JIGU for continuous involvement, encouragement and provided an opportunity to publish this research in the journal.

Author Credit Statement

S.Tamil Selvi: Conceptualization, methodology, formal analysis and writing (original draft and edits). S. Najma Nikkath: Conceptualization, methodology and writing (original draft and edits).

Data Availability

All data used in this study are available at the Tamil Nadu Pollution Control Board website.

Compliance with Ethical Standards

The authors declare that they have no conflict of interest and adhere to copyright norms.

REFERENCES

Akoglu, H., 2018. User's guide to correlation coefficients. Turkish J. Emergency Medicine, 18, 91–93.

Asuero, A.G., Sayago, A. and Gonzalez, A.G., 2006. The correlation coefficient: an overview. Crit. Rev. Anal. Chem., 36 , 41−59.

Coyne, P.I. and Bingham, G.E., 1977. Carbon Dioxide Correlation with Oxidant Air Pollution in the San Bernardino Mountains of California. J. Air Pollut. Control Assoc. 27, 782-784.

Faisal, A.A., Kafy, M.A., Fattah, A., Dewan, M., Jahir, A., Rakib,A.A., Rahaman,Z.A., Ferdousi,J. and Huang, X., 2022. Assessment of temporal shifting of $PM_{2.5}$, lockdown effect, and influences of seasonal meteorological factors over the fastest-growing megacity, Dhaka. Spat. Inf. Res., 30 (3), 441-453.

Hamra, G B., Guha, N., Cohen, A. et al., 2014. Outdoor particulate matter exposure and lung cancer: a systematic review and metaanalysis. Environmental Health Perspectives, 122(9).

Hashim, N.I.M., Noor, N.M. and Yusof, S.Y., 2018. Temporal characterisation of ground-level ozone concentration in Klang Valley. In E3S web of conferences 34, 02047. EDP sciences.

Jafri, M., Noor, N., Rahim, N.A. A. A., Baidrulhisham, S.E., Ramli, N., Saufie, A.Z and Deak, G., 2022. Modified linear regression for predicting ambient particulate pollutants (PM10) during High Particulate Event. Earth and Environmental Science, 1216, 012002.

Karaca, F., 2012. Determination of air quality zones in Turkey. J. Air Waste Manage, 62, 408-419.

Keresztes, R. and Rapo, E., 2017. Statistical analysis of air pollution with specific regard to factor analysis in the Ciuc basin, Romania. Studia Ubb Chemia, 3 , 283-292.

Kushwaha, K., Sham Sundar, K.M. and Karthikeyan, S., 2016. Assessment of Heavy Metals From Respirable Suspended Particulate Matter (PM10) in Thiruvottiyur, Chennai, India. Int. Res. J. Engin. and Technology, 3(8), 796-802.

Lal, D.S., 2004. Climatology, Publisher Sharda Pustak Bhandar, ISBN 81-86204- 12-1.

Lee, C.F., Hsiao, J., Cheng, S.J. and Hsieh, H.H., 2017. Identification of regional air pollution characteristic and the correlation with public health in Taiwan. Int. J. Environ. Res. Public Health, 4 , 106-110.

Li, X., Song, H., Zhai,S., Siqi,L., Kong,Y., Xia, H. and Zhao, H., 2019. Particulate matter pollution in Chinese cities: areal-temporal variations and their relationships with meteorological conditions (2015–2017). Environ. Pollut., 246, 11-18.

Liu, X., Liang, Y. and Yuan, D, 2016. Relationship between Air Polllution Index (API) and Crowd Health in Nanchang City. J. Geosci Environ. Protect, 4, 26−31.

Raub, J.A., Mathieu-Nolf, M., Hampson, N.B. and Thom, S.R., 2000. Carbon monoxide poisoning-A public health perspective. Toxicology, 145;1-14.

Sharma, A.K., 2005. Text book of correlation and regression, Discovery Publishing House, New Delhi.

Sharma, P.D; 2002. Ecology and Environment, Publisher Rastogi publications.

Sonkin, L.R. and Nikolaev, V.D, 1993. Synoptic analysis and atmospheric pollution forecast. Russian Meteorology & Hydrology, 5, 10-14.

Thompson, B., 1984. Canonical correlation analysis – Uses and Interpretation, Sage Publications, London.

Tran, V.V., Park, D., and Lee, Y.C., 2020. Indoor Air pollution, related human diseases and recent trends in the control and improvement of indoor air quality. Int. J. Environ. Res. Public Health, 17(8), 2927.

WHO, 2012. World Health Organization. Burden of disease from ambient air pollution for Geneva, Public Health, Social and Environmental Determinants of Health Department, World Health Organization, Available from: http://www.who.int/phe/health_topics/outdoorair/databases/AAP_BoD_results_March2014.pdf?ua=1

Zhang, B., Xie, G., Li, N. and Wang, S., 2015. Effect of urban green space changes on the role of rainwater runoff reduction in Beijing, China. Landsc. Urban Plan., 140, 8-16.

Received on: 08-08-2024; Revised on: 02-04-2025 ; Accepted on: 16-04-2025

J. Ind. Geophys. Union, 29(4) (2025), 282-292
https://doi.org/10.71122/JIGU.29(4)2025.0027

Student Section

Possible extension of Proterozoic sediments beneath Eastern Ghats Belt: A case study of Bastar Craton

Ankita Roy[1], Swarnapriya Chowdari[2] and A. Vasanthi [2]*
[1]Department of Earth Sciences, Pondicherry University, Puducherry-605014, India
[2]CSIR-National Geophysical Research Institute, Hyderabad-500007, India
*Corresponding author: vasanthi99ngri@gmail.com

ABSTRACT

The eastern margin of the Indian shield presents a geologically and geotectonically intricate zone where Proterozoic sedimentary basins and the high-grade metamorphic Eastern Ghats Belt (EGB), are juxtaposed along a broad, shear-dominated contact stretching from Odisha in the north to northern Tamil Nadu in the south. The tectonic relationship between the Bastar craton and the Eastern Ghats Belt in eastern India, has been the subject of considerable geological interest due to its implications for Proterozoic crustal evolution, basin development, and the assembly of ancient continental blocks. In this study, satellite-derived gravity data over Bastar craton and adjoining regions have been analysed to explore the possible extension of Proterozoic sedimentary sequences of this craton beneath EGB. The presence of a prominent residual gravity low of the order of -50 mGal on the SE part of the study area has been delineated below the EGB terrain, indicating possible presence of Mesoproterozoic to early Neoproterozoic sedimentary sequences. Further, gravity modelling across the Bastar craton and EGB, reveals steep crustal-scale contacts and high-density zones that are consistent with a under-thrust geometry. The underthrusting of Bastar sediments beneath the EGB likely occurred during the Mesoproterozoic collisional events, linked to the Rodinia supercontinent assembly. These findings not only enhance our understanding of the tectono-thermal history of the Bastar craton and EGB interface, but also provide a framework for re-evaluating crustal accretion processes along the cratonic margins in the Indian shield.

Key Words: Proterozoic sediments, Eastern Ghats Belt (EGB), Satellite gravity, Finite Element Method, Bastar craton, Bastar-EGB interface

INTRODUCTION

The Indian peninsular shield predominantly comprises Precambrian crustal blocks that formed approximately 3.6 to 2.6 billion years ago during the Archean Eon, representing some of the earliest solidified portions of the Earth's lithosphere (Sarkar et al., 1990; Sharma, 2010). These stable crustal blocks, commonly known as cratons, form the foundational cores of continental plates and are the key to understanding early Earth processes (Smithies et al., 2009). The tectonic framework of the Indian shield is well characterized by five major cratons, the Aravalli, Bundelkhand, Singhbhum, Bastar, and Dharwar, each exhibiting distinct geological histories and tectono-thermal events (Naqvi and Rogers, 1987; Ramakrishnan and Vaidyanadhan, 2010) (Figure 1). These Archean cratonic blocks are bounded and separated by various Proterozoic mobile belts, rift zones, grabens, and the shear zones, reflecting a complex and prolonged tectonic evolution marked by episodic collisions, accretions, and crustal reworking (Meert, 2003).

This study principally focuses on the Bastar craton, a significant Archean cratonic block situated in central India, renowned for its preserved ancient crust and tectono-thermal history that provide invaluable insights into the geodynamic evolution of the Indian Shield (Asokan et al., 2020; Mohanty, 2021), which in turn has implications for global tectonics, including supercontinent cycles such as Columbia and Rodinia (Satpathi et al., 2022). However, the intricate and heterogeneous litho-tectonic configuration within the Bastar region, characterized by a mosaic of metavolcanic, metasedimentary and granitic units, renders lithological correlations speculative and complex.

Multiple geological and geophysical investigations have been conducted to unravel the crustal and lithospheric architecture of the Bastar craton. Seismic wave dispersion studies reveal a lithospheric thickness of approximately 140 km beneath this region (Mitra et al., 2006). Complementary seismological analyses estimate the crustal thickness of Bastar craton to be in the range of 35–40 km, consistent with the other ancient continental crusts worldwide (Jagadeesh and Rai, 2008). Heat flow measurements carried out by Gupta et al. (1993) have documented relatively high surface heat flow in Bastar craton compared to the Dharwar craton, which has been attributed to spatial variations in upper crustal radiogenic heat production and possibly localized tectono-thermal activity.

In addition, several studies were also carried out to understand the tectonic relationship between the Bastar craton and the Eastern Ghats Belt (EGB) in eastern India. The southeastern margin of the Bastar craton is structurally juxtaposed against the high-grade Proterozoic EGB, forming a tectonically complex and thermally contrasting boundary in eastern Peninsular India. Proterozoic sedimentary basins, such as the Chhattisgarh Supergroup (~1.4–1.0 Ga), Khariar, Indravati, Sabari, Abujhmar and Amphani groups, lie along the Bastar craton's fringe and are interpreted as rift-related intra-basinal sequences. Gravity studies highlight the presence of tectonically active contact between Bastar craton and the EGB (Subramanyam and Verma, 1986; Kumar et al., 2004; Valdiya, 2015). Moreover, thermal (Bhadra et al., 2004), geochemical and geochronological studies have identified successive mafic magmatic events that have profoundly reshaped the lithosphere of the Bastar craton, evidencing sustained crust-mantle interactions that may have influenced its present-day geodynamic character (Rao et al., 2023).

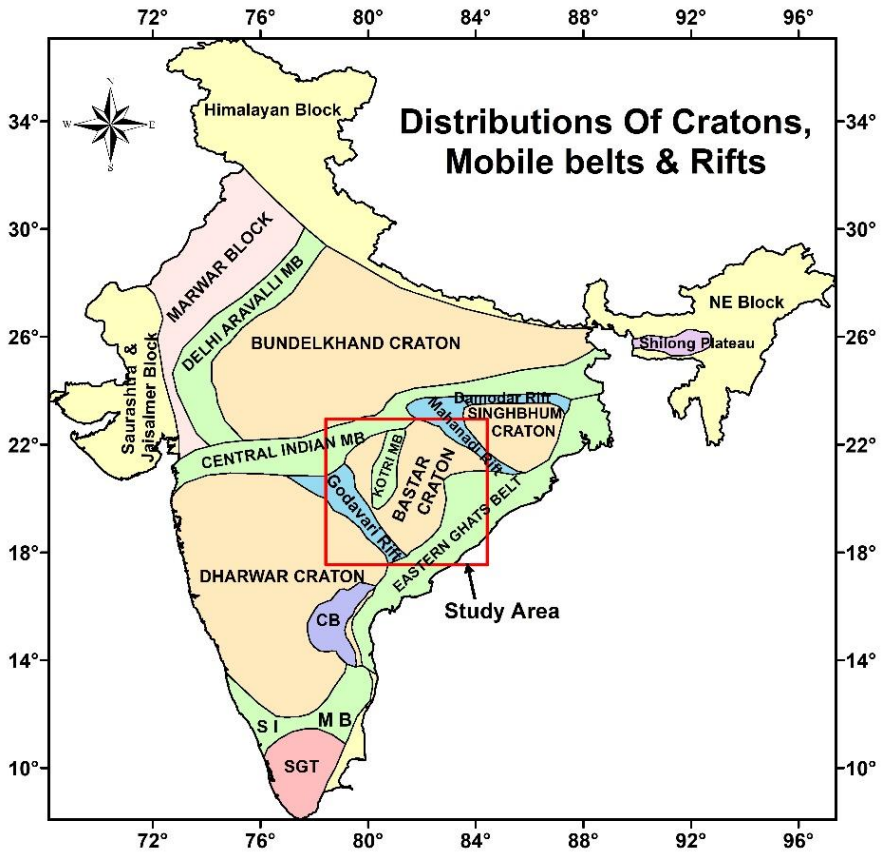

Figure 1. Distribution of cratons and mobile belts in India. Location of present study area is shown by red colour box (modified after Chowdari, 2019). CB: Cuddapah basin, SIMB: South India Mobile Belt, SGT: Southern Granulite Terrain.

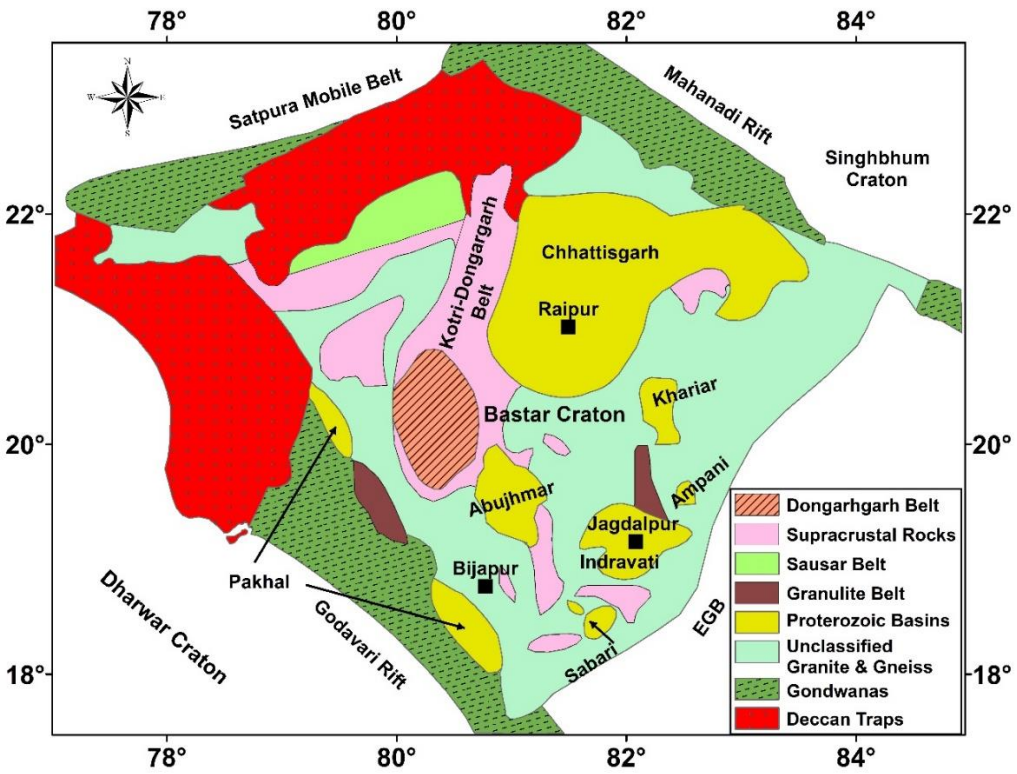

Figure 2. Generalized geology and tectonic boundaries of Bastar craton (modified after Santosh et al., 2020).

In the present study, gravity data derived from a Global Gravity Model (Zingerle et al., 2020) over the Bastar craton and its adjoining regions, are analyzed to delineate the subsurface tectonic framework, and to check the possibility of extension of Proterozoic sediments beneath the EGB. The application of edge enhancement techniques enables detailed delineation of faults, lineaments, and tectonic boundaries that are otherwise challenging to resolve. Additionally, 2.5D gravity modeling along a NW-SE profile, cutting across the Eastern Ghats Belt and Bastar craton, is employed to further constrain the crustal and lithospheric configuration.

GEOLOGY AND STRUCTURAL FRAMEWORK

Bastar craton, displaying a broadly trapezoidal configuration (Mohanty, 2021), lies within 17°30′ N - 23°30′ N and 77° 48′ E – 84°06′ E. This craton is confined by mobile belts and rift zones from all sides, Godavari rift zone in the south-western part and Mahanadi rift in north-east. The south-eastern part of this craton is marked by Eastern Ghats Belt (Biswal et al., 2001). The Central India Tectonic Zone, Son-Narmada lineament, and the Satpura Mobile belt, forms the boundary close to north-western part of the craton (Bandyopadhyay, 1995). The major geological formations in this region are tonalite- trondhjeamite- granodiorite (TTG)- rich gneissic basement complex, enclaves of high grade supracrustal rocks forming the granulitic belts, intra cratonic Kotri-Dongarhgarh mobile belt, and Proterozoic Purana basins (Ramakrishnan and Vaidyanadhan, 2010) (Figure 2). The initial crustal growth phase in the craton took place during Paleoarchean period (Sarkar et al.,1993).

This craton hosts several intra-cratonic Proterozoic sedimentary basins among which, Chhattisgarh Basin (Deb, 2004) is the largest. Other small basins include Indravati, Ampani, Abujhmar, Khariar, Sabari and Pakhal. The complex geology of Bastar craton reflects a long tectonic history which not only shapes the surface geology, but also influenced the underlying deep crustal processes. Among the major supracrustal/volcanic sequences, the Kotri-Dongargarh Supergroup is mainly composed of the Amagaon, Nandagon and Khairagarh groups of rocks. The Amagon group, composed of granites and gneisses with subordinate schists and quartzites, is considered to have been formed at around 2.3 Ga (Naqvi and Rogers, 1987). The Nandgaon Group incorporates the Bijli and Pitapani volcanic suites, which are dominated by rhyolites and subordinate dacites and andesites, with the rhyolite dated at 2503 to 2180 Ma (Sarkar et al., 1993). This terrain also hosts several deformed alkaline complexes along the suture with the Eastern Ghats Belt, including the Mesoproterozoic (1480 Ma) Khariar alkaline complex. The Southern portion of Bastar craton exhibits several episodes of mafic magmatism, as evidenced by the presence of several mafic dyke swarms (Srivastava et al., 2021; Rao et al., 2023).

REGIONAL TOPOGRAPHY

The overall topography of this region (Figure 3) is rugged as it is integrally linked with mobile belts, rift zones and low-lying Proterozoic basinal structures. The elevation varies from as low as 150 m for low lying areas to more than 900 m for upland regions. For example, Eastern Ghats Belt along the south eastern part of the craton, is a structurally upland region, with high elevation of around 900 meter (Valdiya, 2015). In contrast, the intra-cratonic depressions, including Chhattisgarh, Indravati, Sabari, Ampani, Abujhmar, Khariar, collectively form the significant low relief topographic feature. The regions uneven topography is further emphasized by the presence of localized tectonic belt. Kotri-Dongargarh mobile belt is one such tectonic feature, extending ~ 250 km in length, with 50 km wide range from north-south to NNE-SSW direction (Chakraborty and Debnath, 2023). The structurally uplifted nature of the belt, resulted into localized topography high (Ramakrishnan and Vaidyanadhan, 2010).

GRAVITY STUDY

For the present study, the gravity data of the Bastar craton and its adjoining regions have been derived from XGM2019e_2159 global gravity field model, which offers a harmonized and high resolution representation of Earth's gravity field (Zingerle et al., 2020). Figure 4 depicts the Bouguer anomaly map of the studied region, where the anomalies range from -95 mGal to +75 mGal. All the basins of the craton are clearly brought-out with prominent gravity lows, while different high-grade rocks are well reflected by gravity highs.

In general, the observed Bouguer gravity anomaly reflects contribution from both deeper (regional) and shallower (residual) sources, and it is thus important to remove the broader regional trend, which in turn brings out various geological structural features very clearly. In this study, Finite Element Method (FEM) (Mallick et al., 2012; Vasanthi and Santosh, 2021a, b) has been used to compute the regional gravity component, which has been subsequently removed from observed Bouguer gravity anomaly to obtain the residual gravity anomaly map.

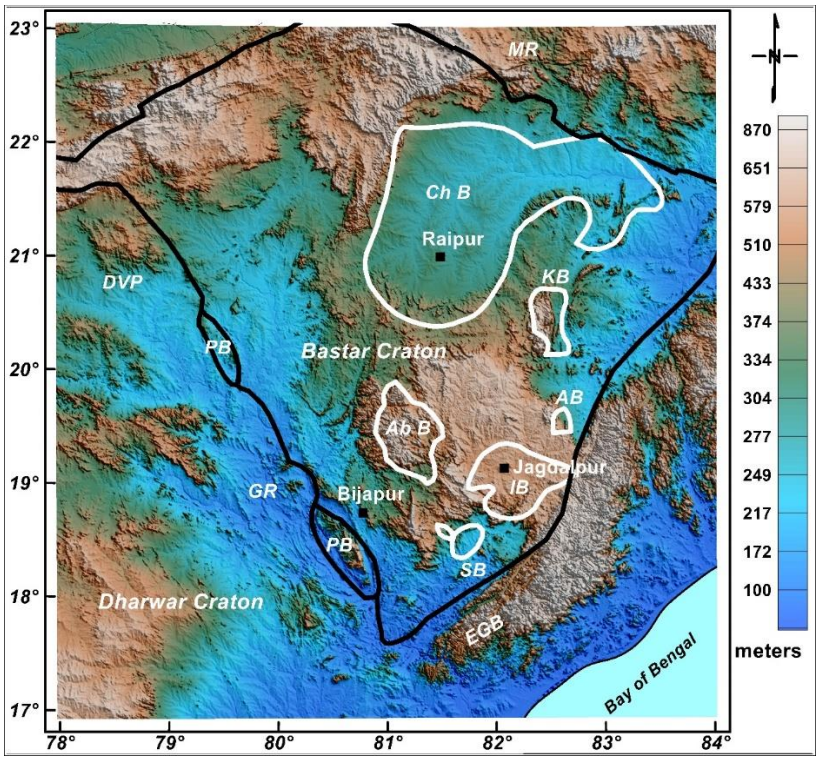

Figure 3. Topographic map of the study region obtained from the Shuttle Radar Topography Mission (SRTM) (ftp://edcsgs9.cr.usgs.gov/pub/data/srtm). Bold black line denotes the boundary of the Bastar craton, and white solid line represents the basin boundaries. Ch B: Chhattisgarh Basin, KB: Khariar Basin, AB: Ampani Basin, IB: Indravati Basin, SB: Sabari Basin, PB: Pakhal Basin, MR: Mahanadi Rift, GR: Godavari Rift, EGB: Eastern Ghats Belt.

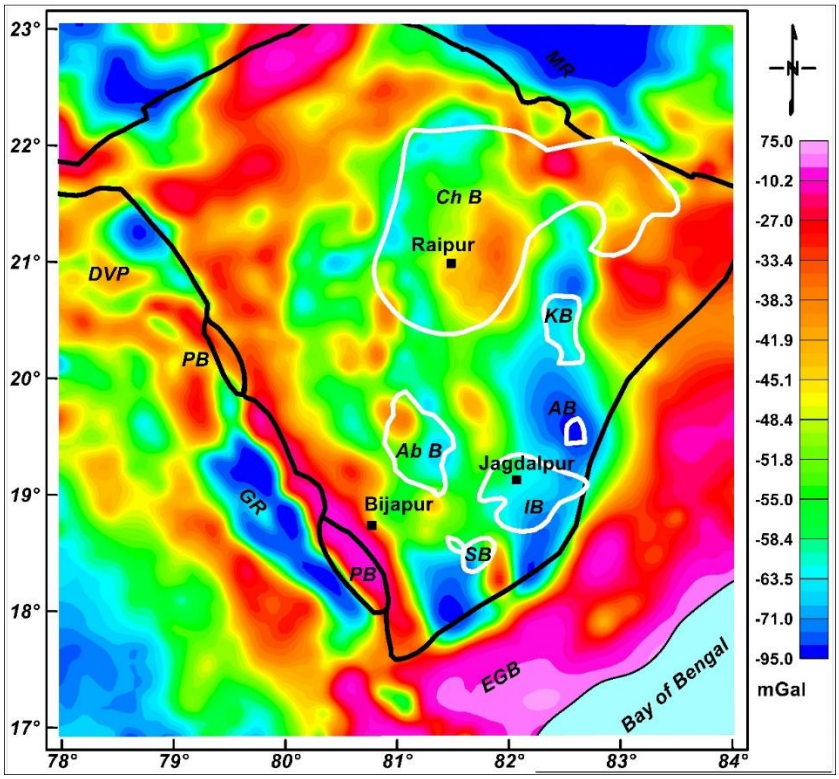

Figure 4. Bouguer gravity anomaly map of the Bastar craton and its surrounding regions. Bold black line denotes the boundary of the Bastar craton, and white solid line represents the basinal boundaries. Ch B: Chhattisgarh Basin, KB: Khariar Basin, AB: Ampani Basin, IB: Indravati Basin, SB: Sabari Basin, PB: Pakhal Basin, MR: Mahanadi Rift, GR: Godavari Rift, EGB: Eastern Ghats Belt.

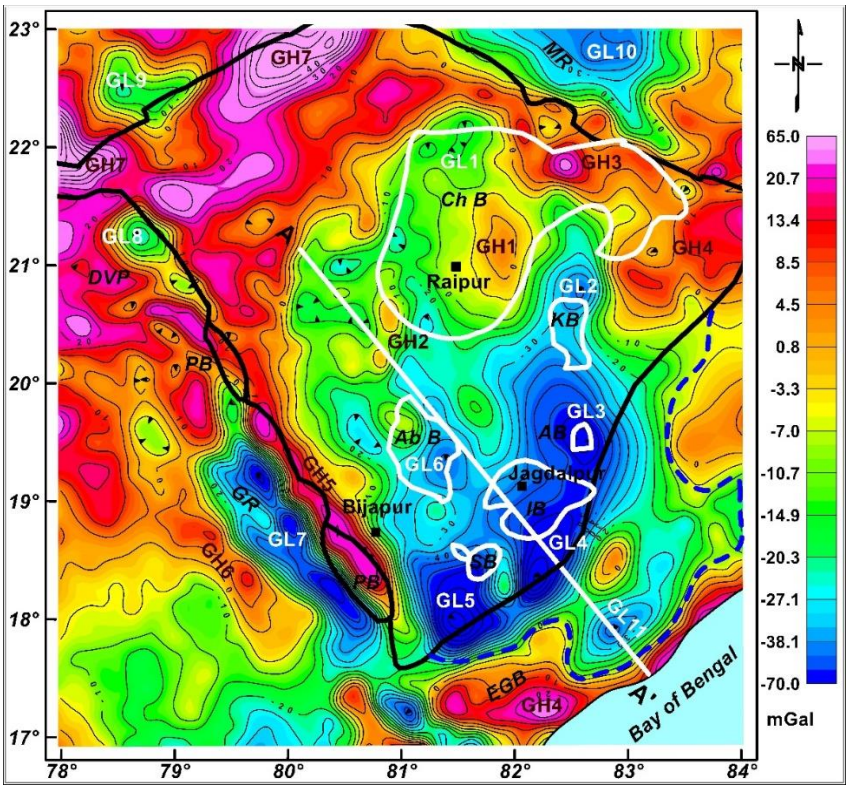

Figure 5. Residual gravity anomaly map, derived by Finite Element Method, covering Bastar craton and adjacent region highlighting key structural features. GL1-GL11 represent the prominent gravity lows, while GH1-GH7 gravity high zones. Bold black line denotes the boundary of the Bastar craton, and white solid line represents the basin boundaries. NW-SE profile AA', is marked, along which 2.5D gravity modelling has been carried out. MR: Mahanadi Rift, GR: Godavari Rift, EGB: Eastern Ghats Belt.

The resultant residual gravity anomaly map is shown in Figure 5. It is interesting to observe that the boundaries of various litho-tectonic units are brought out very clearly. The central and northern parts of the Bastar craton are mostly associated with isoloated gravity highs (GH1, GH2 and GH3) corresponding to un-classified metamorphic rocks (Figure 2) concealed below the sedimentary succession. A notable gravity high (GH4) in south-eastern and eastern part of the study area aligns with the Eastern Ghats Belt (EGB). The Bhoopalapatnam and Karimnagar granulitic belts, which are situated on either side of the Godavari Rift (GR) basin, are characterized by conspicuous gravity highs (GH5 and GH6 respectively). Similarly, the high-order gravity anomaly (GH7) on the NW part of the study region reflects the Deccan Trap cover.

The basins of the craton, such as Chhattisghar (Ch B), Khariar (KB), Indravati (IB), Ampani (AB), Sabari (SB) and Abujhmar (Ab B), correspond to gravity low anomalies (GL1, GL2, GL3, GL4, GL5 and GL6 respectively). However, over the Pakhal Basin (PB), we observe a gravity high anomaly, as the high-density Bhopalpatnam granulitic rocks are in contact with the sedimentary succession. A prominent gravity low (GL7) located in south-western part of study area is sandwiched between the conspicuous gravity high GH5 and GH6 . This prominent gravity low zone corresponds to the Gondwana sedimentary rock accumulation in the Godavari Rift Basin (Vasanthi, 2025). Similarly, Gondwana sediments of Wardha sub-basin and Satpura sequence are associated with gravity lows GL8 and GL9 respectively. Similarly, a notable gravity low (GL10) corresponds to Mahanadi Gondwana sediments.

An interesting finding of the present study has been the delineation of gravity highs (GH1 and GH3) in Chhattisgarh Basin, which contrasts with the usual gravity low association with sedimentary basins. This positive bias might be explained by the geological influence of adjacent Kotri-Dongarhgarh mobile belt. Geological mapping of the craton (Figure 2) shows that the Kotri-Dongarhgarh orogenic supracrustal rocks occurs along the Chhattisgarh basins eastern edge, even though the orogen trends north to south. Therefore, the present study reveals the continuation of the Kotri-Dongarhgarh belt beneath the Chhattisghar Basin.

As discussed earlier, the cluster of gravity lows (GL2 to GL6) characterizing the SE portion of the craton due to the presence of number of basins like Khariar (KB), Ampani (AB), Indravati (IB), Sabari (SB) and Abujhmar (Ab B). It is important to note that this low anomaly stretches beyond the mapped boundary

of the craton, towards EGB. Despite the high grade metamorphic nature of this terrain, the persistence of this gravity low (as marked by blue dotted line; GL11) raises the possibility of under-thrusting of Bastar sediments beneath EGB.

EDGE ENHANCEMENT TECHNIQUES

Precise imaging of crustal architecture plays important role in tectonic reconstruction and resource exploration. The Bouguer anomaly map or residual map without edge constraints, often struggle to delineate sharp crustal boundaries. It has often been used to resolve lateral heterogeneities and sharp crustal boundaries (Blakely and Simpson, 1986; Hsu et al., 1996). The different edge enhancement methods used in this study are Horizontal Gradient, First Vertical Derivative and Analytical Signal.

Horizontal Gradient Method

This technique works on the principle of identifying local maxima in the gravity data (Cordell and Grauch, 1985). The local maxima do not mean the gravity high or low, rather it indicates the abrupt transition in gravity as we move along surface.

$$HG = \sqrt{\left(\frac{\partial g}{\partial x}\right)^2 + \left(\frac{\partial g}{\partial y}\right)^2}$$

The mathematical formula of horizontal gradient method suggests that the method is more concern about the spatial gradient than the absolute values. Which means this method focuses on increasing and decreasing value of gravity in both x and y direction, and mark the area as local maxima where the transition is strongest, which represents the possible edge or boundary of the associated feature (Chowdari et al., 2017, 2022). The aim of using the method for this study is to highlight structural edges such as fault, lineament and rift boundaries.

Figure 6 shows horizontal gradient map of residual gravity data over Bastar craton. The most significant features on the map are: NW-SE trending gradient maxima HZ1 near Raipur area, likely representing a buried fault zone in Chhattisgarh basin margin. The strong gravity gradient seen along HZ2, within the eastern part of the Bastar craton, trending towards N-S direction, marks a faulted boundary between Proterozoic sediment cover and adjoining granitic basement. E-W oriented lineament in SE part of craton (HZ3), could possibly be a tectonic contact between Bastar and EGB. Another gradient maxima HZ4 orienting towards NNE-SSW, corresponds to the contact between the Bastar craton and the Godavari rift basin. A notable fault marked by HZ6 is possibly a structural discontinuity between Deccan Province and the supracrustal basement rocks. Similarly, HZ7, a NW-SE trending maximum gradient, corresponds to a lineament near Mahanadi graben.

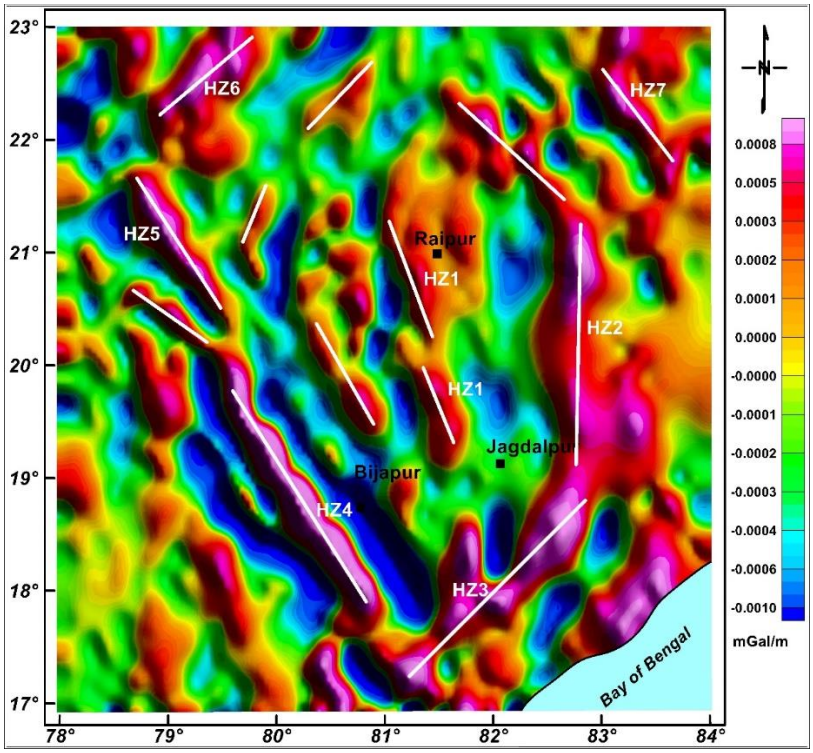

Figure 6. Horizontal gradient map of the residual gravity anomaly field with marked gravity interpreted faults (HZ1 to HZ7), as shown in white colour.

First Vertical Derivative Method

The horizontal gradient method outlines the structural edges by detecting lateral density contrast, however, it does not explain the extensional depth of the structure. First vertical derivative (Milligan and Gunn, 1997; Gönenç, 2014) fills that gap by pointing out rapid vertical changes in gravity.

$$\mathrm{FVD} = \frac{\partial \mathrm{g}(\mathrm{x},\mathrm{y},\mathrm{z})}{\partial \mathrm{z}}$$

This method acts as a high pass filter by calculating rate of change of gravity field in vertical direction, which reduces the contribution from deeper anomalies and enhance short wavelength features, associated with shallow crustal structures. Figure 7 shows First vertical derivative map, which reveals a more detailed picture of the subsurface, with multiple significant lineaments which were not prominent in the horizontal gradient map. The lineaments which were mentioned earlier are visible in vertical derivative map, with additional features trending towards NW-SE direction in NE part of Raipur, NNW-SSE oriented lineament in SE part and NNE-SSW oriented linear trend, all of which indicate a complicated subsurface geology.

Analytical signal Method

This method enhances gravity anomaly interpretation by combining both horizontal gradient and vertical derivative into a single measure (Klingele et al.,1991).

$$AS = \sqrt{\left(\frac{\partial g}{\partial x}\right)^2 + \left(\frac{\partial g}{\partial y}\right)^2 + \left(\frac{\partial g}{\partial z}\right)^2}$$

This fusion allows the method to capture the change in all directions, and produce a maximum directly above the boundary of subsurface density contrasts (Hakim et al., 2006). Unlike other edge enhancement techniques which are sensitive only in one aspect of anomaly, analytical signal balances both lateral and vertical information. This makes it particularly useful for outlining geological boundaries in complex crustal settings more precisely. Analytical signal map for the present study area (Figure 8), reveals some lineaments structures mainly in NE and central part of the craton, which were masked in previous maps. The boundaries of the entire Bastar craton are very well reflected here.

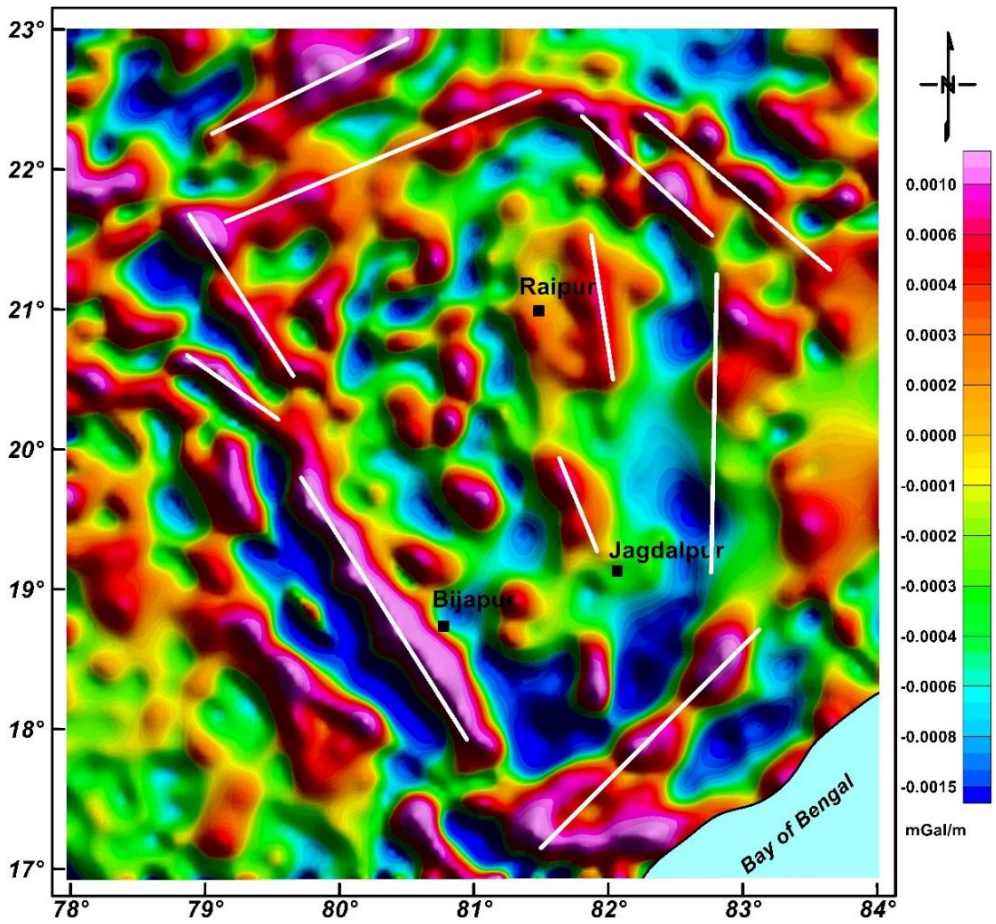

Figure 7. First-order vertical derivative map of residual gravity anomaly with marked gravity interpreted faults in white color.

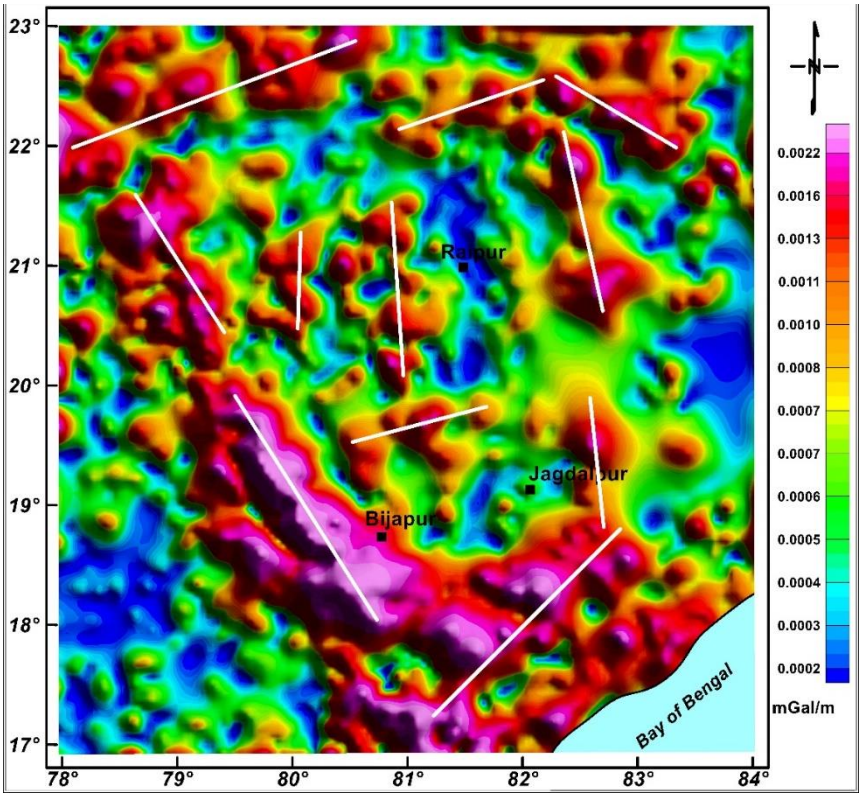

Figure 8. Analytical signal map of residual gravity anomaly with marked gravity Interpreted faults in white colour.

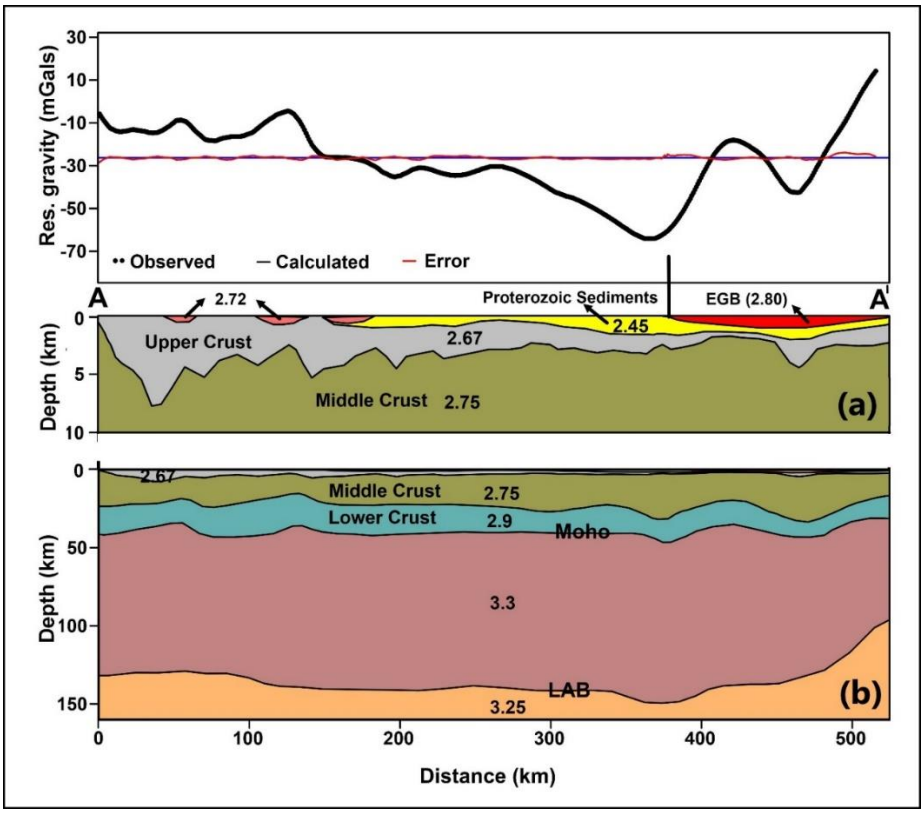

Figure 9. Density model along Profile AA' (location shown in Figure 5). **(a)** shallow crustal structure, and **(b)** lithospheric structure.

2.5D GRAVITY MODELLING

In order to understand the underlying crustal architecture, 2.5D modelling has been carried out along a NW-SE profile AA' cutting across the entire craton and adjacent EGB region (Figure 5). As the precise interpretation of gravity anomalies is non-unique, and often depends on direct inputs like the nature of the underlying rocks and their in-situ densities, we have used the available geophysical constraints in this region for different crustal layers in terms of their thicknesses and densities (Chalapathi Rao et al., 2011; Mandal et al., 2013).

The resultant best-fit density model (with an error of 0.7) along the profile AA' is shown in Figure 9. The top layer, corresponding to Proterozoic sediments, is assigned a density of 2.45 g/cm^3. This layer is followed by a thin upper crustal layer with density 2.67 g/cm^3, and mid-crustal layer, 2.75 g/cm^3. This layer is further underlain by a relatively high density lower-crustal layer which is assigned a density of 2.9 g/cm^3. Similarly, lithospheric mantle is assigned a density of 3.3 g/cm^3. Moho depth along this profile is taken as ~35 km below EGB to ~46 km beneath the sedimentary basins. Lithosphere-Asthenosphere Boundary (LAB) has been delineated between 100 to 144 km. This study delineated the sedimentary formation of the craton beneath the high-grade Eastern Ghats Belt (EGB) (Figure 9).

DISCUSSION AND CONCLUSIONS

The tectonic framework of the eastern Indian shield, particularly along the Bastar craton–Eastern Ghats Belt (EGB) interface, provides critical insights into Proterozoic crustal dynamics and the structural architecture of ancient continental margins. The satellite-derived gravity data analyzed in this study brings out clearly the continuation of Proterozoic sedimentary sequences of the Bastar craton beneath the high-grade EGB terrain. The identification of a prominent residual gravity low (around –50 mGal) in the south-eastern part of the study area, where EGB lithologies dominate the surface geology, is a compelling geophysical signature suggestive of the presence of low-density crustal materials, which appears representing buried Mesoproterozoic sediments such as those of the Indravati and Khariar Groups underneath the granulitic terrain. These gravity anomalies are consistent with the crustal configurations elsewhere in orogenic belts where older sedimentary sequences are tectonically buried beneath younger or higher-grade metamorphic complexes (Pandey et al., 2014; Vasanthi and Singh, 2019; Vasanthi and Santosh, 2023). The gravity modeling results strengthen this interpretation by revealing steep, east-dipping crustal-scale density boundaries, which are indicative of large-scale underthrusting (Figure 9). Such configurations are typical of continental collision zones, where rigid cratonic blocks are partially underthrusted beneath mobile belts, resulting in crustal thickening and complex metamorphic overprinting. This tectonic episode is closely linked with the evolution of Rodinia supercontinent assembly, which involved widespread craton amalgamation and crustal reworking across several continental margins (Pandey et al., 2018; Singh et al., 2025). The development of ductile shear zones such as the Terrane Boundary Shear Zone, facilitated this crustal stacking, enabling the high-grade EGB rocks to thrust over relatively low-grade or un-metamorphosed Proterozoic sequences derived from the Bastar craton. Importantly, this study contributes to a growing body of evidence that redefines the EGB not as an entirely exotic terrane but as a mobile belt with genetic and structural ties with the adjacent Indian cratons. This re-interpretation has broad implications for models of crustal accretion, basin evolution, and tectonothermal reworking in the Indian shield, and encourages a re-evaluation of similar craton–mobile belt interfaces globally.

Acknowledgements

We sincerely thank Dr. Prakash Kumar, Director, CSIR-National Geophysical Research Institute, Hyderabad, for the permission to publish this work. Ankita Roy expresses her sincere thanks to Dr. Abhey Ram Bansal, project Leader ,Gravity and Magnetic Group, CSIR- NGRI, for his constant encouragement and support during Internship at NGRI. We profoundly thank Dr. O. P. Pandey, Editor-in-Chief, for his valuable comments and suggestions to improve the quality of the manuscript. The work has been approved by CSIR-NGRI for publication as contribution number NGRI/LIB/2025/Pub-81.

Author Credit Statement

Ankita Roy: Original manuscript writing, data analysis and figure preparation. Ch. Swarnapriya: Data analysis and figure preparation. A. Vasanthi: Conceptualization, original manuscript writing, editing and reviewing.

Data Availability

The satellite gravity data is available in http:// icgem.gfz-potsdam.de/calcgrid (Zingerle et al., 2020).

Compliance with ethical standards

The authors does not have any competing interest and adhere to copyright norms.

REFERENCES

Asokan, A. D., Elangovan, R., Vishwakarma, N., Hari, K. R. and Ram Mohan, M., 2020. Petrogenesis of the Kanker granites from the Bastar Craton: implications for crustal growth and evolution during the Archean-Proterozoic transition. Front. Earth Sci., 8, 212.

Bandyopadhyay, B. K., 1995. Structure and tectonics of a part of Central Indian shield. Mem. Geol. Soc. India., 31, 433-467.

Bhadra, S., Gupta, S. and Banerjee, M., 2004. Structural evolution across the Eastern Ghats Mobile Belt–Bastar craton boundary, India: hot over cold thrusting in an ancient collision zone. J. Struct. Geol., 26(2), 233-245.

Biswal, T. K., Seward, D. and Jena, S. K., 2001. Eastern Ghats Mobile Belt is an epitome of mesoproterozoic fold thrust belt: a study from its NW margin. Gondwana Res., 4(4), 579-581.

Blakely, R. J. and Simpson, R. W., 1986. Approximating edges of source bodies from magnetic or gravity anomalies. Geophys., 51(7), 1494-1498.

Chakraborty, M. and Debnath, S., 2023. Mapping Facies Classification of Volcanic and Associated Succession in the Dongargarh Province. J. Geol. Soc. India, 99 (6), 886–887.

Chalapathi Rao, N.V., Lehmann, B., Mainkar, D. and Belyatsky, B., 2011. Petrogenesis of the end-Cretaceous Behradih kimberlite (orangeite): implication for mantle plume–lithosphere interaction in the Bastar craton, Central India. Contrib. Miner. Petrol., 161, 721-742.

Chowdari, S., 2019. Gravity studies of Gondwana Rift basins of India with special emphasis on Son-Mahanadi Basin. Ph.D. Thesis. Osmania University, Hyderabad.

Chowdari, S., Singh, B., Rao, B. N., Kumar, N., Singh, A. P. and Chandrasekhar, D. V., 2017. Structural mapping based on potential field and remote sensing data, South Rewa Gondwana Basin, India. J. Earth Syst. Sci., 126, 1-27.

Chowdari, S., Singh, B. and Singh, A. P., 2022. Anatomy of an intracratonic Son-Mahanadi Gondwana rift basin in Peninsular India: An integrated gravity, magnetic and remote sensing approach. Phys. Earth Planet. Inter., 328, 106888.

Cordell, L. and Grauch, V. J. S., 1985. Mapping basement magnetization zones from aeromagnetic data in the San Juan Basin, New Mexico. In The utility of regional gravity and magnetic anomaly maps. SPG., 181-197.

Deb, S. P., 2004. Lithostratigraphy of the Neoproterozoic Chattisgarh Sequence, its bearing on the tectonics and palaeogeography. Gondwana Res., 7(2), 323-337.

Gönenç, T., 2014. Investigation of distribution of embedded shallow structures using the first order vertical derivative of gravity data. J. Appl. Geophys., 104, 44-57.

Gupta, M. L., Sundar, A., Sharma, S. R. and Singh, S. B., 1993. Heat flow in the Bastar craton, central Indian shield: implications for thermal characteristics of Proterozoic cratons. Phys. Earth Planet. Inter., 78(1-2), 23-31.

Hakim, S., H., Nishijima, J., Ehara, S. and Aboud, E., 2006. Integrated gradient interpretation techniques for 2D and 3D gravity data interpretation. EPSL., 58, 815-821.

Hsu, S. K., Sibuet, J. C. and Shyu, C. T., 1996. High-resolution detection of geologic boundaries from potential-field anomalies: An enhanced analytic signal technique. Geophysics, 61(2), 373-386.

Jagadeesh, S. and Rai, S. S., 2008. Thickness, composition, and evolution of the Indian Precambrian crust inferred from broadband seismological measurements. Precambrian Res., 162(1-2), 4-15.

Klingele, E. E., Marson, I. and Kahle, H. G., 1991. Automatic interpretation of gravity gradiometric data in two dimensions: vertical gradient 1. Geophys. Prospect., 39(3), 407-434.

Kumar, N., Singh, A. P., Gupta, S. B. and Mishra, D. C., 2004. Gravity signature, crustal architecture and collision tectonics of the Eastern Ghats Mobile Belt. J. Indian Geophys. Union., 8, 97-106.

Mallick, K., Vasanthi, A. and Sharma, K. K., 2012. Bouguer gravity regional and residual separation: Application to geology and environment. Springer-Verlag.

Mandal, B., Sen, M. K. and Vijaya Rao, V., 2013. New seismic images of the Central Indian Suture Zone and their tectonic implications. Tectonics, 32(4), 908-921.

Meert, J. G., 2003. A synopsis of events related to the assembly of eastern Gondwana. Tectonophysics, 362(1-4), 1-40.

Milligan, P. R. and Gunn, P. J., 1997. Enhancement and presentation of airborne geophysical data. AGSO J. Aust. Geol. Geophys., 17(2), 63-75.

Mitra, S., Priestley, K., Gaur, V. K., Rai, S. S. and Haines, J., 2006. Variation of Rayleigh wave group velocity dispersion and seismic heterogeneity of the Indian crust and uppermost mantle. Geophys. J. Int., 164(1), 88-98.

Mohanty, S. P., 2021. The Bastar Craton of Central India: Tectonostratigraphic evolution and implications in global correlations. Earth-Sci. Rev., 221, 103770.

Naqvi, S. M. and Rogers, J. J. W., 1987. Pre. Geo. of India. Oxford University Press. New York, 223.

Pandey, O. P., Tripathi, P., Parthasarathy, G., Rajagopalan, V. and Sreedhar, B., 2014. Geochemical and mineralogical studies of chlorine-rich amphibole and biotite from the 2.5 Ga mid-crustal basement beneath the 1993 Killari earthquake region, Maharashtra: evidence for mantle metasomatism beneath the Deccan trap. J. Geol. Soc. India, 83(6), 599-612.

Pandey, O. P., Chandrakala, K., Vasanthi, A. and Kumar, K. S., 2018. Seismically imaged shallow and deep crustal structure and potential field anomalies across the Eastern Dharwar Craton, south Indian shield: Possible geodynamical implications. J. Asian Earth Sci., 157, 302-316.

Ramakrishnan, M. and Vaidyanadhan, R., 2010. Geology of India: GSI., Bangalore, 994p.

Rao, B. N., Singh, B. and Ravikumar, M., 2023. Lithospheric density structure beneath the dyke swarm region of the southern Bastar craton reveals a possible Proterozoic mantle plume: Inference from gravity and geoid study. J. Asian Earth Sci., 256, 105820.

Santosh, M., Tsunogae, T., Yang, C. X., Han, Y. S., Hari, K. R., Prasanth, M. M. and Uthup, S., 2020. The Bastar craton, central India: A window to Archean–Paleoproterozoic crustal evolution. Gondwana Res., 79, 157-184.

Sarkar, A., Sarkar, G., Paul, D. K. and Mitra, N. D., 1990. Precambrian geochronology of the central Indian shield: a review. Geol. Surv. India, Spec. Publ. (28), 453-482.

Sarkar, G., Corfu, F., Paul, D. K., McNaughton, N. J., Gupta, S. N. and Bishui, P. K., 1993. Early Archean crust in Bastar Craton, Central India—a geochemical and isotopic study. Precambrian Res., 62(1-2), 127-137.

Satpathi, K., Hifzurrahman, H., Xie, H. Q., Misra, S., Nasipuri, P. Ao, S., 2022. A2-type granites from the Bastar Craton, South-Central India, and their implication in Archean-Paleoproterozoic tectonics in Indian Peninsula. Lithosphere, Special 8, 7938481.

Sharma Ram, S., 2010. Cratons and fold belts of India. Lecture Notes in Earth Sciences,127, 61-61.

Singh, S., Chandrakala, K. and Pandey, O. P., 2025. 3-D Crustal Structure Modelling of the Proterozoic Cuddapah Basin, Its Regional Geodynamic Evolution and Columbia–Rodinia Connection. Geol. J., 1-24.

Smithies, R. H., Champion, D. C. and Van Kranendonk, M. J., 2009. Formation of Paleoarchean continental crust through infracrustal melting of enriched basalt. Earth Planet. Sci. Lett., 281(3-4), 298-306.

Srivastava, R. K., Söderlund, U., Ernst, R. E. and Gautam, G. C., 2021. A Ca. 2.25 Ga mafic dyke swarm discovered in the Bastar craton, Central India: Implications for a widespread plume-generated large Igneous Province (LIP) in the Indian shield. Precambrian Res., 360, 106232.

Subrahmanyam, C. and Verma, R. K., 1986. Gravity field, structure and tectonics of the Eastern Ghats. Tectonophysics., 126(2-4), 195-212.

Valdiya, K. S., 2015. Mesoproterozoic Eastern Ghat Mobile Belt. The Making of India: Geod. Evol., 185-204.

Vasanthi, A., 2025. Mulugu Earthquake: Reactivation of a deep-seated crustal fault in Godavari Graben (India). J. Indian Geophys. Union., 29,124-131.

Vasanthi, A. and Santosh, M., 2021a. Overview of regional gravity field computation models and application of a novel method in imaging the lithospheric architecture and destruction of the North China Craton. Earth-Sci. Rev., 215, 103548.

Vasanthi, A. and Santosh, M., 2021b. Lithospheric architecture and geodynamics of the Archean Dharwar craton and surrounding terranes: New insights from satellite gravity investigation. Gondwana. Res., 95, 14-28.

Vasanthi, A. and Santosh, M., 2023. Post-deformation effects of Indo-Eurasia convergence on major geological features of north-central India: New insights from satellite gravity observations. Phys. Earth Planet. Inter, 340, 107030.

Vasanthi, A. and Singh, A. P., 2019. Bouguer gravity field over Bundelkhand craton and its adjoining regions. J. Indian Geophys. Union., 23, 575-579.

Zingerle, P., Pail, R., Gruber, T. and Oikonomidou, X., 2020. The combined global gravity field model XGM2019e. J. Geod., 94(7), 66.

Received on: 10-07-2025 Revised on: 11-07-2025 ; Accepted on: 12-07\-2025

J. Ind. Geophys. Union, 29(4) (2025), 293-298
https://doi.org/10.71122/JIGU.29(4)2025.0028

Earth Day, April 22, 2025

Abhey Ram Bansal and ASSSRS Prasad
CSIR-National Geophysical Research Institute, Uppal Road, Hyderabad -500007 (India)

International Earth Day is celebrated every year on April 22 to create awareness about sustainability and environmental issues and to encourage individuals and communities to act together. The Earth Day celebration started in 1970 across the US through rallies and marches to educate the community about environmental issues. In 1990, it was celebrated in 141 countries. In 2016, the Paris Agreement was signed and adopted by 195 countries for the Earth Day celebration. The activities organised during Earth Day help mobilise public support, influence Policies and promote sustainability.

The Earth has been suffering from the overexploitation of natural resources (water, minerals, and hydrocarbons), deforestation, and pollution of water, air, and soil. Based on the climate model, 2150 GTon of groundwater was depleted between 1993 and 2010, resulting in a tilt in the Earth's axis of around 31.5 inches (Seo et al., 2023). From the satellite altimetry, the global mean sea level rise is reported as about 3.5 cm/year equivalent to groundwater depletion. The word glaciers which are the source of fresh water, are melting with an alarming rate due to anthropogenic activity and climate change and total ice mass is lost around 5 % since 2010 (The GlaMBIE Team, 2025). Even a slight temperature decrease will help to reduce the loss of ice mass. Deforestation also inhibits the ecosystem and the availability of fresh air. The excessive use of non-renewable energy leads to climate change, environmental pollution and unsustainable development. This year, Earth Day is celebrated with the theme of "Our Power, Our Planet" to increase awareness among society and educate them about their responsibility towards sustainable goals. The Indian Geophysical Union (IGU) celebrated Earth Day with Global Geoscience societies with a common statement, "Calls on all the people to work towards a future where energy is sustainable and accessible to everyone" (Figure **1**). The IGU celebrated Earth Day at 21 places across India, including universities, IIT'S, colleges, and schools, attended by faculty members, students, and community leaders (Figure 2). The following activities were organised during the Earth Day celebration.

- Tree plantation (Figure 3 and 4)
- Awareness rally (Figure 5)
- Oath ceremony (Figure 6)
- Human chain (Figure 7)
- Essay slogan writing (Figure 8)
- Drawing competition (Figure 9)

The Earth Day celebration was attended by 3288 members, of whom 1501 were female and 10 were differently abled and 294 plants were planted (Figure 10).

Figure 1. Joint statement on Earth Day with other global geoscience societies.

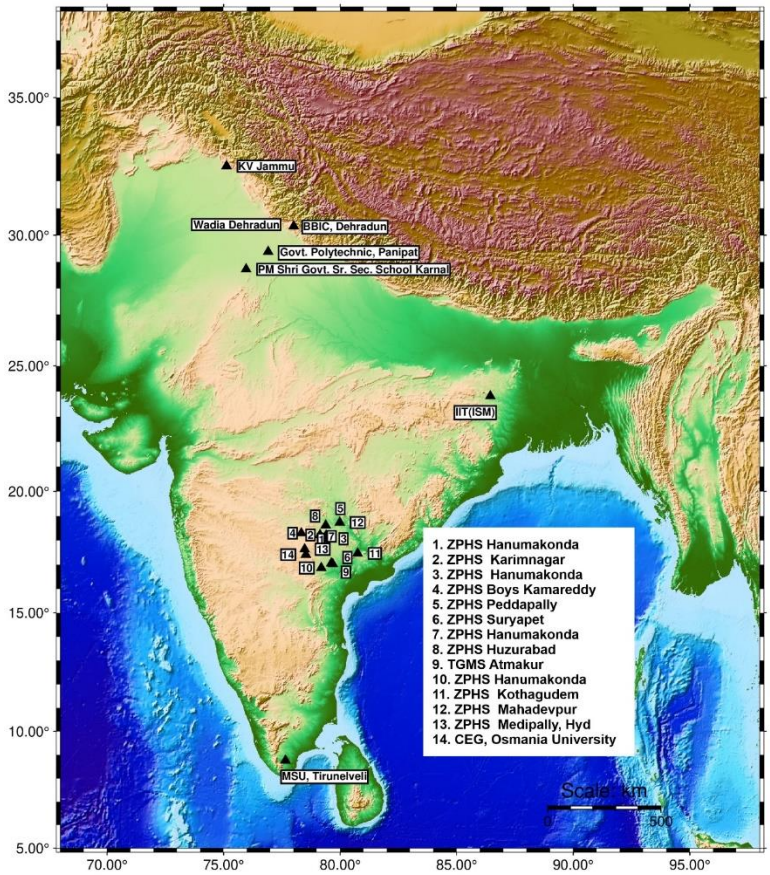

Figure 2. Map showing the locations of IGU's Earth Day celebration.

Figure 3. Tree plantation activity during IGU's Earth Day celebration.

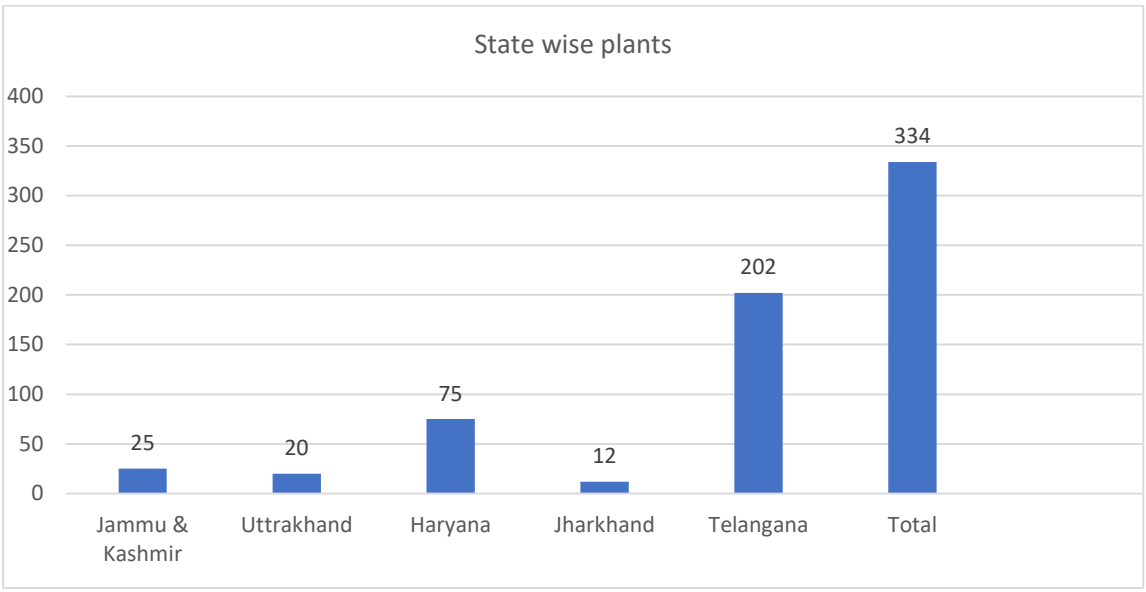

Figure 4. State-wise plantation done during the IGU's Earth Day celebration.

Figure 5. Awareness rally during IGU's Earth Day celebration.

Figure 6. Oath ceremony during IGU's Earth Day celebration.

Figure 7. Human chain during IGU's Earth Day celebration.

Figure 8. Essay competition and display of slogans during IGU's Earth Day celebration.

Figure 9. Drawing competition during IGU's Earth Day celebration.

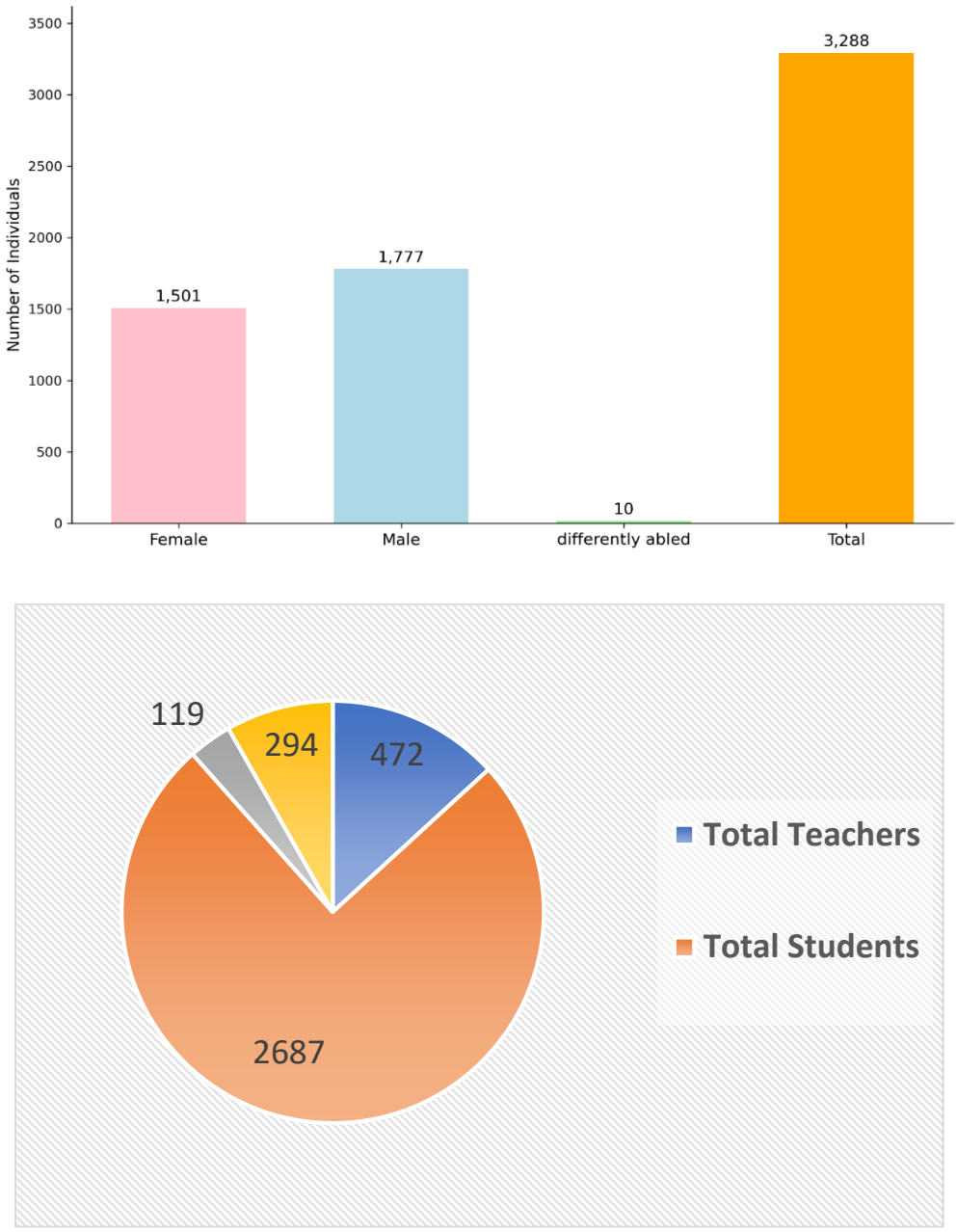

Figure 10. The Number of participants who attended the IGU's Earth Day celebration and the number of plants planted.

Acknowledgements

The Indian Geophysical Union is thankful to the Ministry of Earth Science, Government of India, for the financial support. We are also grateful to the management and Program coordinators of schools / colleges / Universities / IITS, for successfully organising the program. We are thankful to Ms G. Swaroopa and Mrs G. Swapna for helping us to prepare the report.

References:

Seo, K.-W., Ryu, D., Eom, J., Jeon, T., Kim, J.-S., Youm, K. et al., 2023. Drift of Earth's pole confirms groundwater depletion as a significant contributor to global sea level rise 1993–2010. Geophys. Res. Lett., 50, e2023GL103509. https://doi.org/10.1029/2023GL103509

The GlaMBIE Team. Community estimate of global glacier mass changes from 2000 to 2023. Nature, 639, 382–388 (2025). https://doi.org/10.1038/s41586-024-08545-z

Received on: 15-05-2025; Revised on: 23-05-2025 ; Accepted on: 23-05-2025

GUIDE FOR AUTHORS

The Journal of Indian Geophysical Union (JIGU), a SCI Journal published bimonthly by the Indian Geophysical Union (JIGU), is an inter disciplinary journal from India that publishes high-quality research in earth sciences with special emphasis on the topics pertaining to the Indian subcontinent and the surrounding Indian Ocean region. The journal covers several scientific disciplines related to the Earth sciences such as solid Earth Geophysics, geology and geochemistry, apart from marine, atmosphere space and planetary sciences. J-IGU welcomes contributions under the following categories :

*Research articles, short notes and students section reporting new findings, results, etc.

*Review articles providing comprehensive overview of a significant research field.

In addition, JIGU also welcomes short communications, after communications and report on scientific activity, book reviews, news and views, etc.

The manuscript should be submitted electronically as a single word format (.doc file) including the main text, figures, tables, and any other supplementary information along with the signed "Declaration Letter". The manuscript should be submitted by email (jigul1963@ gmail.com) to the Chief Editor.

After acceptance of the manuscript the corresponding author would be required to submit all source files (text and Tables in word format) and figure in high resolution standard (*.jpg, *.tiff, *.bmp) format. These files may be submitted to JIGU as a single *.zip file along with the "Copyright Transfer Statement".

IMPORTANT INFORMATION

Ethics in publishing; J-IGU is committed to ensuring ethics in publication and takes a serious view of plagiarism including self-plagiarism in manuscripts submitted to the journal, Authors are advised to ensure ethical values by submitting only their original work and due acknowledgement to the work of others used in the manuscript. Authors must also refrain from submitting the same manuscript to more than one journal concurrently, or publish the same piece of research work in more than one journal, which is unethical and unacceptable. Editor of JIGU is committed to make every reasonable effort to investigate any allegations of plagiarism brought to his attention, as well as instances that come up during the peer review process and has full authority to retract any plagiarized publication from the journal and take appropriate action against such authors if it is proven that such a misconduct was intentional.

Similarly, Editor and Reviewers are also expected to follow ethical norms of publishing by ensuring that they don't use any unpublished information, communicated to them for editorial or review purpose, in their own research without the explicit written consent of the author. They are also expected to keep manuscript' data/ observations/ any other information related to the peer review confidential to protect the interest of the authors. Reviewers should refrain from reviewing the manuscripts in which they have conflicts of interest resulting from competitive, collaborative, or other relationships or connections with any of the authors, companies, or institutions connected to the manuscript.

Conflict of interest

All authors are requested to disclose any actual or potential conflict of interest including any financial, personal or other relationships with other people or organizations within three years of beginning the submitted nor that could inappropriately influence, or be perceived to influence, their work.

Submission declaration

Submission of a manuscript implies that the work has not been published previously and it is not under consideration for publication elsewhere, and that if accepted it will not be published elsewhere in the same or any other form, in English or in any other language, without the written consent of the publishers. It also implies that the authors have taken necessary approval from the competent authority of the institute/organization where the work was carried out.

Copyright

After acceptance of the manuscript the corresponding author would be required to sign and submit the "Copyright Transfer Statement".

MANUSCRIPT PREPARATION

The corresponding author should be identified (include E-mail address, Phone/Mobile number). Full affiliation and postal address must be given for all co-authors.

Abstract:

An abstract of not more than 300 words must be included.

Text:

The manuscript should be structured to include a front page containing the title, Author(s) name, affiliation and address of the institute, where the work was carried out, and 5-to-6 Key words. Author(s) present address, if different from the above mentioned address, may be given in the footnote. The corresponding author should be identified with an asterisk and his/her email ID should be provided. This page should be followed by the main text consisting of Abstract, Introduction, Methods/ Techniques/ Area description, Results, Discussion, Conclusions, Acknowledgements, and References. Tables and Figures with captions should be inserted at the end of main text. It should not be inserted in the body of the text.

Figures/ Illustrations:

figures should be provided in camera-ready form, suitable for reproduction (which may include reduction) without retouching. Figures in high-resolution (at least 300 dpi) standard formats (*.jpg, * tiff, *.bmp) are acceptable. Figures should be numbered according to their sequence in the text. References should be made in the text to each figure. Each figure should have a suitable caption.

Tables:

Authors should take note of the limitations set by the size and layout of the journal. Table should not exceed the printed area of the page. They should be typed on separate sheets and details about the tables should be given in the text. Heading should be brief. Large tables should be avoided and may be provided as supplementary information, if required.

Equations:

Equations should be numbered sequentially with Arabic numerals and cited in the text. Subscripts and Superscripts should be set off clearly.

Equation writing software that presents each equation as an object in MS Word will be accepted. Style and convention adopted for the equations should be uniform throughout the paper.

References:

All references to publications cited in the main text should be presented as a list of references in order following the text and all references in the list must be cited in the text. References should be arranged chronologically, in the text. The list of references should be arranged alphabetically at the end of the paper.

References should be given in the following form:

Kaila, K.L., Reddy PR., Mall D.M., Venkateswarlu, N., Krishna V.G. and Prasad, A.S.S.S.R.S., 1992, Crustal structure of the west Bengal el eon deep seismic sounding investigations. Geophys. J. Int., 1,45-66.

REVIEW PROCESS:

All manuscripts submitted to the journal are peer-reviewed. It is advisable to send the contact details of 4 potential reviewers along with the manuscript to expedite the review process. Editor has the option to select reviewers from the list or choose different reviewers. The review process usually takes about 3 months. All enquiries regarding the manuscript may be addressed to the Chief Editor.

GALLEY PROOF:

Technical editing of manuscripts is performed by the editorial board. The author is asked to check the galley proof for typographical errors and to answer queries from the editor. Authors are requested to return the corrected proof within two days of its receipt to ensure uninterrupted proceedings The editor will not accept new material in proof unless permission from the editorial board has been obtained for the addition of a "note added in proof". Authors are liable to be charged for excessive alterations to galley proof.

PUBLICATION CHARGES:

There are no page charges for publication. The corresponding author will receive a soft copy (pdf format) of his/her published article. Should the author desire to purchase reprints of his/her publication, he/she must send the duly signed Reprint Order Form (accompanies the galley proof and contains price details) along with the corrected galley proof to the Editor. The reprint charges must be paid within one month of sending the Reprint Order Form.

Any payment related to printing or purchase of reprints should be made in the form of a Demand Draft in the name of Treasurer, Indian Geophysical Union, payable at Hyderabad.

You may download the pdf file from:
http://iguonline.in/journal/instructions.php